



**Università degli Studi di Milano**

---

FACULTY OF SCIENCE AND TECHNOLOGY  
Degree Course in Physics

MASTER THESIS

***AB INITIO* NUCLEAR STRUCTURE  
COMPUTATIONS WITH GENERALIZED  
SPHERICAL BASES**

Advisor:

**Prof. Carlo Barbieri**

Co-Advisor:

**Dott. Enrico Vigezzi**

Candidate:

**Alberto Scalesi**

**Matricola 939903**

---

Academic Year 2019-2020



INDEX
-------

<b>Introduction</b>	<b>5</b>
<b>1 Self-Consistent Green's Function method</b>	<b>7</b>
1.1 Introduction to <i>ab initio</i> methods . . . . .	7
1.2 The Green's functions formalism . . . . .	9
1.2.1 Spectral function . . . . .	12
1.2.2 The Galitskii-Migdal-Koltun sum rule . . . . .	13
1.2.3 ADC( <i>n</i> ) scheme . . . . .	15
1.2.4 The Optimized Reference State . . . . .	15
<b>2 Chiral Potentials</b>	<b>17</b>
2.1 Chiral EFT . . . . .	18
2.2 The hierarchy of nuclear forces . . . . .	20
2.3 Long-range and short-range terms . . . . .	21
2.4 Representation of two-nucleon states in EMN potentials . . . . .	22
<b>3 Nuclear potential matrix elements</b>	<b>23</b>
3.1 Nuclear potential matrix elements in <i>jj</i> coupling for the HO basis	23
3.2 Nuclear potential matrix elements in <i>jj</i> coupling for a general basis	29
3.3 The Wong-Clement coefficients . . . . .	32
3.3.1 Various expressions of $A_{II}(x)$ . . . . .	37
3.3.2 Three-body Wong-Clement coefficients . . . . .	43
<b>4 Generalized spherical bases for <i>ab initio</i> calculations</b>	<b>45</b>
4.1 Bases in nuclear physics . . . . .	45
4.2 Discrete Variable Representation . . . . .	46
4.2.1 Bessel DVR . . . . .	49

<i>CONTENTS</i>	4
4.2.2 Kinetic matrix elements for Bessel DVR functions . . . . .	57
4.2.3 The Bessel DVR model space . . . . .	58
<b>5 Results</b>	<b>65</b>
5.1 N <sup>4</sup> LO450 EMN potential . . . . .	66
5.1.1 Center-of-mass correction for HF radii . . . . .	71
5.1.2 Extrapolations toward low- and high-momentum scales . . . . .	75
5.2 Tests with different kinds of potentials . . . . .	85
5.2.1 N <sup>4</sup> LO550 EMN potential . . . . .	85
5.2.2 N <sup>3</sup> LO EMN potential . . . . .	93
<b>6 Summary and conclusions</b>	<b>97</b>
<b>Bibliography</b>	<b>99</b>

In nuclear physics, *ab initio* methods are fundamental computational tools that allow precise and controllable predictions of observables such as the ground state energy and the charge radii. These methods bring various advantages respect to other phenomenological approaches. First, they provide controllable and systematically improvable predictions. Second, they are directly linked with the fundamental theory of QCD. Finally, *ab initio* methods have the potential to give reliable predictions for nuclei that are not experimentally accessible. In the past decades, these methods have always relied on expanding the nuclear wave functions on HO bases. HO functions allow an exact separation of the center of mass from the intrinsic variables, providing simple analytical expression for the calculation of the interaction matrix elements, which are the fundamental input to numerical computations. However, they also pose several limitations in the study of complex nuclei, such as the weakly-bound ones, as they often cannot resolve the ultraviolet (UV) and infrared (IR) limits that are needed for proper convergence. Alternative bases have been proposed in the last years to overcome similar limitations. Discrete Variable Representation (DVR) bases are promising candidates [1, 2], yet codes for doing nuclear structure computations on a general basis are not available and the corresponding formalism needs to be properly adapted.

The main goal of the present work is to build all the necessary tools to allow the evaluation of two-body interaction matrix elements on a general basis, which are not yet available for modern applications with chiral forces. We will present a first attempt to use these matrix elements in self-consistent Green's function calculations to determine some basic properties of atomic nuclei. The comparison with standard HO calculations will allow us to investigate the main features and possible advances of a specific DVR basis (the spherical Bessel one)

in nuclear applications. In this first approach, we start scratching the surface of these new kind of applications limiting ourselves to the case of two-body forces. This is already sufficient to probe the different behaviors of the chosen bases and determine their main drawbacks and advantages.

In Chapter 1 we present the specific *ab initio* method that we are going to use for our computations. Chapter 2 introduces chiral potentials, which are the state of the art for nuclear structure calculations. Chapter 3 concentrates on developing all the machinery necessary for computing interaction matrix elements on a general basis, next in Chapter 4 we introduce a particular class of functions (the DVR ones), with particular attention to the one that we are going to use for our computations. Finally, in Chapter 5 we make a first attempt to apply these functions in nuclear structure computations and we discuss the main differences with the harmonic oscillator case. Future perspectives on the use of generalized spherical bases in nuclear structure are then given.

# CHAPTER 1

---

## SELF-CONSISTENT GREEN'S FUNCTION METHOD

### 1.1 Introduction to *ab initio* methods

The main goal of any *ab initio* method is to solve the nuclear many-body problem, which consists in finding a numerical solution to the non-relativistic Schrödinger equation

$$H |\psi_n\rangle = E_n |\psi_n\rangle \quad (1.1.1)$$

using effective two-body and three-body interactions which are constrained by the underlying theory of Quantum Chromodynamics. Virtually exact solutions of (1.1.1) are achievable for very light isotopes, while computations become progressively difficult for larger masses. For this reason it is important to have:

- systematically improvable methods;
- quantifications of errors.

*Ab initio* methods are based on various assumptions. First of all, the nucleons and pions are considered to be the most fundamental degrees of freedom. Processes explicitly involving quarks and gluons are seen to be important only at high energy, while in a low-energy picture only hadronic degrees of freedom are available to the system. Though there are various attempts of treating the nucleus as a multi quark-gluon system (e. g. the HAL QCD [3]), in *ab initio* the complexity of the structure of nucleons is taken in account only through the chosen realistic interaction. A second important point is that we are considering a non-relativistic framework (we are dealing with energies which are

small compared to the rest energy of the nucleon), with relativistic corrections already included in the interaction part of the Hamiltonian.

The many-body Hamiltonian used in *ab initio* incorporates a model for the nuclear forces and for the two- and three-body interactions. The theoretical framework mostly used in state-of-the-art *ab initio* calculations is the Chiral Effective Field Theory. The Hamiltonian is expressed separating the center-of-mass kinetic energy and the intrinsic Hamiltonian

$$H = T + V_{NN} + V_{3N} + \dots = T_{cm} + T_{int} + V_{NN} + V_{3N} + \dots = T_{cm} + H_{int} \quad (1.1.2)$$

with the proton-proton interaction and additional charge symmetry breaking effects of nuclear nature included in the  $V_{NN}$  terms. The intrinsic kinetic energy includes informations about the relative motion of nucleons respect to the center-of-mass, while the interaction term describes the relative internal degrees of freedom.

We are focusing on the intrinsic part of the Hamiltonian. The center of mass contribution constitutes a problem because its wave function is mixed with the intrinsic one. Fortunately, this spurious contribution can be estimated and approximately subtracted from the Hamiltonian.

It's clear that the difficult task is to solve the eigenvalue problem for the intrinsic Hamiltonian. We're dealing with theories expressed in Fock space that can break (even slightly) the number of particles.

Regarding the kinetic term  $T_{int}$ , considering that we're dealing with theories that don't conserve the total number of particles, we can express it as a sum of one- and two-body operators [4]

$$T_{int}^{(a)} = \left(1 - \frac{1}{\hat{A}}\right) \sum_i \frac{\mathbf{p}_i^2}{2m} - \frac{1}{\hat{A}m} \sum_{i<j} \mathbf{p}_i \cdot \mathbf{p}_j, \quad (1.1.3)$$

or using just two-body operators, considering the relative kinetic energies of nucleons

$$T_{int}^{(b)} = \frac{2}{\hat{A}} \sum_{i<j} \frac{\mathbf{q}_{ij}^2}{2\mu} = \frac{1}{2\hat{A}} \sum_{i<j} \frac{(\mathbf{p}_i - \mathbf{p}_j)^2}{m}. \quad (1.1.4)$$

In practical applications, one is forced to approximate this expression with the replacement  $\hat{A} \rightarrow A$ , we are then considering a theory with fixed number of particle in which the creation operator is substituted with the actual number of particle. This approximation is a tricky choice which can lead to discrepancies, for the numerical oscillations that can follow for little values of  $A$ .

Various *ab initio* methods have been developed over the past decades in order to deal with the many-body problem. The most successful ones include

- Green's function Monte Carlo (GFMC) [5];
- No-core shell model (NCSM) [6];
- Coupled cluster (CC) [7];
- Self-consistent Green's function (SCGF) [8];
- In-medium similarity renormalization group (IM-SRG) [10, 9].

In this thesis we will base our investigations on the Self-Consistent Green's function method.

## 1.2 The Green's functions formalism

Following [11] (chapter 2), [13, 12], we give a quick overview of the Green's function method that we're using for the computations realized in this work.

The propagation of a single particle/hole in a many-body system in its ground state ( $|\Psi_0^A\rangle$ ) is given by the single-particle propagator, also referred to as one-body Green's function

$$i\hbar g_{ss'}(\mathbf{r}, t; \mathbf{r}', t) = \langle \Psi_0^A | \hat{T}[\psi_s(\mathbf{r}, t)\psi_{s'}^\dagger(\mathbf{r}', t)] | \Psi_0^A \rangle, \quad (1.2.1)$$

where  $\hat{T}$  is the time-ordering operator and  $\psi_s^\dagger(\mathbf{r}, t)$ ,  $\psi_s(\mathbf{r}, t)$  are creation and annihilation field operators in the Heisenberg picture. In the simple case of a two-particle system, the time-ordering is defined as

$$\hat{T}[A(x, t_x), B(y, t_y)] = \begin{cases} A(x, t_x)B(y, t_y) & t_x > t_y \\ \pm B(y, t_y)A(x, t_x) & t_x < t_y \end{cases} \quad (1.2.2)$$

where the  $-/+$  sign stands for fermions/bosons. In the case of  $t > t'$ , eq. (1.2.1) describes the propagation of a particle created in the state  $|\Psi_0^A\rangle$  in  $\beta$  at time  $t$  to the point  $\alpha$  at time  $t'$ . For  $t < t'$ , the particle is removed in the space-time point  $(\alpha, t)$  and created in  $(\beta, t')$ , where  $\alpha$  and  $\beta$  are spatial coordinates. Expanding eq. (1.2.1) with the Heisenberg representation of the fields operators

$$\psi_s(\mathbf{r}, t) = e^{\frac{i}{\hbar}\hat{H}t}\psi_s(\mathbf{r})e^{-\frac{i}{\hbar}\hat{H}t}, \quad (1.2.3)$$

it is seen that the one-particle operator depends only on the time difference  $t-t'$  due to time translation invariance. Finally, introducing the  $c$ -number  $e^{-\frac{i}{\hbar}E_0^A t}$

we can write

$$g_{ss'}(\mathbf{r}, \mathbf{r}'; t - t') = -\frac{i}{\hbar} \vartheta(t - t') \langle \Psi_0^A | \psi_s(\mathbf{r}) e^{-\frac{i}{\hbar}(H - E_0^A)(t - t')} \psi_{s'}^\dagger(\mathbf{r}') | \Psi_0^A \rangle + \mp \frac{i}{\hbar} \vartheta(t' - t) \langle \Psi_0^A | \psi_s(\mathbf{r}) e^{\frac{i}{\hbar}(H - E_0^A)(t - t')} \psi_{s'}^\dagger(\mathbf{r}') | \Psi_0^A \rangle. \quad (1.2.4)$$

The Heaviside step function derives from the time-ordering and can be expanded as

$$\vartheta(\pm\tau) = \mp \lim_{\eta \rightarrow +} \frac{1}{2\pi i} \int_{-\infty}^{+\infty} d\omega \frac{e^{-i\omega\tau}}{\omega \pm i\eta}. \quad (1.2.5)$$

Using this relation in the one-body propagator we find

$$\begin{aligned} g_{ss'}(\mathbf{r}, \mathbf{r}'; \tau) &= \frac{i}{\hbar} \frac{1}{2\pi i} \int_{-\infty}^{\infty} d\omega \langle \Psi_0^A | \psi_s(\mathbf{r}) \frac{e^{[-i\omega - \frac{i}{\hbar}(H - E_0^A)]\tau}}{\omega + i\eta} \psi_{s'}^\dagger(\mathbf{r}') | \Psi_0^A \rangle \\ &\mp \frac{i}{\hbar} \frac{1}{2\pi i} \int_{-\infty}^{\infty} d\omega \langle \Psi_0^A | \psi_s(\mathbf{r}) \frac{e^{[-i\omega - \frac{i}{\hbar}(H - E_0^A)]\tau}}{\omega - i\eta} \psi_{s'}^\dagger(\mathbf{r}') | \Psi_0^A \rangle = \\ &= \frac{1}{2\pi} \int_{-\infty}^{\infty} d\omega e^{-i\omega\tau} \langle \Psi_0^A | \psi_s(\mathbf{r}) \frac{1}{\hbar\omega - (H - E_0^A) + i\eta} \psi_{s'}^\dagger(\mathbf{r}') | \Psi_0^A \rangle + \\ &\mp \langle \Psi_0^A | \psi_s(\mathbf{r}) \frac{1}{\hbar\omega + (H - E_0^A) - i\eta} \psi_{s'}^\dagger(\mathbf{r}') | \Psi_0^A \rangle. \end{aligned} \quad (1.2.6)$$

From this equation we can obtain the frequency-space representation of the propagator in the case of fermions

$$g_{ss'}(\mathbf{r}, \mathbf{r}'; \omega) = \int_{-\infty}^{\infty} d\tau e^{i\omega\tau} g_{ss'}(\mathbf{r}, \mathbf{r}'; \tau) \quad (1.2.7)$$

$$= \langle \Psi_0^A | \psi_s(\mathbf{r}) \frac{1}{\hbar\omega - (H - E_0^A) + i\eta} \psi_{s'}^\dagger(\mathbf{r}') | \Psi_0^A \rangle + \quad (1.2.8)$$

$$\mp \langle \Psi_0^A | \psi_{s'}^\dagger(\mathbf{r}') \frac{1}{\hbar\omega - (H - E_0^A) + i\eta} \psi_s(\mathbf{r}) | \Psi_0^A \rangle \quad (1.2.9)$$

$$= g_{ss'}^p(\mathbf{r}, \mathbf{r}'; \omega) + g_{ss'}^h(\mathbf{r}, \mathbf{r}'; \omega). \quad (1.2.10)$$

The above definitions can be rewritten for a general orthonormal basis

$$g_{\alpha\beta} = -\frac{i}{\hbar} \langle \Psi_0^A | \hat{T}[c_\alpha(t) c_\beta^\dagger(t')] | \Psi_0^A \rangle \quad (1.2.11)$$

$$\begin{aligned} g_{\alpha\beta}(\omega) &= \\ &= \langle \Psi_0^A | c_\alpha \frac{1}{\hbar\omega - (H - E_0^A) + i\eta} c_\beta^\dagger | \Psi_0^A \rangle \mp \langle \Psi_0^A | c_\beta^\dagger \frac{1}{\hbar\omega + (H - E_0^A) - i\eta} c_\alpha | \Psi_0^A \rangle. \end{aligned} \quad (1.2.12)$$

In our applications,  $\alpha$  and  $\beta$  label a complete single-particle basis that defines

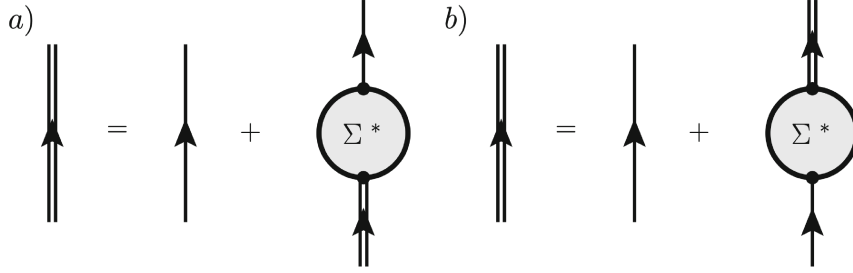


**Figure 1.1:** Diagrammatic representation of the two conjugate forms of the Dyson equation. Single lines represent the unperturbed propagator, double lines represent the dressed propagator. Image taken from [11].

the selected model space. Finally, inserting completeness relations for  $(A + 1)$ -bodies in (1.2.12) we obtain

$$\begin{aligned}
 g_{\alpha\beta}(\omega) &= \sum_n \frac{\langle \Psi_0^A | c_\alpha | \Psi_n^{A+1} \rangle \langle \Psi_n^{A+1} | c_\beta | \Psi_0^A \rangle}{\hbar\omega - (E_n^{A+1} - E_0^A) + i\eta} \\
 &\mp \sum_k \frac{\langle \Psi_0^A | c_\beta | \Psi_k^{A-1} \rangle \langle \Psi_k^{A-1} | c_\alpha | \Psi_0^A \rangle}{\hbar\omega - (E_k^{A-1} - E_0^A) - i\eta} = \\
 &\sum_n \frac{\mathcal{X}_\alpha^n \mathcal{X}_\beta^n}{\hbar\omega - \varepsilon_n^+ + i\eta} + \sum_k \frac{\mathcal{Y}_\alpha^k (\mathcal{Y}_\beta^k)^*}{\hbar\omega - \varepsilon_k^- - i\eta}, \quad (1.2.13)
 \end{aligned}$$

which is known as the ‘Lehmann’ or ‘spectral’ representation of the propagator. The two terms  $\varepsilon_n^+ = (E_n^{A+1} - E_0^A)$  and  $\varepsilon_k^- = (E_0^A - E_k^{A-1})$  label the poles of the Green’s function and represent respectively the one-nucleon addition and removal energies. The terms  $\mathcal{X}_\alpha^n = \langle \Psi_n^{A+1} | a_\alpha^\dagger | \Psi_0^A \rangle$  and  $\mathcal{Y}_\alpha^k = \langle \Psi_k^{A-1} | a_\alpha | \Psi_0^A \rangle$  represent the spectroscopic amplitudes associated for the addition and removal of a particle from the ground state. The propagator (1.2.13) can be calculated by solving the Dyson equation

$$g_{\alpha\beta}(\omega) = g_{\alpha\beta}^{(0)}(\omega) + \sum_{\gamma\delta} g_{\alpha\gamma}^{(0)}(\omega) \Sigma_{\gamma\delta}^*(\omega) g_{\beta\delta}(\omega) \quad (1.2.14)$$

$$= g_{\alpha\beta}^{(0)}(\omega) + \sum_{\gamma\delta} g_{\alpha\gamma}(\omega) \Sigma_{\gamma\delta}^*(\omega) g_{\beta\delta}^{(0)}(\omega), \quad (1.2.15)$$

which can be expressed in the different (conjugate) forms of eq. (1.2.14), (1.2.15).

The unperturbed propagator  $g_{\alpha\beta}^{(0)}(\omega)$  is the starting reference state and is usually chosen to be the Hartree-Fock state.  $g_{\alpha\beta}(\omega)$  is called *dressed* operator, since it is obtained by iteratively ‘dressing’ the free particle by interactions with the system.  $\Sigma_{\gamma\delta}^*(\omega)$  is the *irreducible self-energy* and is the non-local and

energy-dependent potential perceived by each fermion due to the interactions with the medium.

To solve the Dyson equation, we need a way to approximate the self-energy. In perturbation theory, the self-energy is expanded in a series of terms that depend on the interactions and on the propagator. The self-energy, written with its functional dependence  $\Sigma^*[g(\omega)]$ , can be determined through an iterative procedure in which  $\Sigma^*(\omega)$  and the Dyson equations are calculated until convergence. An efficient way to determine the self-energy is given by the Algebraic Diagrammatic Construction (ADC( $n$ )) approximation scheme, which is presented in Section 1.2.1.

### 1.2.1 Spectral function

The spectral function is a fundamental quantity that can be accessed directly by the experiments. To derive it, we reexpress the propagator using the Sokhotski-Plemelj equation

$$\frac{1}{x \pm i\eta} = \mathcal{P} \frac{1}{x} \mp i\pi\delta(x) \quad (1.2.16)$$

$$\begin{aligned} g_{\alpha\beta}(\omega) = & \sum_n \langle \Psi_0^A | c_\alpha | \Psi_n^{A+1} \rangle \langle \Psi_n^{A+1} | c_\beta^\dagger | \Psi_0^A \rangle \\ & \times \left[ \mathcal{P} \frac{1}{\hbar\omega - (E_n^{A+1} - E_0^A)} - i\pi\delta(\hbar\omega - (E_n^{A+1} - E_0^A)) \right] \\ & \mp \sum_k \langle \Psi_0^A | c_\beta^\dagger | \Psi_k^{A-1} \rangle \langle \Psi_k^{A-1} | c_\alpha | \Psi_0^A \rangle \\ & \times \left[ \mathcal{P} \frac{1}{\hbar\omega - (E_0^A - E_k^{A-1})} + i\pi\delta(\hbar\omega - (E_0^A - E_k^{A-1})) \right]. \end{aligned} \quad (1.2.17)$$

The *spectral function* is then separated in a particle and a hole terms:

$$S_{\alpha\beta}(\omega) = S_{\alpha\beta}^p(\omega) + S_{\alpha\beta}^h(\omega), \quad (1.2.18)$$

which are defined as:

$$\begin{aligned} S_{\alpha\beta}^p(\omega) = & -\frac{1}{\pi} \text{Im} g_{\alpha\beta}^p(\omega) = \sum_n \langle \Psi_0^A | c_\alpha | \Psi_n^{A+1} \rangle \langle \Psi_n^{A+1} | c_\beta^\dagger | \Psi_0^A \rangle \delta(\hbar\omega - (E_n^{A+1} - E_0^A)), \\ & \text{for } \omega > E_0^{A+1} - E_0^A \end{aligned} \quad (1.2.19)$$

$$\begin{aligned} S_{\alpha\beta}^h(\omega) = & \frac{1}{\pi} \text{Im} g_{\alpha\beta}^h(\omega) = \mp \sum_k \langle \Psi_0^A | c_\alpha | \Psi_k^{A-1} \rangle \langle \Psi_k^{A-1} | c_\beta^\dagger | \Psi_0^A \rangle \delta(\hbar\omega - (E_n^A - E_0^{A-1})), \\ & \text{for } \omega > E_0^A - E_0^{A-1} \end{aligned} \quad (1.2.20)$$

The one-body propagator can be written as a function of the spectral function using dispersion relations, as

$$g_{\alpha\beta}(\omega) = \int_{-\infty}^{\infty} d\omega' \frac{S_{\alpha\beta}^p(\omega')}{\hbar\omega - \hbar\omega' + i\eta} + \int_{-\infty}^{\infty} d\omega' \frac{S_{\alpha\beta}^h(\omega')}{\hbar\omega - \hbar\omega' - i\eta}. \quad (1.2.21)$$

Eq. (1.2.21) can be proved solving the integral part and comparing to Eq. (1.2.13).

$$\int_{-\infty}^{\infty} d\omega' \frac{S_{\alpha\beta}^p(\omega')}{\hbar\omega - \hbar\omega' + i\eta} + \int_{-\infty}^{\infty} d\omega' \frac{S_{\alpha\beta}^h(\omega')}{\hbar\omega - \hbar\omega' - i\eta} = \quad (1.2.22)$$

$$= \sum_n \langle \Psi_0^A | c_\alpha | \Psi_n^{A+1} \rangle \langle \Psi_n^{A+1} | c_\beta^\dagger | \Psi_0^A \rangle \int_{-\infty}^{\infty} d\omega' \frac{\delta(\hbar\omega' - (E_n^{A+1} - E_0^A))}{\hbar\omega - \hbar\omega' + i\eta} + \quad (1.2.23)$$

$$\mp \sum_k \langle \Psi_0^A | c_\beta^\dagger | \Psi_k^{A-1} \rangle \langle \Psi_k^{A-1} | c_\alpha | \Psi_0^A \rangle \int_{-\infty}^{\infty} d\omega' \frac{\delta(\hbar\omega' - (E_0^A - E_k^{A-1}))}{\hbar\omega - \hbar\omega' - i\eta} = \quad (1.2.24)$$

$$= \sum_n \langle \Psi_0^A | c_\alpha | \Psi_n^{A+1} \rangle \langle \Psi_n^{A+1} | c_\beta^\dagger | \Psi_0^A \rangle \frac{1}{\hbar\omega - (E_n^{A+1} - E_0^A) + i\eta} + \quad (1.2.25)$$

$$\mp \sum_k \langle \Psi_0^A | c_\beta^\dagger | \Psi_k^{A-1} \rangle \langle \Psi_k^{A-1} | c_\alpha | \Psi_0^A \rangle \frac{1}{\hbar\omega - (E_0^A - E_k^{A-1}) - i\eta} = \quad (1.2.26)$$

$$= g_{\alpha\beta}(\omega). \quad (1.2.27)$$

The diagonal part of the spectral function are  $S_{\alpha\alpha}(\omega) = S_{\alpha\alpha}^p(\omega) + S_{\alpha\alpha}^h(\omega)$

$$S_{\alpha\alpha}^p(\omega) = \sum_n |\langle \Psi_n^{A+1} | c_\alpha^\dagger | \Psi_0^A \rangle|^2 \delta(\hbar\omega - (E_n^{A+1} - E_0^A)) \quad (1.2.28)$$

$$S_{\alpha\alpha}^h(\omega) = \mp \sum_k |\langle \Psi_k^{A-1} | c_\alpha^\dagger | \Psi_0^A \rangle|^2 \delta(\hbar\omega - (E_0^A - E_k^{A-1})), \quad (1.2.29)$$

then  $S_{\alpha\alpha}(\omega)$  is interpreted as the probability of adding or removing a particle in the  $\alpha$  state while leaving the final system in an eigenstate with energy  $E_0^A \pm \hbar\omega$ .

## 1.2.2 The Galitskii-Migdal-Koltun sum rule

The GMK (Galitskii-Migdal-Koltun) sum rule is a useful relation which allows to calculate the ground state energy starting from the sole knowledge of the one-body propagator. This sum rule is exact for the case of one- and two-body interactions. The two-body Hamiltonian reads

$$H = \sum_{\alpha\beta} T_{\alpha\beta} c_\alpha^\dagger c_\beta + \frac{1}{2} \sum_{\alpha\beta\gamma\delta} V_{\alpha\beta,\gamma\delta} c_\alpha^\dagger c_\beta^\dagger c_\delta c_\gamma, \quad (1.2.30)$$

where the two contributions represent the kinetic energy matrix elements and the potential energy matrix elements. Writing the equations of motion associated with the operator  $\hat{c}_\alpha$  in the Heisenberg representation

$$i\hbar \frac{d}{dt} c_\alpha(t) = [c_\alpha(t), H] = e^{\frac{i}{\hbar} H(t-t')} [c_\alpha, H] e^{-\frac{i}{\hbar} H(t-t')}, \quad (1.2.31)$$

the commutator of this operator with the Hamiltonian can be shown to be

$$[c_\alpha, H] = \sum_{\beta} T_{\alpha\beta} c_\beta + \sum_{\beta\gamma\delta} V_{\alpha\beta,\gamma\delta} c_\beta^\dagger c_\delta c_\gamma. \quad (1.2.32)$$

Using this relation to compute the derivative of the propagator (1.2.13) gives

$$i\hbar \frac{\partial}{\partial t} g_{\alpha\beta}(t-t') = \sum_{\gamma} T_{\alpha\gamma} g_{\gamma\beta}(t-t') + \frac{i}{\hbar} \sum_{\gamma\delta\varepsilon} V_{\alpha\gamma,\delta\varepsilon} \langle \Psi_0^A | T [c_\gamma^\dagger(t) c_\varepsilon(t) c_\delta(t) c_\beta^\dagger(t')] | \Psi_0^A \rangle. \quad (1.2.33)$$

Now we need the relation between one-body propagator and one-body matrix density and the definition of two-body density matrix elements, respectively given by

$$\varrho_{\alpha\beta} = \pm i\hbar \lim_{t' \rightarrow t^+} g_{\alpha\beta}(t, t') \quad (1.2.34)$$

$$\Gamma_{\gamma\delta,\alpha\beta} = \langle \Psi^A | c_\alpha^\dagger c_\beta^\dagger c_\delta c_\gamma | \Psi^A \rangle, \quad (1.2.35)$$

which leads to

$$\pm i\hbar \left[ i\hbar \lim_{t' \rightarrow t^+} \sum_{\alpha} \frac{\partial}{\partial t} g_{\alpha\alpha}(t-t') \right] = \langle T \rangle + 2 \langle V \rangle. \quad (1.2.36)$$

The kinetic energy expectation value can be calculated as the expectation value of a general one-body operator

$$\langle T \rangle = \pm i\hbar \lim_{t' \rightarrow t^+} \sum_{\alpha\beta} T_{\beta\alpha} g_{\alpha\beta}(t, t') = \mp \sum_{\alpha\beta} \int_{-\infty}^{\infty} d\omega T_{\beta\alpha} S_{\alpha\beta}^h(\omega). \quad (1.2.37)$$

From Eqs (1.2.36) and (1.2.37) we finally obtain the Koltun sum rule for the ground-state energy:

$$\langle H \rangle = \langle T \rangle + \langle V \rangle = \pm \frac{1}{2} i\hbar \lim_{t' \rightarrow t^+} \left[ i\hbar \sum_{\alpha\beta} \left\{ \delta_{\alpha\beta} \frac{\partial}{\partial t} T_{\alpha\beta} \right\} \right] g_{\alpha\beta}(t-t'). \quad (1.2.38)$$

This method can be generalized with a correction for the three-body nuclear forces, as discussed in [14].

### 1.2.3 ADC( $n$ ) scheme

As we previously discussed, in order to solve the Dyson equation a numerical way to estimate the value of the irreducible self-energy is needed. A very efficient approach to do this is given by the ADC( $n$ ) *Algebraic Diagrammatic Construction at order  $n$*  approximation [15]. The ADC method is based on writing the self-energy  $\Sigma^*(\omega)$  in an analytical form, imposing the correct spectral representation of the propagator

$$\begin{aligned} \sum_{\alpha\beta}^* (\omega) = & -U_{\alpha\beta} + \Sigma_{\alpha\beta}(\infty) + \sum_{ij} M_{\alpha i}^\dagger \left[ \frac{1}{\omega - (\mathbf{E}^> + \mathbf{C}) + i\eta} \right]_{ij} M_{j\beta} + \\ & + \sum_{ij} N_{\alpha i} \left[ \frac{1}{\omega - (\mathbf{E}^< + \mathbf{D}) - i\eta} \right]_{ij} N_{j\beta}^\dagger, \end{aligned} \quad (1.2.39)$$

where  $U_{\alpha\beta}$  is the external field and  $\Sigma_{\alpha\beta}(\infty)$  is the correlated mean field.  $\mathbf{M}$  and  $\mathbf{N}$  are matrices which respectively couple single-particle states with 2p1h and 2h1p intermediate state configuration.  $\mathbf{E}^>$  and  $\mathbf{C}$  are the unperturbed energy and the 2p1h interaction, while  $\mathbf{E}^<$  and  $\mathbf{D}$  are the unperturbed energy and the 2h1p interaction.

$ADC(n)$  consists in including all the irreducible diagrams up to order  $n$  for the self-energy, plus all the other diagrams necessary to recover the correct analytical form of the self-energy of Eq. (1.2.39).

$ADC(1)$  simply reduces to the Hartree-Fock approximation. It includes only the first order diagram and it totally neglects nuclear correlations. The ground-state many-body wave-function is written as a Slater determinant of single-particle wavefunctions.

$ADC(2)$  is built summing irreducible energies up to the second order. This approximation can be used to study nuclear correlations. This is level of many-body truncation that we will exploit to investigate HO and DVR bases in **Chapter 5**

### 1.2.4 The Optimized Reference State

As we previously discussed, the propagator that is most often used as a starting reference in the solution of the Dyson equation is the Hartree-Fock one. However, for non-soft Hamiltonians the HF propagator can lead to a solution of the Dyson equation which is not reliable. This happens because the initial single-particle HF energies are too far from the correlated spectrum in the  $ADC(n \geq 2)$  self-energy, which leads to instabilities for the Dyson equation.

In this case, we can use the following procedure: first of all, the HF propagator is used to solve the Dyson equations until convergence. Then, the re-

sulting dressed propagator is used to generate a new HF-like propagator, which is simply another mean-field ansatz to be used as an *Optimized Reference State* (OpRS). The OpRS one-body propagator is obtained by mapping the fully correlated propagator to a simpler one that has a reduced number of poles, looking like a Slater-determinant reference (analogous to HF), but actually keeping the correct information on the unperturbed single-particle spectrum. The whole procedure is then iterated until convergence. Details are discussed in [16].

## CHAPTER 2

## CHIRAL POTENTIALS

The interaction part of the nuclear Hamiltonian constitutes its most complicated part. When two nucleons are close to each other, all the internal structure of the nucleons emerges and the quark-gluon distribution polarizes, giving an effective residual interaction. All these complications deriving from QCD must be taken into account in the nuclear interaction.

The QCD Lagrangian reads [17]

$$\mathcal{L}_{QCD} = \bar{q}(i\gamma^\mu \mathcal{D}_\mu - \mathcal{M})q - \frac{1}{4}\mathcal{G}_{\mu\nu,a}\mathcal{G}_a^{\mu\nu}, \quad (2.0.1)$$

with the gauge-covariant derivative

$$\mathcal{D}_\mu = \partial_\mu - ig\frac{\lambda_a}{2}\mathcal{A}_{\mu,a} \quad (2.0.2)$$

and the gluon field strength tensor

$$\mathcal{G}_{\mu\nu,a} = \partial_\mu\mathcal{A}_{\nu,a} - \partial_\nu\mathcal{A}_{\mu,a} + gf_{abc}\mathcal{A}_{\mu,b}\mathcal{A}_{\nu,c}, \quad (2.0.3)$$

where  $q$  is the quark fields and  $\mathcal{M}$  the quark mass matrix.  $g$  is the strong coupling constant and  $\mu, a$  are the gluon fields.  $\lambda_a$  represents the Gell-Mann matrices and  $f_{abc}$  the structure constants of the  $SU(3)$  Lie algebra. It is implicit the use of the Einstein convention, which involves a summation over repeated indices.

For a long time, the link between QCD and nuclear interactions has been a difficult task to solve. About 10/20 years ago, the state of the art for ab initio theories was the phenomenological NN interaction, mainly represented by two potentials: Argonne V18 (which includes a parametrization of short-medium

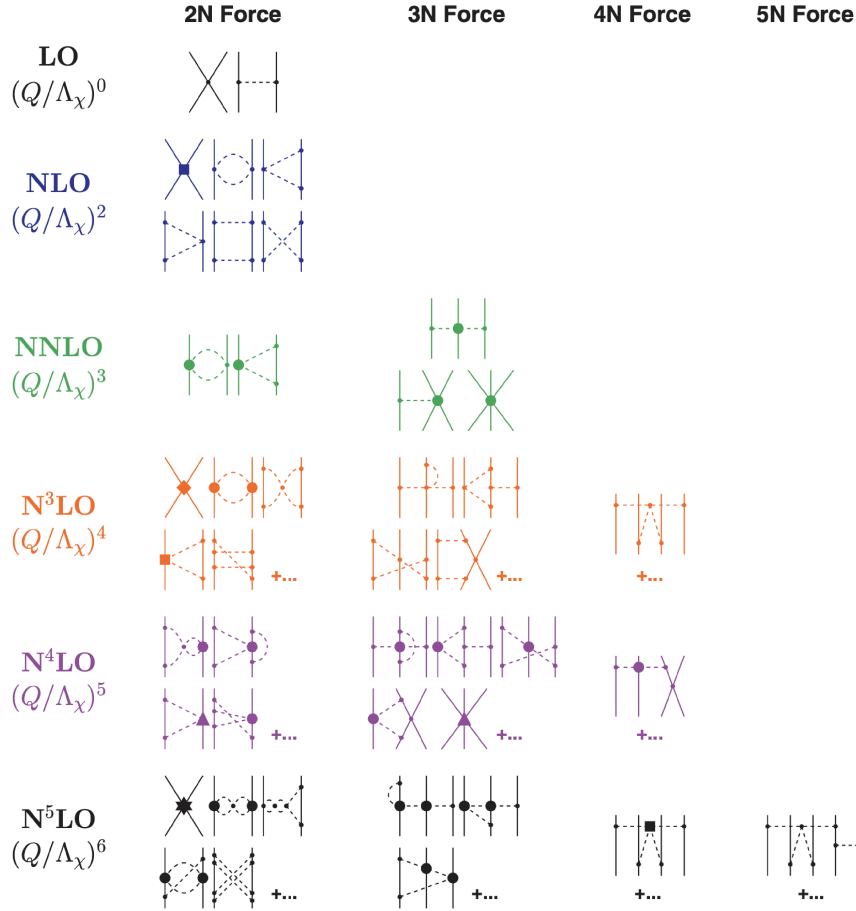


**Figure 2.1:** Hierarchy of nuclear forces in the Chiral Perturbative Theory. Solid lines represent nucleons, while dashed lines represent pions. The dots represents various kind of vertexes

range terms plus a long-range one-pion exchange term) and CD Bonn 2000 (which is mainly grounded on the meson exchange).

## 2.1 Chiral EFT

Today, the state of the art for ab initio calculations is the chiral Effective Field Theory (EFT). For the potentials based on this theory, the effective degrees of freedom are chosen according to the energy domain in which we want to perform calculations. These will be the nucleons and the pions, treated according to the symmetries of QCD. The long-range term is dominated by the exchange of pions, while the other contributions are included in contact terms, with low-energy parameters fit to experimental data. The number of parameters increases

with the order of the diagrams describing the interaction. In the two-body approximation these are mainly given by phase shifts, from electric scattering simulations.

The various contributions of the perturbative expansion of chiral EFT can be organized in a hierarchy: LO, NLO, N<sup>2</sup>LO, N<sup>3</sup>LO, ... in which each ‘N’ stands for ‘next to’ and ‘LO’ stands for ‘leading order’. As can be seen in the diagrammatic **Figure 2.1**, increasing the order of the interaction more multi-particle effects are included.

The chiral NN interactions that we’re using in this work have been developed by Entem, Machleidt and Noysk and are available in all the orders from LO to N<sup>4</sup>LO, for cutoffs of 450, 500 and 550 MeV. They accurately reproduce two-body scattering data up to  $\approx 300$  MeV. These potential include all the two-body physics we need.

Following [18], we give a more detailed description of the chiral EFT potentials N<sup>4</sup>LO that we are going to use and a description of the other orders potentials. At first, chiral perturbation theory was used mostly to describe  $\pi\pi$  and  $\pi N$  dynamics, which are the most suitable for a perturbative expansion. N<sup>4</sup>LO NN potentials have been widely used with chiral three-nucleon forces to study light and medium-mass nuclei and infinite matter. This order brings a lot of novelties, as new contributions from the 3NF contact interactions.

Here we’re focusing on the  $\Delta$ -less version of chiral EFT, in which delta baryons doesn’t appear (the main problem of this approach is that the strength of the  $P$ -wave two-pion-exchange three-nucleon interaction is overestimated by theories that do not include delta resonances as an explicit degree of freedom. This is discussed in detail in [19]. Then we’re dealing only with pions (which can be seen as Goldstone bosons) and nucleons as effective degrees of freedom. The interactions of Goldstone bosons must vanish at zero momentum transfer and in the chiral limit  $m_\pi \rightarrow 0$ , so the effective Lagrangian can be expanded in powers of derivatives and pion masses. The effective Lagrangian can be written as

$$\mathcal{L}_{eff} = \mathcal{L}_{\pi\pi} + \mathcal{L}_{\pi N} + \mathcal{L}_{NN} + \dots, \quad (2.1.1)$$

where the terms deals respectively with the two-pions dynamic, the pion-nucleon interaction and the two-nucleons contact interaction. Each of this terms is given by an increasing-order expansion

$$\mathcal{L}_{\pi\pi} = \mathcal{L}_{\pi\pi}^{(2)} + \mathcal{L}_{\pi\pi}^{(4)} + \dots \quad (2.1.2)$$

$$\mathcal{L}_{\pi N} = \mathcal{L}_{\pi N}^{(1)} + \mathcal{L}_{\pi N}^{(2)} + \mathcal{L}_{\pi N}^{(3)} + \mathcal{L}_{\pi N}^{(4)} + \dots \quad (2.1.3)$$

$$\mathcal{L}_{NN} = \mathcal{L}_{NN}^{(0)} + \mathcal{L}_{NN}^{(2)} + \mathcal{L}_{NN}^{(4)} + \dots \quad (2.1.4)$$

where the superscripts represents the number of pion mass insertions. These Lagrangians originate an infinite number of graphs, whose the irreducible ones define the nuclear potentials. These graphs are classified in terms of the quantity

$$(Q/\Lambda_\chi)^\nu, \tag{2.1.5}$$

where  $Q$  is the generic nucleon three-momentum, pion four-momentum or a pion mass.  $\Lambda_\chi \simeq 1 \text{ GeV}$  is the chiral symmetry-breaking scale. The index  $\nu$  labels the order of the ‘power counting’. A naive treatment of this counting, called also Weinberg counting, is the following: every nucleon propagator gives a term  $Q^{-1}$ , a pion propagator  $Q^{-2}$ , the derivative of an interaction  $Q$  and each four-momentum integration gives a  $Q^4$ .

## 2.2 The hierarchy of nuclear forces

Following **Figure 2.1**, we give a quick description of the first orders of the chiral expansion.

- The lowest order  $\nu = 0$  is the leading order (LO). Here the two-nucleon amplitude consists of two momentum-independent contact terms  $\simeq Q^0$ , which are represented by a four-nucleon-leg graph, and a one-pion exchange diagram. This second diagram includes the tensor force necessary for the description of the deuteron.
- The next order  $\nu = 1$  is always vanishing because of the parity and time-reversal invariance. So the next-to-leading order (NLO) is given by  $\nu = 2$ . This order describes more accurately the intermediate range interaction with the two-pion exchange diagram. The contact terms include a spin-orbit term and central, spin-spin and tensor terms. All the structures necessary to describe the nucleon-nucleon force phenomenologically are included in this order. The main problem of cutting the chiral perturbative expansion at this order is the lack of an efficient intermediate-range attraction.
- The following term ( $\nu = 3$ ) does not include new contact terms with respect to the previous one, but the problem of the two-pion exchange (2PE) is fixed because new vertices which represents a correlated two-pion exchange term and a  $\Delta$ -isobar contribution are included.
- Other 2PE diagrams are produced at order  $\nu = 4$ . 3PE has proven to be negligible at this order. 15 new contact terms ( $\simeq Q^4$ ) arise.

## 2.3 Long-range and short-range terms

The long-range contribution of the  $NN$  interaction is governed by pion exchanges, and their contributions can be summarized as

$$V = V_{1\pi} + V_{2\pi} + V_{2\pi} + \dots \quad (2.3.1)$$

$1\pi$  stands for one-pion exchange,  $2\pi$  for the two-pion exchange etc. For each term, the low-momentum expansion is given by

$$V_{1\pi} = V_{1\pi}^{(0)} + V_{1\pi}^{(2)} + V_{1\pi}^{(3)} + V_{1\pi}^{(4)} + \dots \quad (2.3.2)$$

$$V_{2\pi} = V_{2\pi}^{(2)} + V_{2\pi}^{(3)} + V_{2\pi}^{(4)} + \dots \quad (2.3.3)$$

$$V_{3\pi} = V_{2\pi}^{(4)} + V_{2\pi}^{(5)} + \dots \quad (2.3.4)$$

The subscript represents the order  $\nu$ . The various order of the Lagrangian are built up in the following way

$$V_{\text{LO}} = V^{(0)} = V_{1\pi}^{(0)} \quad (2.3.5)$$

$$V_{\text{NLO}} = V^{(2)} = V_{\text{LO}} + V_{1\pi}^{(2)} + V_{2\pi}^{(2)} \quad (2.3.6)$$

$$V_{\text{NNLO}} = V^{(3)} = V_{\text{NLO}} + V_{1\pi}^{(3)} + V_{2\pi}^{(3)} \quad (2.3.7)$$

$$V_{\text{N}^3\text{LO}} = V^{(4)} = V_{\text{NNLO}} + V_{1\pi}^{(4)} + V_{2\pi}^{(4)} + V_{3\pi}^{(4)} \quad (2.3.8)$$

$$V_{\text{N}^4\text{LO}} = V^{(5)} = V_{\text{N}^3\text{LO}} + V_{1\pi}^{(5)} + V_{2\pi}^{(5)} + V_{3\pi}^{(5)}. \quad (2.3.9)$$

The short-range potential is calculated as a sum of contact terms, with the constraint of parity and time reversal. These symmetries imply that odd powers of momentum vanish. Then the expansion of the contact potential is given by

$$V_{ct} = V_{ct}^{(0)} + V_{ct}^{(2)} + V_{ct}^{(4)} + \dots \quad (2.3.10)$$

Finally, the full potential is a sum of long-range and short-range potentials

$$V_{\text{LO}} = V^{(0)} = V_{1\pi} + V_{ct}^{(0)} \quad (2.3.11)$$

$$V_{\text{NLO}} = V^{(2)} = V_{\text{LO}} + V_{2\pi}^{(2)} + V_{2ct}^{(2)} \quad (2.3.12)$$

$$V_{\text{NNLO}} = V^{(3)} = V_{\text{NLO}} + V_{2\pi}^{(3)} \quad (2.3.13)$$

$$V_{\text{N}^3\text{LO}} = V^{(4)} = V_{\text{NNLO}} + V_{2\pi}^{(4)} + V_{3\pi}^{(4)} + V_{3ct}^{(4)} \quad (2.3.14)$$

$$V_{\text{N}^4\text{LO}} = V^{(5)} = V_{\text{N}^3\text{LO}} + V_{2\pi}^{(5)} + V_{3\pi}^{(5)}, \quad (2.3.15)$$

where higher order corrections to the 1PE are left aside because they are absorbed in the mass and coupling constant renormalizations.

## 2.4 Representation of two-nucleon states in EMN potentials

Entem-Machleidt-Noysk (EMN) potentials are calculated in the  $|q(lS)jM_T\rangle$  basis, which is a representation of the two-nucleon state in term of the spin  $S$ , the total angular momentum  $j$ , the orbital angular momentum  $l$ , the momentum  $q$  and the projection of the total isospin  $M_T$

$$\langle q(lS)jM_T|\hat{V}|q'(l'S)jM_T\rangle = V_{ll'}^{jSM_T}(q', q). \quad (2.4.1)$$

Fixed  $j, q, q'$  and  $M_T$ , only 6 possible configurations of  $l, l'$  and  $S$  are possible. This is due to the fact that the total number of configurations are restricted by the triangular inequality on  $(j, l, S)$  and the parity condition for the orbital angular momentum  $(-)^{l+l'} = 1$ . Among all the possible configurations of  $l = j - S, \dots, j + S, l' = j - S, \dots, j + S$ , the non-vanishing ones are given by the spin singlet, the uncoupled spin triplet and the 4 coupled triplet states:

$$l = l' = 0, \quad S = 0 \quad (2.4.2)$$

$$l = l' = 0, \quad S = 1 \quad (2.4.3)$$

$$l = l' = j - 1, \quad S = 1 \quad (2.4.4)$$

$$l = l' = j + 1, \quad S = 1 \quad (2.4.5)$$

$$l = j - 1, \quad l' = j + 1, \quad S = 1 \quad (2.4.6)$$

$$l = j + 1, \quad l' = j - 1, \quad S = 1 \quad (2.4.7)$$

The two-nucleon system carries a well-defined isospin  $T$  (which is 0 or 1) which is fixed by the Pauli condition

$$(-)^{l+S+T} = -1. \quad (2.4.8)$$

This identity is proven for the harmonic oscillator basis and for a general basis in [Section 3](#).

## CHAPTER 3

# NUCLEAR POTENTIAL MATRIX ELEMENTS

The main goal of this chapter is to obtain an equation to evaluate nuclear potential matrix elements on a general basis. First we will see how to obtain these matrix elements in the harmonic oscillator basis. These elements are simple to be determined because they can be written as a function of the well-known Moshinsky brackets, which decouple the relative and center-of-mass motions. Then we'll see how to generalize the equations for a general basis. To do this, we'll mainly follow [20], [21] and [22] in order to find different ways to write the Wong-Clement coefficients, which are the generalization of the Moshinsky brackets for a general basis.

### 3.1 Nuclear potential matrix elements in $jj$ coupling for the HO basis

We start from the single-particle state, coupling the total angular momentum and isospin of each particle  $(j_i, t_i)$  to the global variables  $(J, T)$ .

$$\begin{aligned} & |n_\alpha l_\alpha j_\alpha m_{j_\alpha} \tau_\alpha, n_\beta l_\beta j_\beta m_{j_\beta} \tau_\beta\rangle = \\ & = \sum_{JM_J} \sum_{TM_T} \langle j_\alpha j_\beta m_{j_\alpha} m_{j_\beta} | JM_J \rangle \left\langle \frac{1}{2} \frac{1}{2} \tau_\alpha \tau_\beta \middle| TM_T \right\rangle |n_\alpha l_\alpha j_\alpha, n_\beta l_\beta j_\beta; JM_J, TM_T\rangle, \end{aligned} \tag{3.1.1}$$

where the bracket  $\langle j_1 j_2 m_1 m_2 | jm \rangle$  represents the well know Clebsch-Gordan coefficient, which is subject to the restrictions that  $(j_1, j_2, j)$  be positive integers or half-integers and  $j_1 + j_2 + j$  is an integer.  $j$  represents an angular momentum,

while  $m$  can be thought of intuitively as the quantized projection of the angular momentum along the z-axis. Each  $m_x$  can range from  $-x$  to  $x$ , covering  $2x + 1$  values for any fixed  $x$ . The Clebsch-Gordan coefficients must satisfy the conditions:  $|j_1 - j_2| \leq j \leq j_1 + j_2$  (triangle condition) and  $m_1 + m_2 = m$ . Now we transform the  $jj$  state (3.1.1) to  $LS$  coupling:

$$\begin{aligned}
 & |n_\alpha l_\alpha j_\alpha, n_\beta l_\beta j_\beta; JM_J, TM_T\rangle = \\
 & = \sum_{\lambda S} \sqrt{(2j_\alpha + 1)(2j_\beta + 1)(2\lambda + 1)(2S + 1)} \begin{Bmatrix} l_\alpha & l_\beta & \lambda \\ 1/2 & 1/2 & S \\ j_\alpha & j_\beta & J \end{Bmatrix} \\
 & |n_\alpha l_\alpha, n_\beta l_\beta; \lambda S, JM_J, TM_T\rangle \quad (3.1.2)
 \end{aligned}$$

The symbol

$$\begin{Bmatrix} j_1 & j_2 & J_{12} \\ j_3 & j_4 & J_{34} \\ J_{13} & J_{24} & J \end{Bmatrix}. \quad (3.1.3)$$

represents the  $9j$ -Wigner coefficient and expresses a coupling of angular momenta. It's invariant under reflection of the elements respect to the two diagonals and under exchange of any couple of rows or columns.

Now we need to transform the two-particle state in the center of mass frame. First of all, we introduce the Jacobi coordinate system

$$\mathbf{r}_m = \frac{\mathbf{r}_1 - \mathbf{r}_2}{\sqrt{2}} \quad \mathbf{R}_m = \frac{\mathbf{r}_1 + \mathbf{r}_2}{\sqrt{2}}. \quad (3.1.4)$$

This change of coordinates is characterized by the Jacobian

$$J = \begin{vmatrix} 1/\sqrt{2} & -1/\sqrt{2} \\ 1/\sqrt{2} & 1/\sqrt{2} \end{vmatrix} = 1 \quad (3.1.5)$$

so the equation  $d\mathbf{r}_1 d\mathbf{r}_2 = d\mathbf{R}_m d\mathbf{r}_m$  is valid. We can therefore perform the transformation writing a completeness relation on  $n, l, N$  and  $L$ , which are the relative and center-of-mass motion quantum numbers

$$\begin{aligned}
 |n_\alpha l_\alpha, n_\beta l_\beta; \lambda S, JM_J, TM_T\rangle = \sum_{nlNL} \langle nl, NL; \lambda | n_\alpha l_\alpha, n_\beta l_\beta; \lambda \rangle \\
 |nl, NL; \lambda S, JM_J, TM_T\rangle. \quad (3.1.6)
 \end{aligned}$$

The bracket  $\langle nl, NL; \lambda | n_\alpha l_\alpha, n_\beta l_\beta; \lambda \rangle$  in the case of an harmonic oscillator basis is known as the Moshinsky bracket. In its form is known in the Jacobi coordinate system and it's a simple combination of factorials and Gamma functions. This

bracket is non-vanishing if the energy-conservation condition  $2n + l + 2N + L = 2n_\alpha + l_\alpha + 2n_\beta + l_\beta$  is satisfied. The following conditions are valid

$$\langle nl, NL; \lambda | n_1 l_1, n_2 l_2; \lambda \rangle = (-)^{L-\lambda} \langle nl, NL; \lambda | n_2 l_2, n_1 l_1; \lambda \rangle \quad (3.1.7)$$

$$= (-)^{l_1-\lambda} \langle NL, nl; \lambda | n_1 l_1, n_2 l_2; \lambda \rangle \quad (3.1.8)$$

$$= (-)^{l_1+l} \langle NL, nl; \lambda | n_2 l_2, n_1 l_1; \lambda \rangle \quad (3.1.9)$$

$$= (-)^{l_2+L} \langle n_1 l_1, n_2 l_2; \lambda | nl, NL; \lambda \rangle. \quad (3.1.10)$$

We'll show that the vector bracket from [20] generalizes these relations.

Now we recouple the relative angular momentum to the total spin, considering that the quantum numbers  $l, L$  and  $S$  can be coupled in  $j = l + S$ ,  $\lambda = l + L$  and  $J = \lambda + S = l + L + S$

$$\begin{aligned} |nl, NL, \lambda S; JM_J, TM_T\rangle &= \sum_j |n(lS)j, NL; JM_J, TM_T\rangle \langle (lS)jL; J | (lL)\lambda S; J \rangle = \\ &= \sum_j |n(lS)j, NL; JM_J, TM_T\rangle \sqrt{(2\lambda + 1)(2j + 1)} (-1)^{j+L+S+\lambda} \begin{Bmatrix} j & L & J \\ \lambda & S & l \end{Bmatrix}. \end{aligned} \quad (3.1.11)$$

where the symbol in brackets represents a  $6j$ -Wigner coefficient. These symbols are a generalization of the Clebsch-Gordan coefficients, that arise in the coupling of three angular momenta, and are defined as a sum over products of four  $3j$ -Wigner symbols (which are in turn defined as a symmetrization of the Clebsch-Gordan coefficients).  $6j$ -coefficients have the general form

$$\begin{Bmatrix} j_1 & j_2 & j_3 \\ j_4 & j_5 & j_6 \end{Bmatrix} \quad (3.1.12)$$

in which each triad  $(j_1 j_2 j_3)$ ,  $(j_1 j_5 j_6)$ ,  $(j_4 j_2 j_6)$  and  $(j_4 j_5 j_3)$  satisfies the triangular inequality. Also, they are invariant under permutation of two columns. Decoupling  $J$  and  $M_J$  in  $m_j$  and  $m_L$ , we get

$$|n(lS)j, NL; JM_J, TM_T\rangle = \sum_{m_j m_L} \langle jL, m_j m_L | JM_J \rangle |nlS(j)m_j, NLm_L; TM_T\rangle. \quad (3.1.13)$$

Now let's consider only the relative coordinates, going back to the  $LS$  coupling

$$|nlS(j)m_j\rangle = \sum_{m_S m_l} \langle lS m_l m_S | jm_j \rangle |nlm_l, Sm_S\rangle \quad (3.1.14)$$

Finally we find the ket

$$|nlm_l, NLM_L, Sm_S; TM_T\rangle. \quad (3.1.15)$$

The center-of-mass contribution is simple, because it can be written as a function of mere Dirac deltas

$$\begin{aligned} \langle NLM_L | N'L'm'_L \rangle &= \int d^3 \mathbf{R}_m \int d^3 \mathbf{R}'_m \langle NLM_L | \mathbf{R}_m \rangle \langle \mathbf{R}_m | \mathbf{R}'_m \rangle \langle \mathbf{R}'_m | N'L'm'_L \rangle = \\ &= \int d^3 \mathbf{R}_m \int d^3 \mathbf{R}'_m \varphi_{NLM_L}^*(\mathbf{R}_m) \delta(\mathbf{R}_m - \mathbf{R}'_m) \varphi_{N'L'm'_L}(\mathbf{R}'_m) = \\ &= \int d^3 \mathbf{R}_m \varphi_{NLM_L}^*(\mathbf{R}_m) \varphi_{N'L'm'_L}(\mathbf{R}_m) = \\ &= \int \Omega_{R_m} \int dR_m R_m^2 R_{NL}(R_m) Y_{LM_L}^*(\hat{R}_m) R_{N'L'}(R_m) Y_{L'm'_L}(\hat{R}_m) = \\ &= \int dR_m R_m^2 R_{NL}(R_m) R_{N'L'}(R_m) \delta_{LL'} \delta_{m_L m'_L} = \delta_{NN'} \delta_{LL'} \delta_{m_L m'_L}. \end{aligned}$$

In this calculation we used the orthonormality condition of the spherical harmonics

$$\int d\Omega_r Y_{lm_l}(\Omega_{r_m}^*) Y_{l'm'_l}(\Omega_{r_m}) = \delta_{ll'} \delta_{m_l m'_l}, \quad (3.1.16)$$

and the orthonormality of the radial function. In the harmonic oscillator case, the radial eigenfunction is given by

$$R_{nl}(r) = (-1)^n \sqrt{\frac{2n!}{\Gamma(n+l+3/2)b^3}} \left(\frac{r}{b}\right)^l e^{-(\frac{r}{b})^2} L_n^{l+1/2}\left(\frac{r^2}{b^2}\right), \quad b = \sqrt{\hbar/(m\omega)} \quad (3.1.17)$$

where  $\Gamma$  represents the Gamma function,  $L$  the Laguerre polynomial and  $b = \sqrt{\hbar/(m\omega)}$  is the oscillator length.

Now we consider the relative motion bracket

$$|nlm_l\rangle = \int d^3 q |\mathbf{q}\rangle \langle \mathbf{q} | nlm_l \rangle = \int dq q^2 \int d\hat{q} |\mathbf{q}\rangle \langle \mathbf{q} | nlm_l \rangle.$$

The total wave function in the momentum space can be written separating the radial and angular contributions

$$\Psi_{nlm_l}(\mathbf{q}) = \langle \mathbf{q} | nlm_l \rangle = R_{nl}(q) Y_{lm_l}(\hat{q}).$$

The radial function of the harmonic oscillator is given by

$$R_{nl}(p) = \sqrt{\frac{2n!b^3}{\Gamma(n+l+3/2)}} (pb)^l e^{-\frac{1}{2}(pb)^2} L_n^{l+1/2}((pb)^2)$$

Performing the partial wave expansion of the  $|\mathbf{q}\rangle$ :

$$\begin{aligned} |\mathbf{q}\rangle &= \sum_{l'm'_l} \int dq' q'^2 |q'l'm'_l\rangle \langle q'l'm'_l|\mathbf{q}\rangle = \sum_{l'm'_l} \int dq' q'^2 \frac{\delta(q' - q)}{q'q} Y_{l'm'_l}^*(\hat{q}) |q'l'm'_l\rangle = \\ &= \sum_{l'm'_l} Y_{l'm'_l}^*(\hat{q}) |q'l'm'_l\rangle. \end{aligned}$$

Then

$$\begin{aligned} |nlm_l\rangle &= \sum_{l'm'_l} \int dq q^2 R_{nl}(q) \int d\hat{q} Y_{l'm'_l}^*(\hat{q}) Y_{lm_l}(\hat{q}) |q'l'm'_l\rangle = \\ &= \sum_{l'm'_l} \int dq q^2 R_{nl}(q) \delta_{ll'} \delta_{m_l m'_l} |q'l'm'_l\rangle = \int dq q^2 R_{nl}(q) |qlm_l\rangle, \end{aligned}$$

having used the orthonormality relation of the spherical harmonics.

Finally we can recouple some angular momentum

$$\begin{aligned} |n(lS)j\rangle &= \sum_{m_l m_S} \sum_{j' m'_j} \langle lS m_l m_S | j m_j \rangle \langle lS m_l m_S | j' m'_j \rangle \int dq q^2 R_{nl}(q) |q(lS)j\rangle = \\ &= \sum_{j' m'_j} \delta_{jj'} \delta_{m_j m'_j} \int dq q^2 R_{nl}(q) |q(lS)j\rangle = \int dq q^2 R_{nl}(q) |q(lS)j\rangle. \end{aligned}$$

So we get the final relation for the transformation from the  $nn'$  to the  $qq'$  basis

$$\begin{aligned} \langle n(lS)j; TM_T | \hat{V} | n'(l'S)j; TM_T \rangle &= \\ = \int dq q^2 R_{nl}(q) \int dq' q'^2 R_{n'l'}(q') \langle q(lS)j; TM_T | \hat{V} | q'(l'S)j; TM_T \rangle. \end{aligned}$$

where the oscillator length parameter  $b$  in the radial functions must be multiplied for  $\sqrt{2}$  to compensate the difference between the center of mass and Jacobi coordinates.

In order to find the final potential bracket, we need to write the total antisymmetric function of a two nucleon system, which is a two fermion system which satisfies the Pauli principle. Considering all the possible exchanges of the single-particle indexes, we get the following phases:  $(-)^{j_\alpha + j_\beta - J}$ ,  $(-)^{t_\alpha + t_\beta - T}$  from the Clebsch-Gordan coefficients,  $(-)^{l_\alpha + \beta + s_\alpha + s_\beta + j_\alpha + j_\beta + \lambda + S + J}$  from the  $9j$ -symbol,  $(-)^{\lambda - L}$  from the HO bracket (which we'll show to be valid also in the caso of the vector bracket) and  $(-)^L = (-)^{l_\alpha + l_\beta + l}$  which is the parity condition ( $l + L + l_\alpha + l_\beta = \text{even}$ ). Summing up all the indexes, it follows that the total phase factor is given by  $(-)^{l+S+T}$  and consequently the total antisymmetric

function can be written as

$$|n_\alpha l_\alpha j_\alpha, n_\beta l_\beta j_\beta; JM_J, TM_T\rangle_A = (1 - (-1)^{l+S+T}) |n_\alpha l_\alpha j_\alpha, n_\beta l_\beta j_\beta; JM_J, TM_T\rangle$$

At last, the final normalized expectation value of the potential on the single-particle basis is

$$\begin{aligned} \bar{v}_{\alpha\beta,\gamma\delta}^J &= \left\langle n_\alpha l_\alpha j_\alpha, n_\beta l_\beta j_\beta; JM_J, \tau_\alpha \tau_\beta \left| \hat{V} \right| n_\gamma l_\gamma j_\gamma, n_\delta l_\delta j_\delta; JM_J, \tau_\gamma \tau_\delta \right\rangle_A = \\ &= \frac{1}{\sqrt{1 + \delta_{\alpha\beta}}} \frac{1}{\sqrt{1 + \delta_{\gamma\delta}}} \sum_T \left\langle \frac{1}{2} \frac{1}{2} \tau_\alpha \tau_\beta \left| TM_T \right\rangle \left\langle \frac{1}{2} \frac{1}{2} \tau_\gamma \tau_\delta \left| TM_T \right\rangle \right. \\ &\quad \sum_{\lambda\lambda'S} \sqrt{(2j_\alpha + 1)(2j_\beta + 1)(2j_\gamma + 1)(2j_\delta + 1)(2\lambda + 1)(2\lambda' + 1)(2S + 1)} \\ &\quad \left. \begin{Bmatrix} l_\alpha & l_\beta & \lambda \\ 1/2 & 1/2 & S \\ j_\alpha & j_\beta & J \end{Bmatrix} \begin{Bmatrix} l_\gamma & l_\delta & \lambda' \\ 1/2 & 1/2 & S \\ j_\gamma & j_\delta & J \end{Bmatrix} \sum_{nn'NL\lambda'L} [1 - (-1)^{l+S+T}] \right. \\ &\quad \left. \langle nl, NL; \lambda | n_\alpha l_\alpha, n_\beta l_\beta; \lambda \rangle \langle n'l', NL; \lambda' | n_\gamma l_\gamma, n_\delta l_\delta; \lambda' \rangle \right. \\ &\quad \sum_j (-1)^{\lambda+\lambda'} \sqrt{(2\lambda + 1)(2\lambda' + 1)(2j + 1)} \begin{Bmatrix} j & L & J \\ \lambda & S & l \end{Bmatrix} \begin{Bmatrix} j & L & J \\ \lambda' & S & l' \end{Bmatrix} \\ &\quad \left. \int dq q^2 R_{nl}(q) \int dq' q'^2 R_{n'l'}(q') \left\langle q(lS)j; TM_T \left| \hat{V} \right| q'(l'S)j; TM_T \right\rangle \right. \end{aligned}$$

Where we used the relation

$$\sum_{m_j m_L} \langle jL, m_j m_L | JM_J \rangle \langle jL, m_j m_L | J'M'_J \rangle = \delta_{JJ'} \delta_{M_J M'_J}. \quad (3.1.18)$$

The potential bracket can be further expanded in

$$\begin{aligned} \langle q(lS)j m_j | V | q'(l'S)j m_j \rangle &= \\ &= \int d\hat{q} d\hat{q}' \sum_{\sigma_1 \sigma_2} \sum_{\sigma'_1 \sigma'_2} j_l(qr) j_{l'}(q'r') Y_{lm}(\hat{q}) \chi_{m_S}^S(\sigma_1, \sigma_2) \hat{V} \chi_{m_S}^S(\sigma'_1, \sigma'_2) Y_{l'm'_l}(\hat{q}') \\ &\quad \sum_{m_l m_S} \langle l'S m'_l m_S | j m_j \rangle \sum_{m'_l m'_S} \langle lS m_l m_S | j m_j \rangle. \end{aligned}$$

The quantum numbers  $j$ ,  $m_j$ ,  $S$ ,  $m_S$ ,  $J$ ,  $M_J$ ,  $T$ , and  $M_T$  are conserved by the NN interaction.  $N$ ,  $L$  and  $m_L$  are conserved by orthogonality of the center-of-mass wave function. In general  $n \neq n'$ ,  $l \neq l'$ ,  $m_l \neq m'_l$  and  $\lambda \neq \lambda'$ .

### 3.2 Nuclear potential matrix elements in $jj$ coupling for a general basis

Now we want to recalculate the matrix elements we have just seen for a general basis. First of all we need to write down an expression equivalent to the one we've just seen in the case of the HO brackets, as a function of the Wong-Clement brackets  $\langle (s_1 s_2) r_a l (t_1 t_2) r_b L; \lambda | n_1 l_1 n_2 l_2; \lambda \rangle$  for the general coordinate system

$$\begin{cases} \mathbf{r}_1 = s_1 \mathbf{r}_a + t_1 \mathbf{r}_b \\ \mathbf{r}_2 = s_2 \mathbf{r}_a + t_2 \mathbf{r}_b \end{cases} \quad (3.2.1)$$

We define the Jacobi coordinates as

$$\begin{cases} \mathbf{r}_w = \frac{\mathbf{r}_1 - \mathbf{r}_2}{\sqrt{2}} \\ \mathbf{R}_w = \frac{\mathbf{r}_1 + \mathbf{r}_2}{\sqrt{2}} \end{cases}$$

and the center of mass coordinates

$$\begin{cases} \mathbf{r} = \sqrt{2} \mathbf{r}_w = \mathbf{r}_1 - \mathbf{r}_2 \\ \mathbf{R} = \frac{\mathbf{R}_w}{\sqrt{2}} = \frac{\mathbf{r}_1 + \mathbf{r}_2}{2} \end{cases}$$

Choosing  $\mathbf{r}_a = \mathbf{r}$  and  $\mathbf{r}_b = \mathbf{R}$ , it follows that  $t_1 = t_2 = 1$  and  $s_1 = -s_2 = 1/2$  for the center of mass system. If we consider the mass difference between the two particles (this is the case of the proton-neutron system), the coordinate parameters are written as  $s_1 = m_n/(m_p + m_n)$  and  $s_2 = -m_p/(m_p + m_n)$ . If we want to use instead the Jacobi system, we have to put  $\mathbf{r}_a = \mathbf{r}_w$  and  $\mathbf{r}_b = \mathbf{R}_w$ , which leads to  $t_1 = t_2 = 1/\sqrt{2}$  and  $s_1 = -s_2 = 1/\sqrt{2}$ . In the following we'll use always the center-of-mass frame, because the nuclear interaction that we're using is given in that system.

For the wave-functions we'll use the convention

$$\Phi_{nlm}(\mathbf{r}) = \langle \mathbf{r} | nlm \rangle = u_{nl}(r) Y_m^l(\hat{r}) = \frac{1}{r} R_{nl}(r) Y_m^l(\hat{r}) = \frac{1}{r} \langle rl | nl \rangle Y_m^l(\hat{r}).$$

The angular part calculations are identical to the ones we have already seen in the HO case. We just need to write down the radial part

$$|n_\alpha l_\alpha n_\beta l_\beta; \lambda \rangle = \int dR dr \sum_{lL} |rlRL; \lambda \rangle \langle (s_1 s_2) rl(t_1 t_2) RL; \lambda | n_\alpha l_\alpha n_\beta l_\beta; \lambda \rangle, \quad (3.2.2)$$

where  $|rlRL; \lambda \rangle \langle (s_1 s_2) rl(t_1 t_2) RL; \lambda | n_\alpha l_\alpha n_\beta l_\beta; \lambda \rangle$  is the Wong-Clement coefficient

cient. Here the orthonormality of the barycentral wave function leads to

$$\langle R'L'm'_L | R L m_L \rangle = \delta_L(R - R') \delta_{L'L'} \delta_{m_L m'_L} \quad (3.2.3)$$

$$\text{with} \quad \delta_L(R - R') = R R' \frac{2}{\pi} \int j_L(kR) j_L(kR') k^2 dk. \quad (3.2.4)$$

Performing the same calculations already seen for the radial part, we get to the equation

$$\begin{aligned} & \hat{V} |n_\alpha l_\alpha, n_\beta l_\beta; \lambda S, J M_J, \tau_\alpha \tau_\beta \rangle = \\ & = \sum_{T M_T} \left\langle \frac{1}{2} \frac{1}{2} \tau_\alpha \tau_\beta \left| T M_T \right. \right\rangle \sum_{\lambda S} \sqrt{(2j_\alpha + 1)(2j_\beta + 1)(2\lambda + 1)(2S + 1)} \left\{ \begin{array}{ccc} l_\alpha & l_\beta & \lambda \\ 1/2 & 1/2 & S \\ j_\alpha & j_\beta & J \end{array} \right\} \\ & \quad \int dR dr \sum_{lL} \langle r l R L | n_\alpha l_\alpha n_\beta l_\beta; \lambda \rangle \sum_j \sum_{m_j m_L} \langle j L, m_j m_L | J M_J \rangle \\ & \quad \sqrt{(2\lambda + 1)(2j + 1)} (-1)^{j+L+S+\lambda} \left\{ \begin{array}{ccc} j & L & J \\ \lambda & S & l \end{array} \right\} \hat{V} |r, (lS) j m_j, R L m_L; T M_T \rangle. \end{aligned} \quad (3.2.5)$$

Now we're almost done with the potential matrix elements. We just need to show that the antisymmetric term is the same as in the HO case (Wong and Clement noticed in [20] that their brackets include the same symmetry of the Moshinsky brackets). We know that the parity condition  $l_\alpha + l_\beta + l + L = \text{even}$  is satisfied by the function  $A_{II}(x)$  included in those coefficients, but we need to prove an equation analogous to

$$\langle nl, NL; \lambda | n_1 l_1, n_2 l_2; \lambda \rangle = (-)^{\lambda-L} \langle nl, NL; \lambda | n_2 l_2, n_1 l_1; \lambda \rangle, \quad (3.2.6)$$

which is, we need to prove that

$$\langle (s_1 s_2) r l, (t_1 t_2) R L; \lambda | n_1 l_1, n_2 l_2; \lambda \rangle = (-)^{\lambda-L} \langle (s_1 s_2) r l, (t_1 t_2) R L; \lambda | n_2 l_2, n_1 l_1; \lambda \rangle. \quad (3.2.7)$$

We start from the symmetry relations for the vector bracket written in [20],

which are

$$\langle (s_1 s_2)rl(t_1 t_2)RL; \lambda | r_\alpha l_\alpha r_\beta l_\beta; \lambda \rangle = (-)^{l_\alpha + l_\beta - \lambda} \langle (s_2 s_1)rl(t_2 t_1)RL; \lambda | r_\beta l_\beta r_\alpha l_\alpha; \lambda \rangle \quad (3.2.8)$$

$$= (-)^{l+L-\lambda} \langle (t_1 t_2)RL(s_1 s_2)rl; \lambda | r_\alpha l_\alpha r_\beta l_\beta; \lambda \rangle \quad (3.2.9)$$

$$= (-)^l \langle (-s_1 -s_2)rl(t_1 t_2)RL; \lambda | r_\alpha l_\alpha r_\beta l_\beta; \lambda \rangle \quad (3.2.10)$$

$$= (-)^{l_\alpha} \langle (-s_1 s_2)rl(-t_1 t_2)RL; \lambda | r_\alpha l_\alpha r_\beta l_\beta; \lambda \rangle \quad (3.2.11)$$

In particular, we need the first and the third ones and we need two show that they are still valid for the Wong-Clement coefficients, writing them as a function of the vector brackets

$$\begin{aligned} & \langle (s_1 s_2)rl(t_1 t_2)RL; \lambda | n_\alpha l_\alpha n_\beta l_\beta; \lambda \rangle = \\ & = \int dr_\alpha dr_\beta \langle (s_1 s_2)rl(t_1 t_2)RL; \lambda | r_\alpha l_\alpha r_\beta l_\beta; \lambda \rangle \langle r_\alpha l_\alpha r_\beta l_\beta; \lambda | n_\alpha l_\alpha n_\beta l_\beta; \lambda \rangle. \end{aligned} \quad (3.2.12)$$

From eq. (3.2.10) it's immediate to find that

$$\langle (s_1 s_2)rl(t_1 t_2)RL; \lambda | n_\alpha l_\alpha n_\beta l_\beta; \lambda \rangle = (-)^l \langle (-s_1 -s_2)rl(t_1 t_2)RL; \lambda | n_\alpha l_\alpha n_\beta l_\beta; \lambda \rangle. \quad (3.2.13)$$

In order to get the Wong-Clement analogous of eq. (3.2.8), we just need to notice that the bracket  $\langle r_\alpha l_\alpha r_\beta l_\beta; \lambda | n_\alpha l_\alpha n_\beta l_\beta; \lambda \rangle$  is separable and independent from  $\lambda$ , which allows us to write  $\langle r_\alpha l_\alpha r_\beta l_\beta; \lambda | n_\alpha l_\alpha n_\beta l_\beta; \lambda \rangle = \langle r_\alpha l_\alpha | n_\alpha l_\alpha \rangle \langle r_\beta l_\beta | n_\beta l_\beta \rangle = \langle r_\beta l_\beta | n_\beta l_\beta \rangle \langle r_\alpha l_\alpha | n_\alpha l_\alpha \rangle = \langle r_\beta l_\beta r_\alpha l_\alpha; \lambda | n_\beta l_\beta n_\alpha l_\alpha; \lambda \rangle$  It's then immediate to find the simmetry relation

$$\langle (s_1 s_2)rl(t_1 t_2)RL; \lambda | n_\alpha l_\alpha n_\beta l_\beta; \lambda \rangle = (-)^{l_\alpha + l_\beta - \lambda} \langle (s_2 s_1)rl(t_2 t_1)RL; \lambda | n_\alpha l_\alpha n_\beta l_\beta; \lambda \rangle. \quad (3.2.14)$$

Finally, combining eqs. (3.2.13) and (3.2.14) we find

$$\begin{aligned} \langle (s_1 s_2)r_\alpha l_\alpha(t_1 t_2)r_\beta l_\beta; \lambda | n_\alpha l_\alpha n_\beta l_\beta; \lambda \rangle &= (-)^{l_1 + l_2 - \lambda} \langle (s_2 s_1)r_\alpha l_\alpha(t_2 t_1)r_\beta l_\beta; \lambda | n_\beta l_\beta n_\alpha l_\alpha; \lambda \rangle = \\ &= (-)^{l_1 + l_2 - \lambda} (-)^l \langle (-s_2 -s_1)r_\alpha l_\alpha(t_1 t_2)r_\beta l_\beta; \lambda | n_\beta l_\beta n_\alpha l_\alpha; \lambda \rangle = \\ &= (-)^{l_1 + l_2 - \lambda} (-)^l \langle (s_1 s_2)r_\alpha l_\alpha(t_1 t_2)r_\beta l_\beta; \lambda | n_\beta l_\beta n_\alpha l_\alpha; \lambda \rangle = \\ &= (-)^{\lambda - L} \langle (s_1 s_2)r_\alpha l_\alpha(t_1 t_2)r_\beta l_\beta; \lambda | n_\beta l_\beta n_\alpha l_\alpha; \lambda \rangle \end{aligned}$$

where we used both the parity condition ( $l_\alpha + l_\alpha + l + L = \text{even}$ ) and the identities  $s_1 = -s_2$  and  $t_1 = t_2$  which are always valid in the Jacobi and center-of-mass frames. Then it follows the same antisymmetry relation for the wave function seen in the HO case.

$$\begin{aligned}
 \bar{v}_{\alpha\beta,\gamma\delta}^J &= \left\langle n_\alpha l_\alpha j_\alpha, n_\beta l_\beta j_\beta; JM_J, \tau_\alpha \tau_\beta \left| \hat{V} \right| n_\gamma l_\gamma j_\gamma, n_\delta l_\delta j_\delta; JM_J, \tau_\gamma \tau_\delta \right\rangle_A = \\
 &= \frac{1}{\sqrt{1+\delta_{\alpha\beta}}} \frac{1}{\sqrt{1+\delta_{\gamma\delta}}} \sum_T \left\langle \frac{1}{2} \frac{1}{2} \tau_\alpha \tau_\beta \left| TM_T \right\rangle \left\langle \frac{1}{2} \frac{1}{2} \tau_\gamma \tau_\delta \left| TM_T \right\rangle \right. \\
 &\quad \sum_{\lambda\lambda'S} \sqrt{(2j_\alpha+1)(2j_\beta+1)(2j_\gamma+1)(2j_\delta+1)(2\lambda+1)(2\lambda'+1)(2S+1)} \\
 &\quad \left\{ \begin{matrix} l_\alpha & l_\beta & \lambda \\ 1/2 & 1/2 & S \\ j_\alpha & j_\beta & J \end{matrix} \right\} \left\{ \begin{matrix} l_\gamma & l_\delta & \lambda' \\ 1/2 & 1/2 & S \\ j_\gamma & j_\delta & J \end{matrix} \right\} \int dr dr' dR \sum_{u'L} [1 - (-1)^{l+S+T}] \\
 &\quad \langle r l, RL; \lambda | n_\alpha l_\alpha, n_\beta l_\beta; \lambda \rangle^* \langle r' l', RL; \lambda' | n_\gamma l_\gamma, n_\delta l_\delta; \lambda' \rangle \\
 &\quad \sum_j (-1)^{\lambda+\lambda'} \sqrt{(2\lambda+1)(2\lambda'+1)(2j+1)} \left\{ \begin{matrix} j & L & J \\ \lambda & S & l \end{matrix} \right\} \left\{ \begin{matrix} j & L & J \\ \lambda' & S & l' \end{matrix} \right\} \\
 &\quad \left\langle r', (S'l')j; TM_T \left| \hat{V} \right| r, (Sl)j; TM_T \right\rangle. \quad (3.2.15)
 \end{aligned}$$

Considering that we're mostly using potentials given in the momentum space, we need to write those elements performing a double Hankel transform in the momentum coordinates

$$\begin{aligned}
 &\left\langle r', (S'l')j; TM_T \left| \hat{V} \right| r, (Sl)j; TM_T \right\rangle = \\
 &= \frac{2}{\pi} r r' \int dq dq' q^2 q'^2 j_\nu(q'r') j_l(qr) \left\langle q', (S'l')j; TM_T \left| \hat{V} \right| q, (Sl)j; TM_T \right\rangle. \quad (3.2.16)
 \end{aligned}$$

### 3.3 The Wong-Clement coefficients

In this section we are going to discuss the mathematical foundation of the coupling coefficients we have previously seen, the various forms they can assume and which one is the most suitable for numerical calculations.

First of all, we introduce some notations. We consider the general transformation

$$\begin{cases} \mathbf{r}_1 = s_1 \mathbf{r}_a + t_1 \mathbf{r}_b = \varrho_1(\mathbf{r}_a, \mathbf{r}_b) \\ \mathbf{r}_2 = s_2 \mathbf{r}_a + t_2 \mathbf{r}_b = \varrho_2(\mathbf{r}_a, \mathbf{r}_b) \end{cases} \quad (3.3.1)$$

which is represented by the vector bracket  $\langle (s_1 s_2) \mathbf{r}_a l (t_1 t_2) \mathbf{r}_b L, \lambda | \mathbf{r}_1 l_1 \mathbf{r}_2 l_2, \lambda \rangle$ . This bracket is the vector analog of the Moshinsky bracket. The Wong-Clement

coefficients are a generalization of Moshinsky brackets in the sense that they are written in a general coordinate system for any orthonormal basis. Here the indexes 1 and 2 represents two single-particle states, while  $a$  and  $b$  refer to the coordinate of a second coordinate system (p.e. center-of-mass or Jacobi). The particular choice of the system is specified by the scale factors  $s_i, t_i$ .

Starting from this three-dimensional radial vector, it can be expanded in the angular momentum as

$$\langle \mathbf{r} | = \frac{1}{r} \sum_{lm} \langle rlm | Y_m^l(\hat{r}), \quad (3.3.2)$$

where the radial ket satisfies the orthonormality condition

$$\langle rlm | r'l'm' \rangle = \delta_{ll'} \delta_{mm'} \delta(r - r'). \quad (3.3.3)$$

For the three-dimensional coordinate-space wave function we will use the notation

$$\varphi_{nlm}(\mathbf{r}) = \frac{1}{r} R_{nl}(r) Y_m^l(\hat{r}), \quad (3.3.4)$$

which can be written in the bracket notation as

$$\langle \mathbf{r} | nlm \rangle = \frac{1}{r} \langle rl | nl \rangle Y_m^l(\hat{r}), \quad (3.3.5)$$

where  $\langle rl | nl \rangle = \langle rlm | nlm \rangle = R_{nl}(r)$  represents the total radial contribution to the wave function multiplied by  $r$  and is independent from  $m$  for the orthogonality condition (3.3.3).

Switching to a two vectors (particles) system, the coupled angular momentum representation is

$$\langle \mathbf{r}_1 \mathbf{r}_2 | = \frac{1}{r_1 r_2} \sum_{l_1 l_2 \lambda \mu} \langle r_1 l_1 r_2 l_2, \lambda \mu | [Y^{l_1}(\hat{r}_1) Y^{l_2}(\hat{r}_2)]_{\mu}^{\lambda} \rangle. \quad (3.3.6)$$

As above, the radial bracket satisfies the orthonormality condition

$$\langle r_1 l_1 r_2 l_2, \lambda \mu | r'_1 l'_1 r'_2 l'_2, \lambda' \mu' \rangle = \delta_{l_1 l'_1} \delta_{l_2 l'_2} \delta_{\lambda \lambda'} \delta_{\mu \mu'} \delta(r_1 - r'_1) \delta(r_2 - r'_2). \quad (3.3.7)$$

In order to obtain an analytic expression of the Wong-Clement bracket, we start considering the Dirac bracket

$$\begin{aligned} \langle (s_1 s_2) \mathbf{r}_a (t_1 t_2) \mathbf{r}_b | \mathbf{r}_1 \mathbf{r}_2 \rangle &= (r_a r_b r_1 r_2)^{-1} \sum_{\lambda \mu \lambda' \mu'} \sum_{l l_1 l_2} [Y^l(\hat{r}_a) \times Y^L(\hat{r}_b)]_{\mu}^{\lambda} \\ &\cdot [Y^{l_1}(\hat{r}_1) \times Y^{l_2}(\hat{r}_2)]_{\mu'}^{\lambda'} \langle (s_1 s_2) r_a l (t_1 t_2) r_b L, \lambda \mu | r_1 l_1 r_2 l_2, \lambda' \mu' \rangle, \end{aligned} \quad (3.3.8)$$

which is invariant under rotation of each axis. This basic property, noticed by

Balian-Brezin, is essential to obtain the final analytical form of the coefficients.

Now, the radial part of the Dirac bracket can be isolated reversing the previous equation integrating over the four angles

$$\begin{aligned} \langle r_a l r_b L, \lambda \mu | r_1 l_1 r_2 l_2, \lambda' \mu' \rangle &= r_a r_b r_1 r_2 \int d^2 \hat{r}_a d^2 \hat{r}_b d^2 \hat{r}_1 d^2 \hat{r}_2 [Y^l(\hat{r}_a) \times Y^L(\hat{r}_b)]_\mu^\lambda \cdot \\ &\cdot [Y^{l_1}(\hat{r}_1) \times Y^{l_2}(\hat{r}_2)]_{\mu'}^{\lambda'} \langle r_a r_b | r_1 r_2 \rangle. \end{aligned} \quad (3.3.9)$$

This is the so called *vector bracket*. The rotational invariance that we previously required now implies that

$$\langle r_a l r_b L, \lambda \mu | r_1 l_1 r_2 l_2, \lambda' \mu' \rangle = \delta_{\lambda \lambda'} \delta_{\mu \mu'} \langle r_a l r_b L, \lambda | r_1 l_1 r_2 l_2, \lambda \rangle. \quad (3.3.10)$$

This equation can be further expanded, considering the bracket

$$\langle (s_1 s_2) \mathbf{r}_a (t_1 t_2) \mathbf{r}_b | \mathbf{r}_1 \mathbf{r}_2 \rangle = \delta[\mathbf{r}_1 - \boldsymbol{\varrho}_1(\mathbf{r}_a, \mathbf{r}_b)] \delta[\mathbf{r}_2 - \boldsymbol{\varrho}_2(\mathbf{r}_a, \mathbf{r}_b)]. \quad (3.3.11)$$

We will deal separately with the radial and the angular part. The radial part simplifies into

$$\begin{aligned} (r_1 r_2)^{-2} \delta(r_1 - |\boldsymbol{\varrho}_1|) \delta(r_2 - |\boldsymbol{\varrho}_2|) &= 2(r_a r_b r_1 r_2)^{-1} \delta(w) \delta(\cos \vartheta_{ab} - x) = \\ &= (r_a r_b r_1 r_2)^{-1} \delta(w) \vartheta(1 - x^2) \sum_{\mathfrak{L}=0}^{+\infty} (2\mathfrak{L} + 1) P_{\mathfrak{L}}(\cos \vartheta_{ab}) P_{\mathfrak{L}}(x), \end{aligned} \quad (3.3.12)$$

where we used the Legendre functions expansion of the Dirac delta

$$\sum_{l=0}^{+\infty} \frac{2l+1}{2} P_l(x) P_l(y) = \delta(x - y), \quad (3.3.13)$$

which is a completeness over the range  $x = -1 \dots 1$  (the term  $\vartheta(1 - x^2)$  derives from here). From the definition of the  $\varrho$  functions, it follows that

$$w = s_2 t_2 r_1^2 - s_1 t_1 r_2^2 + (t_1 s_2 - t_2 s_1)(s_1 s_2 r_a^2 - t_1 t_2 r_b^2) \quad (3.3.14)$$

$$x = \frac{r_i^2 - s_i^2 r_a^2 - t_i^2 r_b^2}{2s_i t_i r_a r_b}, \quad i=1,2 \quad (3.3.15)$$

Concerning the angular part

$$\sum_{l_1 l_2 \lambda \mu} [Y^{l_1}(\hat{r}_1) \times Y^{l_2}(\hat{r}_2)]_\mu^{\lambda*} [Y^{l_1}(\hat{\varrho}_1) \times Y^{l_2}(\hat{\varrho}_2)]_\mu^\lambda, \quad (3.3.16)$$

we can use the spherical harmonics identity found by [23]

$$|s\mathbf{r}_a + t\mathbf{r}_b|^l Y_m^l(s\mathbf{r}_a + t\mathbf{r}_b) = \sum_{k=0}^l \left[ \frac{4\pi}{2k+1} \binom{2l+1}{2k} \right]^{1/2} (s r_a)^k (t r_b)^{l-k} \cdot [Y^k(\hat{r}_a) \times Y^{l-k}(\hat{r}_b)]_m^l. \quad (3.3.17)$$

Now we need two other identities involving the spherical harmonics, one for each couple of harmonics included in equation (3.3.16). The first one follows immediately from the relation we have just seen

$$[Y^{l_1}(\hat{\rho}_1) \times Y^{l_2}(\hat{\rho}_2)]_\mu^\lambda = \left( \frac{t_1 r_b}{r_1} \right)_1^l \left( \frac{t_2 r_b}{r_2} \right)_2^l \sum_{l' L'} [Y^{l'}(\hat{r}_a) \times Y^{L'}(\hat{r}_b)]_\mu^\lambda B(l' L' l_1 l_2, \lambda; yz), \quad (3.3.18)$$

where  $B$  is an angular momentum coupling function:

$$B(l' L' l_1 l_2, \lambda; yz) = (-)^{l'+L'} (2l_1+1)(2l_2+2) \sqrt{(2l'+1)(2L'+1)} \sum_{kk'} \times \binom{2l_1}{2k}^{1/2} \binom{2l_2}{2k'}^{1/2} \begin{pmatrix} k & k' & l' \\ 0 & 0 & 0 \end{pmatrix} \begin{pmatrix} l_1-k & l_2-k' & L' \\ 0 & 0 & 0 \end{pmatrix} \left\{ \begin{matrix} k & l_1-k & l_1 \\ k' & l_2-k' & l_2 \\ l' & L' & \lambda \end{matrix} \right\} \quad (3.3.19)$$

, where the variables

$$y = \frac{s_1 r_a}{t_1 r_b} \quad z = \frac{s_2 t_1}{s_1 t_2} \quad (3.3.20)$$

depend only on the reference system.

The second identity we need to simplify equation (3.3.16) is

$$P_\Sigma(\cos(\vartheta_{ab})) [Y^{l'}(\hat{r}_a) \times Y^{L'}(\hat{r}_b)]_\mu^\lambda = (-)^{\Sigma+\lambda} \sum_{lL} [Y^l(\hat{r}_a) \times Y^L(\hat{r}_b)]_\mu^\lambda \sqrt{(2l+1)(2L+1)(2l'+1)(2L'+1)} \cdot \begin{pmatrix} l & \Sigma & l' \\ 0 & 0 & 0 \end{pmatrix} \begin{pmatrix} L & \Sigma & L' \\ 0 & 0 & 0 \end{pmatrix} \left\{ \begin{matrix} l & L & \lambda \\ L' & l' & \Sigma \end{matrix} \right\}. \quad (3.3.21)$$

This relation can be proven starting by the triple spherical harmonics completeness relation

$$\int Y_{m_1}^{l_1}(\vartheta, \varphi) Y_{m_2}^{l_2}(\vartheta, \varphi) Y_{m_3}^{l_3}(\vartheta, \varphi) d\Omega = \left[ \frac{(2l_1+1)(2l_2+1)(2l_3+1)}{4\pi} \right]^{1/2} \begin{pmatrix} l_1 & l_2 & l_3 \\ 0 & 0 & 0 \end{pmatrix} \begin{pmatrix} l_1 & l_2 & l_3 \\ m_1 & m_2 & m_3 \end{pmatrix}. \quad (3.3.22)$$

from which it follows that

$$Y_{m_1}^{l_1}(\vartheta, \varphi) Y_{m_2}^{l_2}(\vartheta, \varphi) = \sum_{LM} (-)^M \left[ \frac{(2l_1+1)(2l_2+1)(2L+1)}{4\pi} \right]^{1/2} \begin{pmatrix} l_1 & l_2 & L \\ 0 & 0 & 0 \end{pmatrix} \begin{pmatrix} l_1 & l_2 & L \\ m_1 & m_2 & M \end{pmatrix} Y_{L,-M}(\vartheta, \varphi), \quad (3.3.23)$$

where the quantum number  $L$  express the coupling of the two orbital angular momenta  $l_1$  and  $l_2$ .

Finally, we can put together the angular and radial parts to obtain

$$\langle (s_1 s_2) r_a l(t_1 t_2) r_b L, \lambda | r_1 l_1 r_2 l_2, \lambda \rangle = \langle I | I I \rangle = (4\pi)^2 \delta(w) \vartheta(1-x^2) A_{I I I}(x). \quad (3.3.24)$$

The function  $A_{I I I}(x)$  represents the main part of the Wong-Clement coefficients. We'll discuss some analytical forms in which this coefficients can be written, but at the moment we just write the expression by [20], which follows from the previous calculations

$$A_{I I I}(x) = \frac{1}{4\pi^2} \sum_{\mathfrak{L}=0}^{\mathfrak{L}_{max}} (2\mathfrak{L}+1) P_{\mathfrak{L}}(x) (1+2xy+y^2)^{-\frac{1}{2}l_1} (1+2xyz+y^2z^2)^{-\frac{1}{2}l_2} G_{\mathfrak{L}}(l l l_1 l_2, \lambda; yz) \quad (3.3.25)$$

where

$$G_{\mathfrak{L}}(l l l_1 l_2, \lambda; yz) = (-)^{\mathfrak{L}+\lambda} \sqrt{(2l+1)(2L+1)} \sum_{l' L'} \sqrt{(2l'+1)(2L'+1)} \begin{pmatrix} l & \mathfrak{L} & l' \\ 0 & 0 & 0 \end{pmatrix} \begin{pmatrix} L & \mathfrak{L} & L' \\ 0 & 0 & 0 \end{pmatrix} \begin{Bmatrix} l & L & \lambda \\ L' & l' & \mathfrak{L} \end{Bmatrix}. \quad (3.3.26)$$

with  $\mathfrak{L}_{max} = l_1 + l_2 + \min(l, L)$ . This function includes all the contributes deriving from the angular momenta couplings. The bracket (3.3.24) satisfies the simmetry conditions (3.2.8) that we have seen in the previous section, while the function  $A(x)$  satisfies the parity condition.

Now we want to express the Wong-Clement bracket  $\langle (s_1 s_2) r_a l(t_1 t_2) r_b L, \lambda | n_1 l_1 n_2 l_2, \lambda \rangle$  as a function of the vector bracket we have just determined. We can do this using the completeness relation

$$\langle (s_1 s_2) r_a l(t_1 t_2) r_b L, \lambda | n_1 l_1 n_2 l_2, \lambda \rangle = \int \int \langle (s_1 s_2) r_a l(t_1 t_2) r_b L, \lambda | r_1 l_1 r_2 l_2, \lambda \rangle \cdot \langle r_1 l_1 r_2 l_2, \lambda | n_1 l_1 n_2 l_2 \rangle dr_1 dr_2, \quad (3.3.27)$$

where the left bracket has just been discussed and the right bracket is a product

of two radial functions ( $u_{nl}(r) = r^{-1} \langle rl|nl \rangle$ ). Putting inside this equation the expression of the vector bracket (3.3.24), we find from the delta function that  $x = \cos \vartheta_{ab}$ , so we can identify the variable  $x$  as the cosine of the angle between  $r_a$  and  $r_b$ . Thus  $x$  can be expressed as a function of  $r_1$  and  $r_2$ , with the help of the other delta function  $\delta(w)$ . Finally we can express the double integral over  $r_1$  and  $r_2$  as a single integral over  $x$ , with the substitution

$$dx = (s_1 t_1 r_a r_b)^{-1} r_1 dr_1, \quad (3.3.28)$$

and our final expression for the Wong-Clement coefficient, which is the more general one, is

$$\langle (s_1 s_2) r_a l (t_1 t_2) r_b L, \lambda | n_1 l_1 n_2 l_2, \lambda \rangle = 8\pi^2 r_a r_b \int_{-1}^1 dx u_{n_1 l_1 n_2 l_2}(r_1, r_2) A_{III}(x). \quad (3.3.29)$$

### 3.3.1 Various expressions of $A_{III}(x)$

Now we will discuss different ways in which the function  $A_{III}(x)$  can be expressed. First of all, we start from the more general form in which this coefficient can be written, which is due to Balian and Brezin [21]

$$A_{III}(x) = (2\lambda + 1)^{-1} \sum_{\mu} [Y^l(\hat{r}_a) \times Y^L(\hat{r}_b)]_{\mu}^{\lambda*} [Y^{l_1}(\hat{r}_1) \times Y^{l_2}(\hat{r}_2)]_{\mu}^{\lambda}. \quad (3.3.30)$$

All the expressions that we are going to see are a consequence of rotational invariance of this function (which is then a scalar function).

- The first expression is due to Wong and Clement, and correspond to put directly in the equation (3.3.29) the expression (3.3.25)

$$\begin{aligned} \langle (s_1 s_2) r_a l (t_1 t_2) r_b L, \lambda | n_1 l_1 n_2 l_2, \lambda \rangle &= \frac{1}{2} r_a r_b \sum_{\mathfrak{L}=0}^{\mathfrak{L}_{max}} (2\mathfrak{L}+1) G_{\mathfrak{L}}(l l l_1 l_2, \lambda; yz) \cdot \\ &\cdot \int_{-1}^1 dx u_{n_1 l_1 n_2 l_2}(r_1, r_2) \left( \frac{t_1 r_b}{r_1} \right)^{l_1} \left( \frac{t_2 r_b}{r_2} \right)^{l_2}. \end{aligned} \quad (3.3.31)$$

The single-particle coordinates  $r_1, r_2$  can be expressed as a function of the  $r_b$  coordinate and the variables  $x, y, z$

$$\begin{cases} r_1 = t_1 r_b (1 + 2xy + y^2)^{1/2} \\ r_2 = t_2 r_b (1 + 2xyz + y^2 z^2)^{1/2} \end{cases} \quad (3.3.32)$$

- The second expression is a generalization by Wong-Clement [24]. Bay-

man and Kallio found an easy formula for isolating the relative-angular-momentum-zero part of the wave function of two particles in a single-particle potential. This method is generalized for the case  $l \neq 0$ . First of all we start from the identity

$$\begin{aligned} (r_1 r_2)^{-1} \langle r_1 l_1 r_2 l_2 | n_1 l_1 n_2 l_2 \rangle [Y^{l_1}(\hat{r}_1) \times Y^{l_2}(\hat{r}_2)]_\mu^\lambda = \\ (r_a r_b)^{-1} \sum_{lL} \langle (s_1 s_2) r_a l (t_1 t_2) r_b L, \lambda | n_1 l_1 n_2 l_2, \lambda \rangle [Y^l(\hat{r}_a) \times Y^L(\hat{r}_b)]_\mu^\lambda. \end{aligned} \quad (3.3.33)$$

Now we need to isolate the states for a given value of  $l$ . We can do this multiplying the two sides of the equation by  $[Y_m^l(\hat{r}_a)]^*$  and integrating over  $\hat{r}_a$ . The spherical harmonic have the general form

$$Y_m^l(\vartheta, \varphi) = e^{im\varphi} d_{m,0}^l(\vartheta) \left( \frac{2l+1}{4\pi} \right)^{1/2}, \quad (3.3.34)$$

where

$$\begin{aligned} d_{m,0}^l(\vartheta) = \sum_{n=m}^l (-1)^n \frac{l![(l+m)!(l-m)!]^{1/2}}{n!(l+m-n)!(l-n)!(n-m)!} \\ (\cos \frac{1}{2}\vartheta)^{2l+m-2n} (\sin \frac{1}{2}\vartheta)^{2n-m}. \end{aligned} \quad (3.3.35)$$

Also, we can use the property of rotational invariance of  $A_{II}(x)$ , setting the  $r_b$  axis parallel to the  $x$  axis. In this way the spherical harmonic in  $L$  is simplified into

$$Y_M^L(0, 0) = \delta_{M0} \left( \frac{2L+1}{4\pi} \right)^{1/2} \quad \text{and } m = \mu. \quad (3.3.36)$$

Now we notice that from (3.3.1),  $\varphi_i = \varphi + n_i \pi$  with  $n_i = 1, 2$ , where  $n_i = 0$  if  $s_i > 0$  and  $n_i = 1$  if  $s_i < 0$ . Then the integral is independent of  $\varphi$  and the integral over the angle  $\hat{r}_a$  gives

$$\begin{aligned} \langle (s_1 s_2) r_a l (t_1 t_2) r_b L, \lambda | n_1 l_1 n_2 l_2, \lambda \rangle = \\ = \frac{1}{2} r_a r_b \frac{(2l_1+1)(2l_2+1)(2l+1)}{2\lambda+1} \sum_{mm_1} (-)^{l+(n_2-1)m+(n_1-n_2)m_1} \\ \langle \lambda m l - m | L 0 \rangle \langle l_1 m_1 l_2 m - m_1 | \lambda m \rangle \int_{-1}^1 u_{n_1 l_1 n_2 l_2}(r_1, r_2) d_{m_1,0}^{l_1}(\vartheta_1) d_{m_2,0}^{l_2}(\vartheta_2) \\ \cdot d_{m,0}^l(\cos^{-1} x) dx, \end{aligned} \quad (3.3.37)$$

with  $\cos \vartheta_i = r_i^{-1}(s_1 r_1 x + t_i r_b)$ .

- The third expression corresponds to set all the vectors in the plane  $xOy$  with the center of mass vector  $r_b = R$  along the  $z$ -axis. With this configuration, the azimuthal angle of the spherical harmonics in (3.3.30) is just 0 or  $\pi$ , based on the  $x$  component of the vector. The expression (3.3.30) is then simplified into

$$A(x) = \frac{1}{2\lambda + 1} \sum_{\mu m_1 m_2} \langle l_1 l_2 m_1 m_2 | \lambda \mu \rangle \langle l L \mu 0 | \lambda \mu \rangle \cdot Y_{m_1}^{l_1}[\vartheta_1, 0] Y_{m_2}^{l_2}[\vartheta_2, \pi] Y_0^L[0, 0] Y_\mu^l[\vartheta_{ab}, 0], \quad (3.3.38)$$

where  $\vartheta_i$  are given by the expression above and  $\vartheta_{ab}$  is the angle between  $r_a$  and  $r_b$ , which is  $\cos \vartheta_{ab} = x$ . The sign term is given by the Clebsch-Gordan symmetry relation

$$\langle l L \mu 0 | \lambda \mu \rangle = (-)^{l+L-\lambda} \langle L l 0 \mu | \lambda \mu \rangle. \quad (3.3.39)$$

The expression above can be further simplified taking in account the symmetries of the spherical harmonics

$$Y_{m_2}^{l_2}[\vartheta_2, \pi] = (-)^{m_2} Y_{m_2}^{l_2}[\vartheta_2, 0] \quad (3.3.40)$$

and in the first Clebsch-Gordan the conservation condition on the magnetic quantum numbers ( $m_1 + m_2 = \mu$ ) reduces the triple summation to a double summation

$$A(x) = \frac{1}{2\lambda + 1} \sum_{\mu m_1} \langle l_1 l_2 m_1 \mu - m_1 | \lambda \mu \rangle (-)^{l+L-\lambda} \langle L l 0 \mu | \lambda \mu \rangle \cdot (-)^{\mu - m_1} Y_{m_1}^{l_1}[\vartheta_1, 0] Y_{\mu - m_1}^{l_2}[\vartheta_2, 0] Y_0^L[0, 0] Y_\mu^l[\vartheta_{ab}, 0]. \quad (3.3.41)$$

We must notice that this expression is slightly different from the one written by Balian-Brezin, because of the different conventions they used. It's interesting to notice that the spherical harmonics

$$Y_l^m[\vartheta, \varphi] = \sqrt{\frac{2l+1}{4\pi} \frac{(l-m)!}{(l+m)!}} P_l^m(\cos \vartheta) e^{im\varphi} \quad (3.3.42)$$

written in the equation (3.3.41) way (q.e. with  $\varphi = 0$ ) have a vanishing phase, so they can be written just as a Legendre polynomial up to a normalization factor.

- Another possible configuration of the vectors is to set everything in the

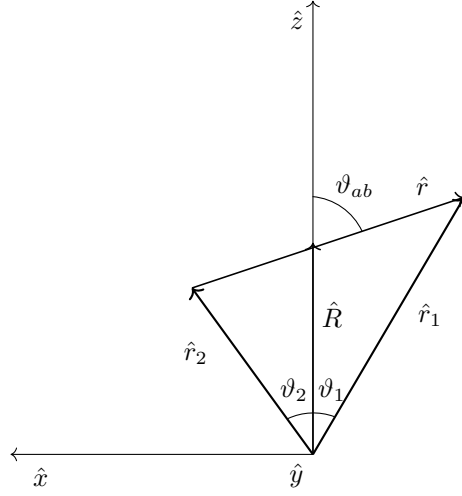


**Figure 3.1:** Configuration of the radial vectors in equation (3.3.41) in the cartesian coordinate system.  $\hat{y}$  is pointing out of the plane.  $\mathbf{R} = r\hat{z}$

plane  $xOy$ . In this case the spherical harmonics are all defined for  $\vartheta = \pi/2$ , and they can be written as

$$Y_{lm_l}\left(\frac{\pi}{2}, \varphi\right) = \Gamma_{lm_l} e^{im_l\varphi} \quad (3.3.43)$$

with

$$\Gamma_m^l = \begin{cases} 0 & \text{if } l - m \text{ is odd} \\ \frac{(-)^{(l+m)/2}}{2^l((l+m)/2)!((l-m)/2)!} \left[ \frac{2l+1}{4\pi} (l+m)!(l-m)! \right]^{1/2} & \text{if } l - m \text{ is even.} \end{cases} \quad (3.3.44)$$

Equation (3.3.30) can then be written as

$$A_{III}(x) = (2\lambda + 1)^{-1} \sum_{\mu} e^{i\mu\varphi_2} \left[ \sum_m \langle lmL\mu - m | \lambda\mu \rangle \Gamma_m^l \Gamma_{\mu-m}^L e^{-im\varphi} \right] \times \\ \times \left[ \sum_{m_\alpha} \langle l_\alpha m_\alpha l_\beta \mu - m_\alpha | \lambda\mu \rangle \Gamma_{m_\alpha}^{l_\alpha} \Gamma_{\mu-m_\alpha}^{l_\beta} e^{im_\alpha(\varphi_1 - \varphi_2)} \right]. \quad (3.3.45)$$

The analytical form of the  $\Gamma$  function implies that every exponential is

real, then

$$A_{III}(x) = (2\lambda + 1)^{-1} \sum_{\mu} \cos(\mu\varphi_2) \left[ \sum_m \langle lmL\mu - m | \lambda\mu \rangle \Gamma_m^l \Gamma_{\mu-m}^L \cos(m\varphi) \right] \times \left[ \sum_{m_\alpha} \langle l_\alpha m_\alpha l_\beta \mu - m_\alpha | \lambda\mu \rangle \Gamma_{m_\alpha}^{l_\alpha} \Gamma_{\mu-m_\alpha}^{l_\beta} \cos(m_\alpha(\varphi_1 - \varphi_2)) \right]. \quad (3.3.46)$$

- Another possibility is the following: first we set  $\hat{r}_1$  along the  $z$ -axis and all the other vectors in the plane  $xOz$ . Then  $\hat{r}_2$  and  $\hat{r}_b$  can be rotated around the  $y$ -axis, in this way  $\hat{r}_2$  is put along the  $z$ -axis

$$A(x) = (2\lambda + 1)^{-1} \sum_{m_1 m_2} \langle l_1 l_2 m_1 0 | \lambda m_1 \rangle \langle l L m 0 | \lambda m \rangle Y_{m_1}^{l_1*}[\hat{r}_{a1}, 0] \sqrt{\frac{2l_2 + 1}{4\pi}} Y_M^L[\hat{r}_b, 0] \sqrt{\frac{2L + 1}{4\pi}} d_{mm_1}^L(\hat{r}_1), \quad (3.3.47)$$

where  $\hat{r}_{a1}$  is the angle between  $\mathbf{r}_a$  and  $\mathbf{r}_1$ ,  $d_{mm'}^l(\beta) = \langle lm | e^{-i\beta J_y} | lm' \rangle = D_{mm'}^l(0, \beta, 0)$  is an element of the orthogonal Wigner's (small) d-matrix and  $J_y$  is the generator of the rotation.

- So far, all the expressions we have seen live in the coordinate space. Finally, we show an expression for the momentum space, due to Kung, Kuo and Ratcliff [22]. They start considering the expression for the vector bracket in the momentum space

$$\langle klKL; \lambda | k_3 l_3 k_4 l_4; \lambda \rangle = 4\pi^2 \delta(w) \vartheta(1 - x^2) A(x), \quad (3.3.48)$$

where  $w = k^2 + \frac{1}{4}K^2 - \frac{1}{2}(k_3^2 + k_4^2)$ ,  $x = (k_3^2 - k^2 - \frac{1}{4}K^2)/kK$ . This is completely analogous to our equation (3.3.24), with the  $\delta(w)$  expressing now an energy conservation. Then we can rewrite equation (3.3.30) for our new vectors system  $k, K, k_1$  and  $k_2$

$$A(x) = (2\lambda + 1)^{-1} \sum_{\mu} [Y_m^l(\hat{k}) \times Y_M^L(\hat{K})]_{\mu}^{\lambda*} [Y_{m_3}^{l_3}(\hat{k}_3) \times Y_{m_4}^{l_4}(\hat{k}_4)]_{\mu}^{\lambda}. \quad (3.3.49)$$

The vector rotation chosen by Kung-Kuo-Ratcliff is the following:  $\hat{k}_3$  is chosen to be along the  $z$ -axis and the vectors  $\hat{k}_3$  and  $\hat{k}_4$  belong to the  $\varphi = 0$  plane.

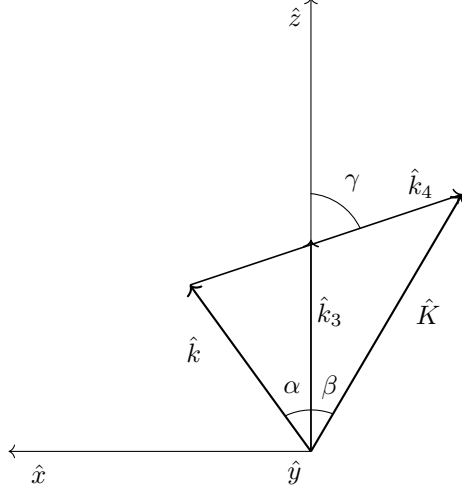


**Figure 3.2:** Configuration of the momentum vectors in the  $\varphi = 0$  plane.  $\hat{y}$  is pointing out of the plane.

Then  $A(x)$  becomes

$$A(x) = \frac{(-)^{l+L+\lambda}}{2\lambda+1} \sum_{\mu M} (-)^{\mu} \langle lLmM|\lambda-\mu\rangle \langle l_3l_40\mu|\lambda\mu\rangle Y_m^l(\alpha, 0) Y_M^L(\beta, 0) Y_0^{l_3}(0, 0) Y_{\mu}^{l_4}(\gamma, 0) \quad (3.3.50)$$

with

$$\alpha = \cos^{-1} \left[ \frac{k_3^2 + k^2 - K^2/4}{2kk_3} \right] \quad (3.3.51)$$

$$\beta = \cos^{-1} \left[ \frac{k_3^2 + K^2/4 - k^2}{kk_3} \right] \quad (3.3.52)$$

$$\gamma = \cos^{-1} \left[ \frac{k_3^2 + k_4^2 - 4k^2}{2k_3k_4} \right]. \quad (3.3.53)$$

We notice that this equation is the same as eq. (3.3.41), with the same phase factors. This was predictable because the Balian and Brezin procedure is general for a 4-vector system, and suggests that all the Wong and Clement calculation is the same in the momentum space.

In the rest of this work, for the numerical implementation of the Wong-Clement coefficients we chose eq. (3.3.41) because it's the most efficient one, having the least number of summations.

### 3.3.2 Three-body Wong-Clement coefficients

The vector and Wong-Clement brackets we have seen are fundamental quantities from which we can build more complicated objects. For example, we can generalize them to find the analogous of the Wong-Clements coefficient in the three-body case. To do this, we start from the completeness relation

$$|(n_1 l_1 n_2 l_2) \lambda_{12} n_3 l_3; \lambda \mu\rangle = \sum_{lL'} \int dr_a dr'_b \langle r_a l r'_b L'; \lambda_{12} | n_1 l_1 n_2 l_2; \lambda_{12} \rangle | (r_a l r'_b L') \lambda_{12} n_3 l_3; \lambda \mu \rangle, \quad (3.3.54)$$

where the right-side ket is given by

$$|(r_a l r'_b L') \lambda_{12} n_3 l_3; \lambda \mu\rangle = \sum_{\mathfrak{L} L l_c} \int dr_b dr_c \langle (lL') \lambda_{12} l_3; \lambda | l(L' l_3) \mathfrak{L}; \lambda \rangle \langle r_b L r_c l_c; \mathfrak{L} | r'_b L' n_3 l_3; \mathfrak{L} \rangle | r_a l(r_b L r_c l_c) \mathfrak{L}; \lambda \mu \rangle, \quad (3.3.55)$$

where the first bracket is an angular coupling coefficient

$$\langle (lL') \lambda_{12} l_3; \lambda | l(L' l_3) \mathfrak{L}; \lambda \rangle = \sqrt{(2\mathfrak{L} + 1)(2\lambda_{12} + 1)} (-)^{l + \lambda_{12} + l_3 + \mathfrak{L}} \begin{Bmatrix} \lambda_{12} & l_3 & \lambda \\ \mathfrak{L} & l & L' \end{Bmatrix}, \quad (3.3.56)$$

while the second has the same structure as equation (3.3.29). The final three-body Wong-Clement coefficient can then be written as

$$\langle r_a l(r_b L r_c l_c) \mathfrak{L}; \lambda \mu | (n_1 l_1 n_2 l_2) \lambda_{12} n_3 l_3; \lambda \mu \rangle = \sum_{lL' \mathfrak{L} L l_c} \int dr_a dr'_b dr_b dr_c \langle r_a l r'_b L'; \lambda_{12} | n_1 l_1 n_2 l_2; \lambda_{12} \rangle \langle (lL') \lambda_{12} l_3; \lambda | l(L' l_3) \mathfrak{L}; \lambda \rangle \langle r_b L r_c l_c; \mathfrak{L} | r'_b L' n_3 l_3; \mathfrak{L} \rangle. \quad (3.3.57)$$



## CHAPTER 4

# GENERALIZED SPHERICAL BASES FOR *AB* *INITIO* CALCULATIONS

Now that we have all the machinery necessary to compute general interaction matrix elements, we focus on the choice of the basis to use for our nuclear structure computations.

### 4.1 Bases in nuclear physics

The harmonic oscillator (HO) basis is a fundamental tool on which the nuclear structure computations of the last decades have been grounded. Its convenience relies on multiple aspects. First, in the case of small nuclei the self-consistent field is well-approximated by the harmonic potential at small distances from the center of the nucleus. Second, decoupling brackets of the center-of-mass and relative motions are well known and easy to compute in this basis. These are the Moshinsky brackets, discussed in detail in **Section 3**.

On the other hand, this basis involves some negative aspects. The HO functions has an oscillating behavior at the boundaries of a selected box and this has several negative consequences: it can constitute a problem for the convergence of nuclear structure calculations and it makes this basis ill-suited for the computation of complex nuclei, like the heavy or the weakly-bounded ones.

It is then clear the importance of making nuclear structure computations with a different basis, to push forward the domain of nuclei which can be studied. An alternative to the HO basis in nuclear structure physics has been recently proposed by Bulgac and Forbes [2], while it was first introduced by [1].

Their suggestion is the use of the Discrete Variable Representation (DVR) basis, which found a wide use in quantum chemistry and is the state of the art in several different fields as chemical physics, theoretical spectroscopy and molecular dynamics.

In nuclear physics, the numerical representation of wave functions requires limiting both ultraviolet (UV) and infrared (IR) scales. DVR bases seem to be particularly suitable for studying these two limits. Also, one can often use smaller basis set than the HO basis getting qualitatively similar results. In the following of this section, we will show for the particular basis that we are going to use for nuclear computations (the Bessel DVR) that less partial waves in the model space are needed to reach the same energy than in the HO case.

## 4.2 Discrete Variable Representation

A deep explanation of the historical context of DVR and FBR (finite basis representation) can be found in [25], and a lot of applications of these two representations are discussed in various articles by Littlejohn and Light [30, 28, 27, 29, 26]. In [2], the authors showed the suitability of this basis for nuclear structure calculations, because it is optimal for the representation of wave functions and allows to study the ultraviolet and infrared convergence property of the nuclei, which is forbidden in the case of the harmonic oscillator, whose wave functions diverge at the boundaries of the considered box.

Following [31], we consider the three-dimensional configuration space for the single-particle  $M = \mathbb{R}^3$ . Then we select the Hilbert space  $\mathcal{H} = L^2(M)$  of the square-integrable wavefunctions on  $M$ . On this space we define a projector  $\hat{P}$  on a subspace  $\mathcal{S} = P\mathcal{H}$ . Let  $\{x_\alpha\}$  be a set of grid points defined in the space  $M$ . Finally we introduce the notation  $\Delta_\alpha(x) = P[\delta(x - x_\alpha)]$  for the projected  $\delta$ -functions concentrated around the grid points. We say that the grid  $\{x_\alpha\}$  defines a DVR set if the set of vectors

$$|\Delta_\alpha\rangle = P|x_\alpha\rangle, \quad (4.2.1)$$

is orthogonal

$$\langle\Delta_\alpha|\Delta_\beta\rangle = N_\alpha\delta_{\alpha\beta}N_\alpha > 0 \quad (4.2.2)$$

and complete in  $\mathcal{S}$ . Then we can define the complete and orthonormalized set of vectors

$$|F_\alpha\rangle = \frac{1}{\sqrt{N_\alpha}}|\Delta_\alpha\rangle, \quad (4.2.3)$$

as the DVR set of the space  $\mathcal{S}$  on the grid  $\{x_\alpha\}$  (actually, also the grid itself defines the DVR set with the projection operator). Eq. (4.2.3) shows that each

state  $|F_\alpha\rangle$  is localized around the grid point  $x_\alpha$ . In this sense, the states  $F$  in the  $\mathcal{S}$ -space are localized around the grid points. The  $\hat{P}$  operator is a projector, so it's idempotent and self-adjoint:  $\hat{P}^\dagger = \hat{P}^2 = \hat{P}$ . We can therefore show that

$$\langle \Delta_\alpha | \Delta_\beta \rangle = \langle x_\alpha | \hat{P}^2 | x_\beta \rangle = \langle x_\alpha | \hat{P} | x_\beta \rangle = \langle x_\alpha | \Delta_\beta \rangle = \Delta_\beta(x_\alpha) = \Delta_\alpha^*(x_\beta) = N_\alpha \delta_{\alpha\beta}, \quad (4.2.4)$$

where we used the following theorem: the scalar product of two  $\delta$ -functions can be obtained by projecting each  $\delta$  function on the grid points of the second  $\delta$  function. As a consequence of this theorem we get the following corollary: the set of  $\Delta$  function is orthogonal if and only if

$$\Delta_\alpha(x_\beta) = N_\alpha \delta_{\alpha\beta}. \quad (4.2.5)$$

Then from eq. (4.2.3)

$$F_\beta(x_\alpha) = \delta_{\alpha\beta} \sqrt{N_\alpha}, \quad (4.2.6)$$

so the each DVR function is non vanishing only in his grid points (which are the grid points with the same index of the function-state  $F$ ). DVR functions then satisfy two properties: orthogonality ( $\langle \Delta_\alpha | \Delta_\beta \rangle = N_\alpha \delta_{\alpha\beta}$  or  $\langle F_\alpha | F_\beta \rangle = \delta_{\alpha\beta}$ ) and interpolation property ( $\Delta_\alpha(x_\beta) = N_\alpha \delta_{\alpha\beta}$ ). Now we use this properties to get two different ways to expand a function which belongs to  $\mathcal{S}$ .

We start considering a vector  $|\varphi\rangle \in \mathcal{S}$ . This state can be expanded as a function of the DVR set

$$|\varphi\rangle = \sum_\alpha |F_\alpha\rangle \langle F_\alpha | \varphi \rangle = \sum_\alpha \frac{1}{N_\alpha} \varphi(x_\alpha) |F_\alpha\rangle, \quad (4.2.7)$$

where we used eq. (4.2.3) to simplify the second equivalence. Then the DVR representation of the state vector  $|\varphi\rangle$ , which is  $\varphi_\alpha^{DVR} = \langle F_\alpha | \varphi \rangle$ , is simply given by the wavefunction evaluated at the grid points. So we can use the two definitions

$$\varphi_\alpha^{DVR} = \langle F_\alpha | \varphi \rangle \quad (4.2.8)$$

$$\varphi_\alpha^{DVR} = \frac{1}{\sqrt{N_\alpha}} \varphi(x_\alpha), \quad (4.2.9)$$

which are respectively the 'scalar product definition' and the 'grid definition' of the DVR function. If  $|\varphi\rangle \notin \mathcal{S}$ , these two expressions are different, while their projections on  $\mathcal{S}$  are still the same. We can then define two possible approximation of the state vector  $|\varphi\rangle$ , the first from the projection on  $\mathcal{S}$

$$|\varphi\rangle \simeq |\varphi^S\rangle = P |\varphi\rangle = \sum_\alpha |F_\alpha\rangle \langle F_\alpha | \varphi \rangle \quad (4.2.10)$$

and the second one from the DVR equation

$$|\varphi\rangle \simeq |\varphi^{DVR}\rangle = \sum_{\alpha} \frac{1}{\sqrt{N_{\alpha}}} \varphi(x_{\alpha}) |F_{\alpha}\rangle. \quad (4.2.11)$$

We have then approximated the state  $|\varphi\rangle$  with two different ways of writing their projection on the  $\mathcal{S}$  space. Eq. (4.2.11) defines the approximate Discrete Variable Representation of the state vector  $\varphi_{\alpha}^{DVR} = \langle F_{\alpha} | \varphi^{DVR} \rangle = \varphi(x_{\alpha}) N_{\alpha}^{-1/2}$ . We can as well express an approximation of the scalar product in the  $\mathcal{S}$  space. First, we consider two state vectors  $|\varphi\rangle, |\psi\rangle \in \mathcal{S}$

$$\langle \varphi | \psi \rangle = \sum_{\alpha} \langle \psi | F_{\alpha} \rangle \langle F_{\alpha} | \varphi \rangle = \sum_{\alpha} \frac{1}{N_{\alpha}} \psi^{*}(x_{\alpha}) \varphi(x_{\alpha}). \quad (4.2.12)$$

So the DVR set introduces an exact quadrature rule for the scalar product

$$\langle \varphi | \psi \rangle = \sum_{\alpha} \omega_{\alpha} \psi^{*}(x_{\alpha}) \varphi(x_{\alpha}) \quad \text{with} \quad \omega_{\alpha} = N_{\alpha}^{-1} \quad (4.2.13)$$

which, in the case of vectors  $|\varphi\rangle, |\psi\rangle \notin \mathcal{S}$ , is an approximation of the scalar product

$$\langle \varphi | \psi \rangle \simeq \langle \varphi^{DVR} | \psi^{DVR} \rangle. \quad (4.2.14)$$

### Finite Basis Representation (FBR)

Now we consider a complete orthonormal set  $\{|\psi_n\rangle\}$  in  $\mathcal{S}$ . This can be used to obtain the so called Finite Basis Representation

$$|\varphi\rangle = \sum_n |\psi_n\rangle \langle \psi_n | \varphi \rangle, \quad (4.2.15)$$

where we can identify  $\langle \psi_n | \varphi \rangle = \varphi_n^{FBR}$  as the FBR state vector in the  $\mathcal{S}$  space.

It can be noticed that a unitary transformation exists such that

$$|F_{\alpha}\rangle = \sum_n |\psi_n\rangle U_{n\alpha}. \quad (4.2.16)$$

Acting on this equation with a  $\langle \varphi |$  bra we obtain

$$\langle \varphi | F_{\alpha} \rangle = \sum_n \langle \varphi | \psi_n \rangle U_{n\alpha} \quad (4.2.17)$$

$$\varphi^{DVR} = \sum_n (U^{\dagger})_{\alpha n} \psi_n^{FBR}. \quad (4.2.18)$$

This unitary matrix can then be used to transform between the DVR and FBR

representations. Noticing that we can expand the bracket  $\langle \varphi | F_\alpha \rangle$  as

$$\langle \varphi | F_\alpha \rangle = \sum_n \langle \varphi | \psi_n \rangle \langle \psi_n | F_\alpha \rangle \quad (4.2.19)$$

and comparing with eq. (4.2.17) we obtain

$$U_{n\alpha} = \langle \psi_n | F_\alpha \rangle = \sqrt{\omega_\alpha} \psi_n^*(x_\alpha), \quad (4.2.20)$$

where  $\omega_\alpha$  is the quadrature weight. We can represent operator expectation values as

$$\langle F_\alpha | A | F_\beta \rangle = \sum_{nm} \langle F_\alpha | \psi_n \rangle \langle \psi_n | A | \psi_m \rangle \langle \psi_m | F_\beta \rangle, \quad (4.2.21)$$

which can be vectorized with the help of the unitary matrix above introduced

$$A^{DVR} = U^\dagger A^{FBR} U. \quad (4.2.22)$$

Local operators can instead be approximated as

$$\langle F_\alpha | A | F_\beta \rangle = A(x_\alpha) \delta_{\alpha\beta}. \quad (4.2.23)$$

This equation is exact in the  $\mathcal{S}$ -space.

The standard procedure to determine a DVR is: first one uses (4.2.23) for operators which are local in our coordinate system and, starting from an appropriate FBR for non-local operators, then an approximate discrete variable representation can be obtained using (4.2.22). If the FB set diagonalizes the operator  $\hat{A}$

$$(\hat{A}^{DVR})_{\alpha\beta} = \sum_n \sqrt{\omega_\alpha \omega_\beta} \psi_n(x_\alpha) \psi_n^*(x_\beta) a_n. \quad (4.2.24)$$

More in general

$$(f(\hat{A})^{DVR})_{\alpha\beta} = \sum_n \sqrt{\omega_\alpha \omega_\beta} \psi_n(x_\alpha) \psi_n^*(x_\beta) f(a_n). \quad (4.2.25)$$

### 4.2.1 Bessel DVR

In this section we focus on the Bessel discrete variable representation basis, that we will use for our nuclear physics application. The primary reference for this section is [32], in which the most important relations for the DVR Bessel basis are derived.

The DVR basis based on Bessel function is particularly suitable for radial problems. In fact, Bessel functions are eigenfunctions of the radial Schrödinger equation for the free-particle in the spherical box. These functions satisfy the

orthonormality condition and the interpolation property we've seen in the previous section.

We will mainly follow [32] where these functions are derived, while an independent derivation has been obtained by Lemoine [33] and consists in applying a discretized Hankel transform on a Bessel FBR basis to obtain the Bessel DVR basis.

We start from a  $d$ -dimensional problem, considering the free-particle in an external potential  $V(r)$ , with total wavefunction  $\Psi(x_1, \dots, x_d) = \psi(r)Y_\lambda(\Omega)$ . The radial Schrödinger equation is given by

$$\frac{1}{r^{d-1}} \frac{d}{dr} \left( r^{d-1} \frac{d\psi}{dr} \right) - \frac{\lambda(\lambda + d - 2)}{r^2} \psi + \frac{2m}{\hbar^2} [E - V(r)] \psi = 0 \quad (4.2.26)$$

normalized according to  $\int_0^\infty r^{d-1} |\psi(r)|^2 dr$ . In the following we'll use the generalized  $d$ -dimensional wave function  $\varphi(r) = r^{(d-1)/2} \psi(r)$ , which satisfies the equation

$$\frac{d^2 \varphi}{dr^2} - \frac{\nu^2 - 1/4}{r^2} \varphi + \frac{2m}{\hbar^2} [E - V(r)] \varphi = 0, \quad (4.2.27)$$

where we have defined the integer/semi-integer index  $\nu = \lambda + d/2 - 1$  and the radial function can be written with the Dirac notation  $\langle r | \varphi \rangle = \varphi(r)$ . For the free-particle with energy  $E = \hbar^2 k^2 / 2m$ , the radial wave function is a Bessel function

$$\varphi_k(r) = \langle r | k\nu \rangle = \sqrt{kr} J_\nu(kr). \quad (4.2.28)$$

This defines the state  $|k\nu\rangle$ , normalized according to

$$\langle k\nu | k'\nu \rangle = \int_0^{+\infty} dr \langle k\nu | r \rangle \langle r | k'\nu \rangle = \delta(k - k') \quad (4.2.29)$$

For an odd number of dimensions, as the 3-dimensional case, we can introduce the functions

$$j_n(r) = \sqrt{\frac{\pi}{2r}} J_\nu(r), \quad (4.2.30)$$

where  $\nu = l + 1/2$ . Here the notation  $J_\nu(r)$  represents the Bessel function of the first kind, while  $j_l(r)$  represents the spherical Bessel function.

### Properties of the Bessel functions

The Bessel function of the first kind is defined in terms of the  $\Gamma$  function

$$J_\nu(r) = \left( \frac{r}{2} \right)^\nu \sum_{n=0}^{\infty} \frac{(-1)^n \left( \frac{r}{2} \right)^{2n}}{n! \Gamma(\nu + n + 1)}. \quad (4.2.31)$$

These functions satisfy the two relations

$$\int_0^R dr \frac{2r}{R^2} \frac{J_\nu(kr)J_\nu(k'r)}{|J'_\nu(kR)J'_\nu(k'R)|} = \delta(k - k') \quad \text{orthonormality relation} \quad (4.2.32)$$

$$\sum_{\alpha=0}^{\infty} \frac{2\sqrt{rr'}}{R^2} \frac{J_\nu(k_\alpha r)J_\nu(k_\alpha r')}{J'_\nu(k_\alpha R)^2} = \delta(r - r') \quad \text{completeness relation} \quad (4.2.33)$$

as well as the recurrence relation

$$J_{\nu-1}(r) + J_{\nu+1}(r) = \frac{2\nu}{r} J_\nu(r). \quad (4.2.34)$$

Finally, the derivative of the Bessel function can be shown to be

$$\frac{d}{dr}[J_\nu(r)] = \frac{1}{2}[J_{\nu-1}(r) + J_{\nu+1}(r)]. \quad (4.2.35)$$

We can define the spherical Bessel functions through the Rayleigh formula

$$j_l(r) = r^l \left( -\frac{1}{r} \frac{d}{dr} \right)^l \frac{\sin r}{r}. \quad (4.2.36)$$

The recurrence relation is then

$$j_{l-1}(r) + j_{l+1}(r) = \frac{2l+1}{r} j_l(r). \quad (4.2.37)$$

For the derivatives we can use

$$j_{l-1}(r) + j_{l+1}(r) = \frac{1}{2n+1} [n j_{l-1}(r) - (l+1) j_{l+1}(r)] = \quad (4.2.38)$$

$$= j_{l-1}(r) - \frac{l+1}{r} j_l(r) = \quad (4.2.39)$$

$$= \frac{l}{r} j_l(r) - j_{l+1}(r) \quad (4.2.40)$$

In an infinite box, the orthonormality relation of the Bessel functions becomes

$$\int_0^{+\infty} dr r^2 j_l(k_\alpha r) j_l(k_\beta r) = \frac{\pi}{2k^2} \delta(k_\alpha - k_\beta). \quad (4.2.41)$$

Having completed this overview on the properties of the Bessel functions, we can resume our path to the Bessel DVR basis. First of all, these functions are defined on a radial half-line, so the manifold  $M$  is restricted to the space  $[0, +\infty)$ . As already seen, we consider the Hilbert space  $\mathbb{H}$  of wavefunctions defined on  $M$ , and  $\mathcal{S}$  a subspace on  $\mathcal{H}$  spanned by the considered basis. We define a projector operator  $\hat{P}$  on  $\mathcal{S}$  and the set of grid points  $\{x_n\}$  on  $M$ . Then the projector  $\hat{P}$  and the grid points define a DVR if the orthogonality relation

$\langle \Delta_n | \Delta_m \rangle = N_n \delta_{nm}$  with  $|\Delta_n\rangle = P|x_n\rangle$ . For the theorem showed in eq. (4.2.4), the  $\delta$  functions vanish at each other's points and they are non-vanishing only at their own points.

We start defining a projection operator and a set of grid points also for the Bessel basis, taking a cutoff in the momentum space. Then we'll check that the DVR conditions are satisfied, which is, they must satisfy the usual theorem (4.2.4). We start guessing the analytical form of the projection operator

$$P = \int_0^K dk |k\nu\rangle \langle k\nu|, \quad (4.2.42)$$

which selects all the free-particle states with energy  $E \leq E_0 = \hbar^2 K^2 / 2m$ . For the grid points we need to do a second guess, which consists in choosing the positive zeroes  $z_{\nu n}$  of the Bessel function as grid points at the limit of the box in the momentum space. The grid points are then  $r_{\nu n} = z_{\nu n} / K$ .

First of all we need the following identity

$$\int_0^R r dr J_\nu(kr) J_\nu(k'r) = \frac{R}{k^2 - k'^2} [k' J_\nu(kR) J'_\nu(k'R) - k J'_\nu(kR) J_\nu(k'R)], \quad (4.2.43)$$

that in the limit  $k' \rightarrow k$  becomes

$$\int_0^R r dr J_\nu(kr)^2 = \frac{1}{2k^2} [k^2 R^2 J'_\nu(kR)^2 + (k^2 R^2 - \nu^2) J_\nu(kR)^2]. \quad (4.2.44)$$

Now we can calculate the expectation value of the projection operator, taking eq. (4.2.43) and swapping  $r$  and  $k$

$$\begin{aligned} \langle r | P | r' \rangle &= \int_0^K dk \langle r | k\nu \rangle \langle k\nu | r' \rangle = \sqrt{rr'} \int_0^K dk k J_\nu(kr) J_\nu(kr') = \\ &= \frac{K \sqrt{rr'}}{r^2 - r'^2} [r' J_\nu(Kr) J'_\nu(Kr') - r J_\nu(Kr') J'_\nu(Kr)]. \end{aligned} \quad (4.2.45)$$

The discretization of this equation gives the known Darboux-Cristoffel formula

$$\sum_{k=0}^n \varphi_k(x) \varphi_k(y) = \frac{k_n}{k_{n+1}} \left[ \frac{\varphi_n(y) \varphi_{n+1}(x) - \varphi_n(x) \varphi_{n+1}(y)}{x - y} \right]. \quad (4.2.46)$$

Now we select  $r'$  as the grid points  $r_{\nu n}$  and write the projected  $\delta$  functions

$$\Delta_{\nu n}(r) = \langle r | P | r_{\nu n} \rangle = \frac{\sqrt{r z_{\nu n}^3 K^3}}{K^2 r^2 - z_{\nu n}^2} J'_\nu(z_{\nu n}) J_\nu(Kr). \quad (4.2.47)$$

So these are orthogonal Bessel DVR functions. We just need to determine the

normalization

$$N_{\nu n} = \langle \Delta_{\nu n} | \Delta_{\nu n} \rangle = \Delta_{\nu n}(r_{\nu n}) = \frac{K z_{\nu n} J'_{\nu}(z_{\nu n})^2}{2} \quad (4.2.48)$$

and the normalized Bessel DVR function is given by

$$F_{\nu n}(r) = \frac{J'_{\nu}(z_{\nu n})}{|J'_{\nu}(z_{\nu n})|} \frac{K z_{\nu n} \sqrt{2r}}{K^2 r^2 - z_{\nu n}^2} J_{\nu}(Kr) = (-)^{n+1} \frac{K z_{\nu n} \sqrt{2r}}{K^2 r^2 - z_{\nu n}^2} J_{\nu}(Kr), \quad (4.2.49)$$

where  $\frac{J'_{\nu}(z_{\nu n})}{|J'_{\nu}(z_{\nu n})|} = \text{sign}(J'_{\nu}(z_{\nu n})) = (-)^{n+1}$ .

### Dirichlet BC

Now we can write the Bessel DVR functions in the case in which we want to have a cutoff in the coordinate space. The eigenfunctions of the free-particle in a spherical box with radius  $R_{box}$  are characterized by the radial eigenfunction  $\varphi_{\nu n}(r) = N_n \sqrt{k_{\nu n} r} J_{\nu}(k_{\nu n} r)$ . Applying Dirichlet boundary condition, we impose that the function vanishes outside the box:  $\varphi_{\nu n}(R_{box}) = 0$ , which leads to  $k_{\nu n} = z_{\nu n}/R_{box}$ . From eq. (4.2.43) we obtain

$$\varphi_{\nu n}(r) = \frac{\sqrt{2r}}{R_{box} |J'_{\nu}(z_{\nu n})|} J_{\nu}(z_{\nu n} r / R_{box}), \quad (4.2.50)$$

which is the normalized wavefunction. Now we can move to the momentum space by substituting  $r$  with  $k$  and swapping  $R_{box}$  with  $K$

$$\hat{\varphi}_{\nu n}(k) = \frac{\sqrt{2k}}{K |J'_{\nu}(z_{\nu n})|} J_{\nu}(z_{\nu n} k / K). \quad (4.2.51)$$

This function needs to be multiplied by a spherical harmonic in the  $k$  space and the result can be transformed again in the coordinate space with a Fourier transform. For spherically symmetric problems, the  $d$ -dimensional Fourier transform is equivalent to the Hankel transform of the radial function

$$\begin{aligned} \varphi_{\nu n}(r) &= \int_0^{\infty} dk \sqrt{kr} J_{\nu}(kr) \hat{\varphi}_{\nu n}(k) = \frac{\sqrt{2r}}{K |J'_{\nu}(z_{\nu n})|} \int_0^K dk k J_{\nu}(kr) J_{\nu}(kr_{\nu n}) = \\ &= \frac{\sqrt{2r}}{K |J'_{\nu}(z_{\nu n})|} \frac{K}{r^2 - r_{\nu n}^2} [r_{\nu n} J_{\nu}(rK) J'_{\nu}(r_{\nu n}K) - r J'_{\nu}(rK) J_{\nu}(r_{\nu n}K)] = \end{aligned}$$

Now we use  $r_{\nu n} = z_{\nu n}/K$  e  $\varphi_{\nu n}(k) = N_n \sqrt{kr_{\nu n}} J_{\nu}(r_{\nu n}k) = 0 \implies J_{\nu}(r_{\nu n}k) = 0$

$$\begin{aligned}
 &= \frac{\sqrt{2r}}{K|J'_{\nu}(z_{\nu n})|} \frac{K^3}{K^2r^2 - z_{\nu n}^2} \frac{z_{\nu n}}{K} J_{\nu}(rK) J'_{\nu}(z_{\nu n}) = \\
 &= \frac{\sqrt{2r}}{K|J'_{\nu}(z_{\nu n})|} \frac{K^3}{K^2r^2 - z_{\nu n}^2} z_{\nu n} J_{\nu}(rK) J'_{\nu}(z_{\nu n}) = \quad (4.2.52) \\
 &= (-1)^{n+1} \frac{K z_{\nu n} \sqrt{2r}}{K^2r^2 - z_{\nu n}^2} J_{\nu}(rK) = F_{\nu n}(r).
 \end{aligned}$$

The result is then  $\varphi_{\nu n}(r) = F_{\nu n}(r)$ , so the Fourier transform of the free-particle in the box in the  $k$ -space are complete in the space of the wavefunctions in the box. We have then proved that the Bessel DVR are complete in this space.  $\varphi_{\nu n}(R_{box}) = 0$ , so the Bessel DVR eigenfunctions satisfy the Dirichlet boundary condition  $F_{\nu n}(R_{box}) = 0$ . We can then use as a definition of the Bessel DVR the eigenfunctions of the particle in the box

$$F_{\nu n}(r) = \frac{\sqrt{2r}}{R_{box}|J'_{\nu}(z_{\nu n})|} J_{\nu}(z_{\nu n}r/R_{box}). \quad (4.2.53)$$

Some of these functions are represented in **Figure 4.1**.

### Neumann BC

In this section we specify the case  $d = 3$ . We start imposing the in  $\mathbf{r} \cdot \nabla \psi = 0$  in  $r = R_{box}$ . In general, the radial derivative of  $\varphi(r)$  is  $d\varphi(r)/dr = [(d - 1)/2]\varphi(r)/r$ , which in the case of  $d = 3$  becomes

$$\frac{d\varphi(r)}{dr} = \frac{\varphi(r)}{r} \quad (4.2.54)$$

in  $r = R_{box}$ . Proceeding in analogy of the Dirichlet calculation, we calculate the normalization of the wavefunction. In this case we get

$$\varphi'(r) = \frac{\sqrt{k}}{s\sqrt{R_{box}}} J_{\nu}(kR_{box}) + \sqrt{kR_{box}} J'_{\nu}(kr) = \frac{\sqrt{kR_{box}} J_{\nu}(kR_{box})}{\sqrt{R_{box}}} \quad (4.2.55)$$

$$J_{\nu}(kR_{box}) = 2R_{box} J'_{\nu}(kR_{box}) = 0 \quad (4.2.56)$$

Eq. (4.2.44) brings the normalization coefficient

$$\int_0^{R_{box}} dr r J_{\nu}(kr)^2 = \left( \frac{1}{8} + \frac{R_{box}^2}{2} - \frac{\nu^2}{2k^2} \right) J_{\nu}(kR_{box})^2. \quad (4.2.57)$$

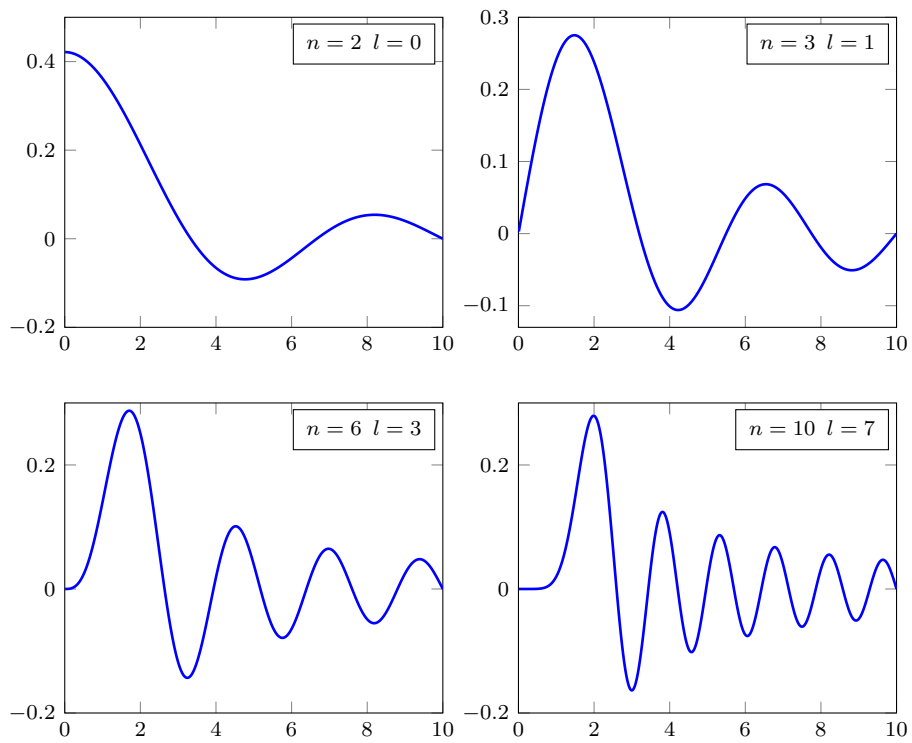


**Figure 4.1:** Plot of the Bessel DVR functions  $F_{nl}(r)$  for  $R_{box} = 10$  and various values of  $n$  and  $l$

The radial eigenfunction is then

$$\varphi(r) = \frac{\sqrt{r}}{\sqrt{\frac{1}{8} + \frac{R_{box}^2}{2} - \frac{\nu^2}{2k^2}}} \frac{J_\nu(kr)}{|J_\nu(kR_{box})|} = \frac{\sqrt{r}}{\sqrt{\frac{1}{8} + \frac{R_{box}^2}{2} - \frac{R_{box}^2 \nu^2}{2z_{\nu n}^2}}} \frac{J_\nu(z_{\nu n}r/R_{box})}{|J_\nu(z_{\nu n})|}. \quad (4.2.58)$$

Swapping  $r \rightarrow k$

$$\hat{\varphi}(k) = \frac{\sqrt{k}}{\sqrt{\frac{1}{8} + \frac{K^2}{2} - \frac{K^2 \nu^2}{2z_{\nu n}^2}}} \frac{J_\nu(z_{\nu n}k/K)}{|J_\nu(z_{\nu n})|}. \quad (4.2.59)$$

Now we can apply the Hankel transform

$$\begin{aligned} \varphi(r) &= i^\lambda \int_0^K dk \sqrt{kr} J_\nu(kr) \hat{\varphi}(k) = \\ &= \frac{i^\lambda \sqrt{r}}{\sqrt{\frac{1}{8} + \frac{K^2}{2} - \frac{K^2 \nu^2}{2z_{\nu n}^2} |J_\nu(z_{\nu n})|}} \int_0^K dk k J_\nu(kr) J_\nu(z_{\nu n}k/K). \end{aligned} \quad (4.2.60)$$

The following identity can be easily verified

$$\begin{aligned} \int_0^K dk k J_\nu(kr) J_\nu(z_{\nu n}k/K) &= \\ &= \frac{K^2}{K^2 r^2 - z_{\nu n}^2} (z_{\nu n} J_{\nu-1}(z_{\nu n}) J_\nu(Kr) - Kr J_{\nu-1}(Kr) J_\nu(z_{\nu n})) = \end{aligned} \quad (4.2.61)$$

Isolating eq. (4.2.49)

$$\begin{aligned} &= \frac{(-1)^{n+1} K z_{\nu n} \sqrt{2r}}{K^2 r^2 - z_{\nu n}^2} \frac{J_\nu(Kr) (-1)^{n+1} K}{2\sqrt{r}} \left( J_{\nu-1}(z_{\nu n}) - \frac{Kr}{z_{\nu n}} \frac{J_{\nu-1}(Kr) J_\nu(z_{\nu n})}{J_\nu(Kr)} \right) = \\ &= F_\nu(r) (-1)^{n+1} \frac{K}{2\sqrt{r}} \left( J_{\nu-1}(z_{\nu n}) - \frac{Kr}{z_{\nu n}} \frac{J_{\nu-1}(Kr) J_\nu(z_{\nu n})}{J_\nu(Kr)} \right). \end{aligned} \quad (4.2.62)$$

Then we have

$$\varphi(r) = \frac{i^\lambda}{\sqrt{\frac{1}{8} + \frac{K^2}{2} - \frac{K^2 \nu^2}{2z_{\nu n}^2} |J_\nu(z_{\nu n})|}} F_\nu(r) (-1)^{n+1} \frac{K}{2} \left( J_{\nu-1}(z_{\nu n}) - \frac{Kr}{z_{\nu n}} \frac{J_{\nu-1}(Kr) J_\nu(z_{\nu n})}{J_\nu(Kr)} \right). \quad (4.2.63)$$

Using eq. (4.2.58) we obtain the Bessel DVR function for Neumann boundary condition in  $d = 3$ .

### 4.2.2 Kinetic matrix elements for Bessel DVR functions

We start considering the total wavefunction

$$F(r, \vartheta, \varphi, \sigma, \tau) = F_{nl}(r)Y_{lm}(\vartheta, \varphi)\chi(s)\chi(\tau) \quad (4.2.64)$$

For the radial function we use the 3-dimensional Bessel DVR function with Dirichlet boundary conditions.

$$F_{nl}(r) = 2\sqrt{\frac{z_{\nu n}}{\pi R_{box}}} \frac{1}{R_{box}|J'_{\nu}(z_{\nu n})|} j_l(k_{\nu n}r) = \sqrt{\frac{2}{r}} \frac{1}{R|J'_{\nu}(z_{\nu n})|} J_{\nu}(k_{\nu n}r). \quad (4.2.65)$$

The kinetic matrix elements are given by the expectation values

$$t_{\alpha\beta} = \left\langle \alpha \left| -\frac{\hbar^2 \nabla^2}{2m} \right| \beta \right\rangle = \delta_{q_{\alpha}q_{\beta}} \delta_{j_{\alpha}j_{\beta}} \delta_{m_{\alpha}m_{\beta}} \delta_{l_{\alpha}l_{\beta}} t_{n_{\alpha}n_{\beta}}^{l=l_{\alpha}=l_{\beta}} \quad (4.2.66)$$

$$t_{n_{\alpha}n_{\beta}}^l = -\frac{\hbar^2}{2m} \int_0^{R_{box}} dr r^2 F_{n_{\alpha}l}(r) \left[ \frac{d^2}{dr^2} + \frac{2}{r} \frac{d}{dr} - \frac{l(l+1)}{r^2} \right] F_{n_{\beta}l}(r) \quad (4.2.67)$$

Where  $q$  is the charge of the single particle. Here the laplacian can be simplified taking into account that the spherical Bessel function is solution of the Bessel equation

$$\left[ \frac{d^2}{dr^2} + \frac{2}{r} \frac{d}{dr} - \frac{l(l+1)}{r^2} \right] j_l(kr) = -k^2 j_l(kr). \quad (4.2.68)$$

We could have also used the Helmholtz equation before separating the radial and the angular part, getting the same result

$$\nabla^2 [j_l(kr)Y_{lm}(\vartheta, \varphi)] = -k^2 [j_l(kr)Y_{lm}(\vartheta, \varphi)] \quad (4.2.69)$$

In general, the solutions of the Bessel and the Helmholtz equations is a linear combination of spherical Bessel functions of the first and of the second kind. Here we just need the first ones.

$$t_{n_{\alpha}n_{\beta}}^l = \frac{\hbar^2}{2m} k_{\nu n_{\beta}}^2 \int_0^{R_{box}} dr r^2 F_{n_{\alpha}l}(r) F_{n_{\beta}l}(r) = \frac{\hbar^2}{2m} k_{\nu n_{\beta}}^2 \delta_{n_{\alpha}n_{\beta}}. \quad (4.2.70)$$

The last integral is the orthogonality condition of the Bessel DVR functions with Dirichlet conditions and can be proven in the following way

$$\int_0^{R_{box}} dr r^2 F_{n_{\alpha}l}(r) F_{n_{\beta}l}(r) = \int_0^{R_{box}} \frac{2r}{R^2} \frac{J_{\nu}(k_{\nu n_{\alpha}}r) J_{\nu}(k_{\nu n_{\beta}}r)}{J'_{\nu}(k_{\nu n_{\alpha}}r) J'_{\nu}(k_{\nu n_{\beta}}r)} = \delta_{n_{\alpha}n_{\beta}}. \quad (4.2.71)$$

### 4.2.3 The Bessel DVR model space

In order to use the Bessel DVR functions for nuclear structure calculations, we need to study the distribution of the associated energy eigenvalues. This allows us to decide how to cut the model space, that is, which partial waves we want to include. The free-particle energy can be written as a function of the momenta, which, in the case of the Bessel DVR basis, are connected to the nodes of the Bessel functions through the radius  $R_{box}$  of the box ( $k_{nl} = z_{nl}/R_{box}$ )

$$\varepsilon_{nl} = \frac{\hbar^2 k_{nl}^2}{2m} = \frac{\hbar^2 z_{nl}^2}{2m R_{box}^2}, \quad (4.2.72)$$

where  $z_{nl}$  are the zeros of the Bessel functions as usual. We represent in **Figure 4.2** the distribution of these levels.

As we can see, for fixed  $l = \bar{l}$ , when  $n$  grows the zeroes of the Bessel functions with  $l = \bar{l} + 2$  and  $n - 1$  tend to align to the same zero:  $z_{n,\bar{l}} \rightarrow z_{n-1,\bar{l}+2}$  for  $n \rightarrow +\infty$ . This is represented in **Figure 4.3**. The energy levels (**Figure 4.2**) have the same behaviour, as they are proportional to the Bessel zeroes.

The reason of this behavior emerges from the definition of spherical Bessel functions

$$j_l(r) = (-r)^l \left( \frac{1}{r} \frac{d}{dr} \right)^l \frac{\sin r}{r}, \quad (4.2.73)$$

so for even  $l$ , the leading term is proportional to  $\sin(r)$  and the zeroes of the Bessel functions tend to be multiples of  $\pi$ , while for odd  $l$  the leading term is  $\cos(r)$  and the zeroes tend to be multiples of  $\pi/2$ . This can be more easily seen if we take a look at the first Bessel functions

$$j_0(r) = \frac{\sin r}{r} \quad (4.2.74)$$

$$j_1(r) = \frac{\sin r}{r^2} - \frac{\cos r}{r} \quad (4.2.75)$$

$$j_2(r) = \left( \frac{3}{r^2} - 1 \right) \frac{\sin r}{r} - \frac{3 \cos r}{r^2} \quad (4.2.76)$$

$$j_3(r) = \left( \frac{15}{r^3} - \frac{6}{r} \right) \frac{\sin r}{r} - \left( \frac{15}{r^2} - 1 \right) \frac{\cos r}{r}, \quad (4.2.77)$$

in which is clearly visible that in the case of even  $l$  the dominant term is proportional to  $\sin r$ , while for odd  $l$  the dominant term is  $\cos r$ . Another characteristic behavior of the Bessel DVR model space is that the spacing between the energy levels increases with  $n$ . This is very different from the harmonic oscillator model space, where the spacing between the energy levels is constant and is always  $\Delta\varepsilon = 2\hbar\Omega$ , where  $\Omega$  is the oscillator frequency. A typical plot of the single-particle levels in the nuclear shell model is showed in **Figure 4.5**, where

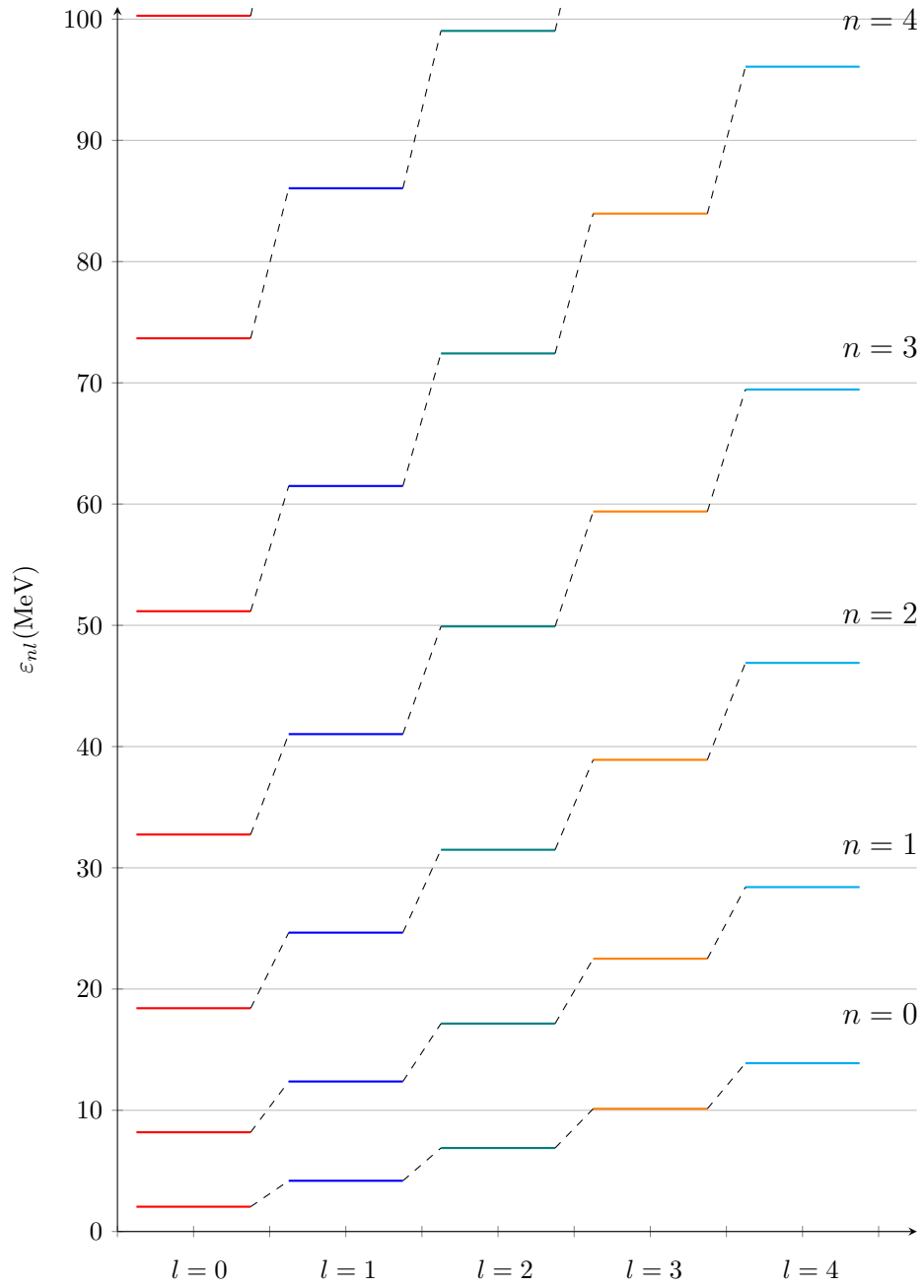
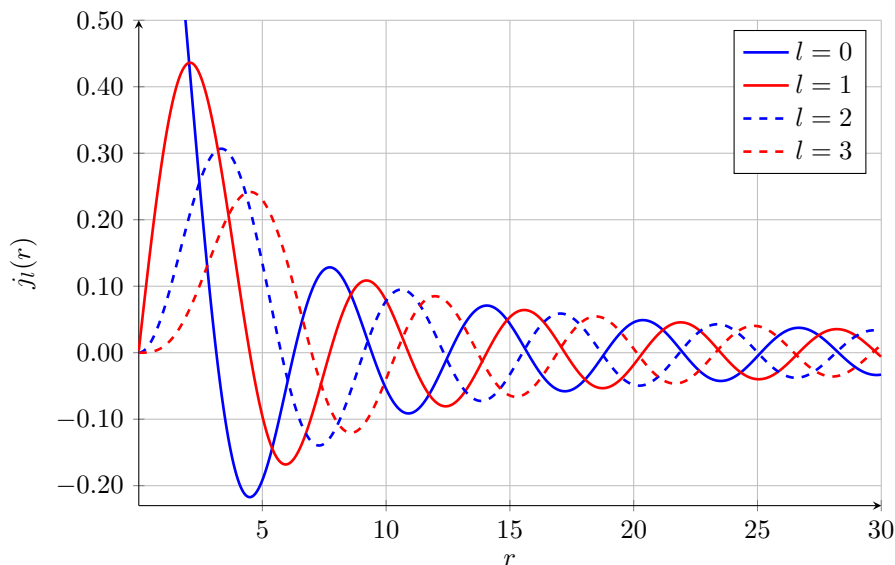


Figure 4.2: Energy levels for the Bessel DVR basis ( $R_{box} = 10$  fm)



**Figure 4.3:** Spherical Bessel functions. In blue the ones with even  $l$ , in red the ones with odd  $l$

the effect of the spin-orbit is also outlined.

After this discussion on the distribution of the energy levels, we need to decide a criterion to build the model space. To do this, we consider the **Figure 4.4**, which represents the energy levels as a function of  $N_{max} = 2n + l$ , which is the usual principal quantum number for the harmonic oscillator. This is the quantum number used to cut the model space for the harmonic oscillator case: first one chooses the  $N_{max}$  they want to use, than only the partial waves with quantum numbers with  $n$  and  $l$  such that  $2n + l \leq N_{max}$  are selected.

We create the corresponding DVR model space by including the energy levels with quantum numbers  $n, l$  such that  $2n + l < l_{max} + 1$  and  $z_{nl} < z_{0, l_{max} + 1}$ . The second condition corresponds to a cutoff on the energy  $\varepsilon_{nl} = \frac{\hbar^2 k_{nl}^2}{2m}$ .

For a given value of  $l_{max} = N_{max}$  the Bessel DVR model space includes less orbitals (we are considering  $N_{max} = l_{max}$  when comparing the HO and Bessel model space), because the spacing between the levels increases with the energy, so we need less levels to reach the same energy than in the harmonic oscillator case.

Finally, we can give a quick estimate useful to approximately compare the two different bases with their length parameters, which are  $b_{HO} = \sqrt{\frac{\hbar}{m\Omega}}$  (the oscillator length) in the case of the harmonic oscillator and  $R_{box}$  in the case of the Bessel DVR. We do this by calculating the spacing of the energy levels in the two bases. In the Bessel DVR case, we take the spacing between the first

nodes of the  $s$  orbitals

$$\Delta\varepsilon = \varepsilon_{1s_{1/2}} - \varepsilon_{0s_{1/2}} = \frac{\hbar^2\pi^2}{2mR_{box}^2}(2^2 - 1^2) = \frac{\hbar^2\pi^2}{2mR_{box}^2}3 \quad (4.2.78)$$

$$\Delta'\varepsilon = \varepsilon_{2s_{1/2}} - \varepsilon_{1s_{1/2}} = \frac{\hbar^2\pi^2}{2mR_{box}^2}(3^2 - 2^2) = \frac{\hbar^2\pi^2}{2mR_{box}^2}5. \quad (4.2.79)$$

A mean of this two values gives

$$\Delta\varepsilon = 2\frac{\hbar^2\pi^2}{mR_{box}^2}. \quad (4.2.80)$$

This value can be compared with the spacing between two consecutive energy levels in the harmonic oscillator case, which is  $\Delta\varepsilon = 2\hbar\Omega$ . Comparing these results we obtain

$$R = \pi b_{HO}, \quad (4.2.81)$$

which is an approximated formula that we're going to use to compare results in the two different bases.

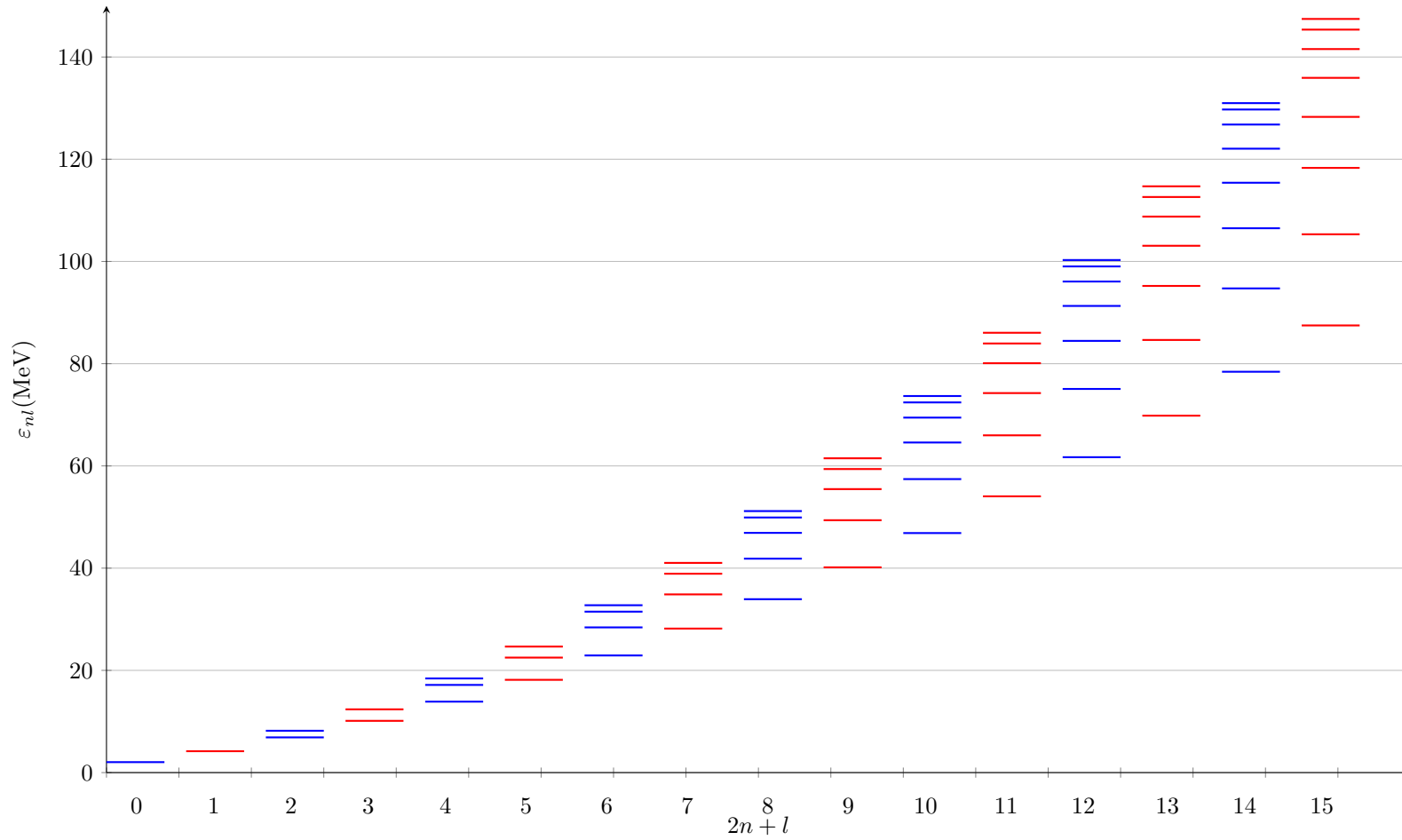


Figure 4.4: Energy of the partial waves as a function of  $2n + l$  ( $R_{box} = 10$  fm)

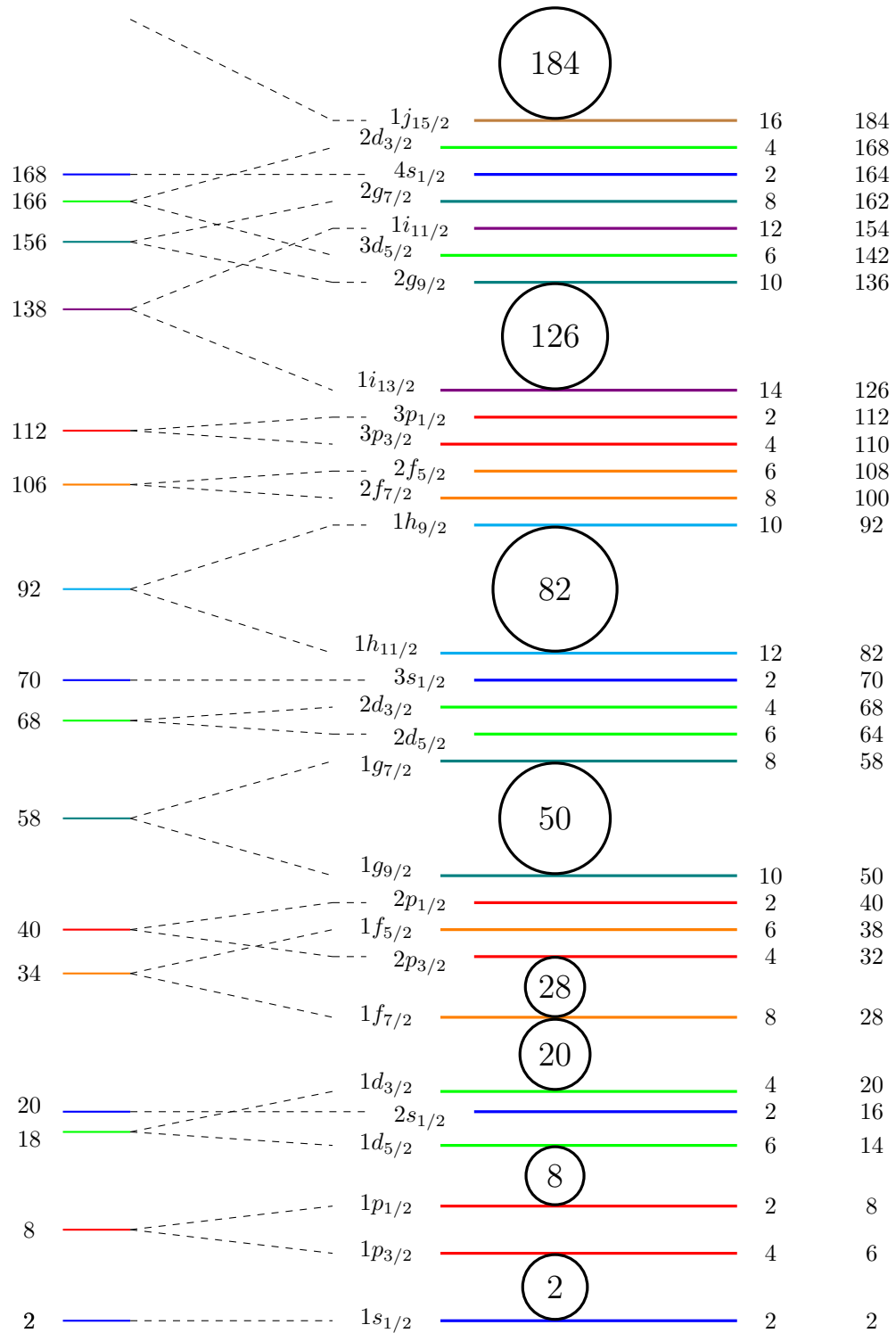


Figure 4.5: The nuclear shell model



## CHAPTER 5

## RESULTS

In the following we apply the formalism developed in the previous chapters and carry out nuclear structure calculations in order to compare the HO and the Bessel DVR bases. We will calculate ground-state energies and radii for the two closed shell nuclei  $^{16}\text{O}$  and  $^{48}\text{Ca}$  in order to investigate the conduct of our calculations for light and medium-mass nuclei, both in the HF and in the ADC2 approximations. We will employ three chiral potentials associated with different energy cutoffs, namely  $\text{N}^4\text{LO450}$ ,  $\text{N}^4\text{LO550}$  [18] and  $\text{N}^3\text{LO}(500)$  [34]. These interactions have been developed by D. R. Entem, R. Machleidt and Y. Nosyk (EMN) and they represent the state-of-the-art in the study of hadronic interactions at low energy, including contributions up to fourth order in the chiral expansion.  $\text{N}^3\text{LO}(500)$  includes contributes up to fourth order of the chiral expansion and is characterized by a 500 MeV cutoff.  $\text{N}^4\text{LO450}$  and  $\text{N}^4\text{LO550}$  are the most recent ones. These are fifth-order potentials with cutoffs of respectively 450 MeV and 550 MeV.

HF results provide a first estimate of the convergence of the studied observables, while with the ADC2 approximation we can see how the differences between the energies and the radii computed in the two bases are affected by the introduction of nuclear correlations. We will systematically investigate the infrared (IR) and ultraviolet (UV) convergence of our results. In other terms, we will study their dependence on the spatial extension and on the energy cutoff of the bases employed in our calculations. This is an important analysis because the numerical representation of wave functions requires limiting the UV and IR scales. We will first compare the HO and DVR basis in terms of the size and energy cutoff parameters introduced in Chapter 4, investigating in great detail the case of the  $\text{N}^4\text{LO450}$  potential, which is the softest of these three interac-

tions. We will then refine our study of the IR and UV convergence in Section 5.1.2. In the final part of the chapter, we will show results for the  $N^4\text{LO}550$  and  $N^3\text{LO}(500)$  potentials in order to investigate the behavior of our computations for a fair variety of Hamiltonians with different softness and analyze the main differences in terms of convergence of the computed observables.

In the various plots that we show,  $N_{max}$  and  $l_{max}$  label the dimension of the model space referred respectively to the HO and the Bessel DVR basis, as discussed in Section 4.2.3.

## 5.1 $N^4\text{LO}450$ EMN potential

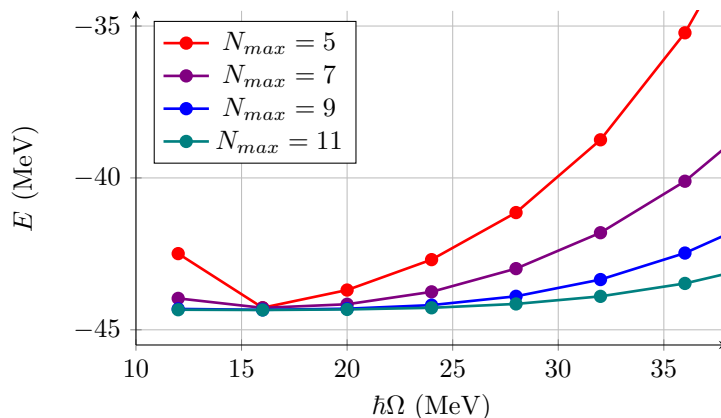


**Figure 5.1:** Convergence of the energies for  $^{16}\text{O}$  calculated with HF approximation and  $N^4\text{LO}450$  potential for different truncations of the single-particle HO basis

We start by showing results for the  $N^4\text{LO}450$  potential obtained in the HF approximation. **Figures 5.1 and 5.2** show the convergence of the energy and radius of  $^{16}\text{O}$ . The curves for the convergence of energies and radii are typically plotted as a function of  $\hbar\Omega$  in the case of the HO basis. The energy graphs are characterized by parabolic-like curves that reach a well defined minimum in correspondence of a certain value of  $\hbar\Omega$ . This value strongly depends on the particular kind of potential used and on the type of calculation performed. In the case of our soft interaction, the general experience is that correlations move the optimal  $\hbar\Omega$  to larger frequencies. In the HF approximation, as shown in **Figure 5.1**, the convergence is obtained for  $\hbar\Omega \approx 16$  MeV, in correspondence of which the minimum value of the energy is reached at  $E \approx -44.3$  MeV. The radii follow a characteristic behavior: their graph show curves that approximately decrease as  $\hbar\Omega$  increases. The oscillator length for the HO is defined as  $b_{HO} = \sqrt{\frac{\hbar}{m\Omega}}$ , so

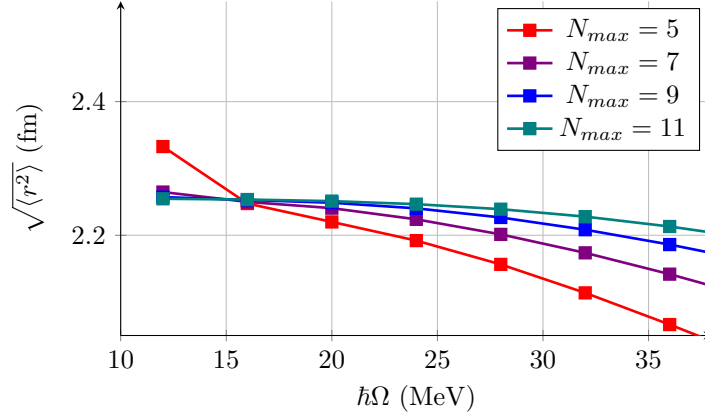


**Figure 5.2:** Convergence of the r.m.s. radii for  $^{16}\text{O}$  calculated with HF approximation and  $\text{N}^4\text{LO450}$  potential for different truncations of the single-particle HO basis

we can equally describe the behavior of the plots relating to the radii observing that they assume higher values as  $b_{HO}$  increases, becoming independent of this parameter in the limit  $N_{max} \rightarrow +\infty$ . The  $N_{max} = 5$  curve is the steepest one, and curves relative to different model spaces  $N_{max}$  tend to flatten to a horizontal curve as  $N_{max}$  increases. This can be easily seen from **Figure 5.2**, as the  $N_{max} = 11$  curve is almost constant for a large range of  $\hbar\Omega$  values. From this graph, one can easily estimate the converged value as the one for which the curves intersect with each other. In the case of **Figure 5.2**, the converged value is found at  $\sqrt{\langle r^2 \rangle} \approx 2.25$  fm.

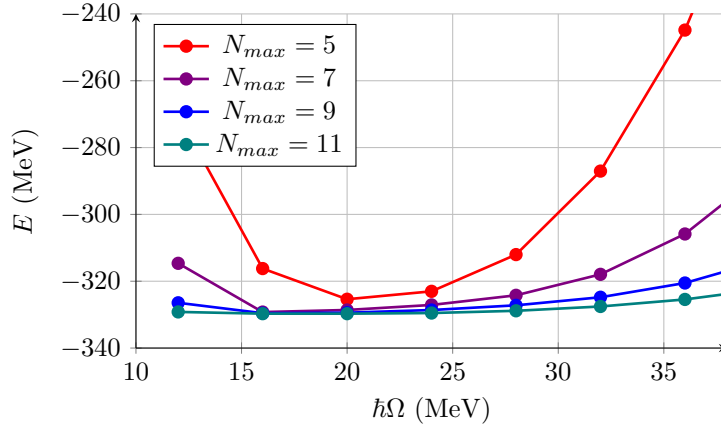


**Figure 5.3:** Convergence of the energies for  $^{48}\text{Ca}$  calculated with HF approximation and  $\text{N}^4\text{LO450}$  potential for different truncations of the single-particle HO basis

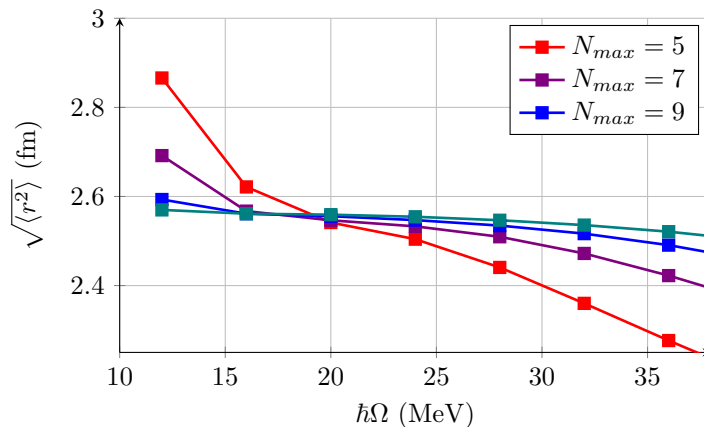


**Figure 5.4:** Convergence of the r.m.s. radii for  $^{48}\text{Ca}$  calculated with HF approximation and  $\text{N}^4\text{LO450}$  potential for different truncations of the single-particle HO basis

The results for  $^{48}\text{Ca}$  are qualitatively similar to the  $^{16}\text{O}$  ones, but the convergence is slower. The greater difficulty for heavier nuclei to converge respect to  $N_{max}$  (both in the energy and the radius) is a common limitation of any kind of nuclear structure calculation, as larger systems require bigger model spaces to be correctly described. We will see that when nuclear correlations are added to our calculations, the convergence rate become even slower, as calculations including nuclear correlations probe larger model spaces than those required by the simple HF.

We now turn to the corresponding HF calculations applied in the cases of the Bessel DVR basis. On the abscissa we represent the quantity  $\hbar^2/mR_{box}^2$ , which is analogous to the HO energy  $\hbar\Omega = \hbar^2/mb^2$  (Eq. 4.2.81) and allows us to approximately compare the results obtained in the two different bases.

The convergence pattern shows a different behavior compared to the HO basis. The curves obtained for fixed values of  $l_{max}$  are still parabolic curves, but their minimum does not correspond to a fixed value of the  $\hbar\Omega$ . It instead gets shifted to smaller values of  $\hbar\Omega$  as  $l_{max}$  increases, showing a direct dependence of the results on the box size. To study the relation between the computed energies or radii and the box size  $R_{box}$  on which the Bessel DVR are defined, we present an extrapolation of the results for the infrared limit  $R_{box} \rightarrow \infty$  for the two bases in Section 5.1.2. **Figure 5.5** shows that computations with the two model spaces  $l_{max} = 7$  and  $l_{max} = 9$  reach the same values of the energy for boxes up to  $R_{box} = 5$  fm ( $\frac{\hbar^2}{mR_{box}^2} = 1.3$  MeV) and start to differ for larger boxes. The minimum energy found for  $^{16}\text{O}$  is  $E \approx -43.7$  MeV for  $l_{max} = 9$ , in good agreement with the value  $E \approx -44.3$  MeV obtained in the case of the HO.

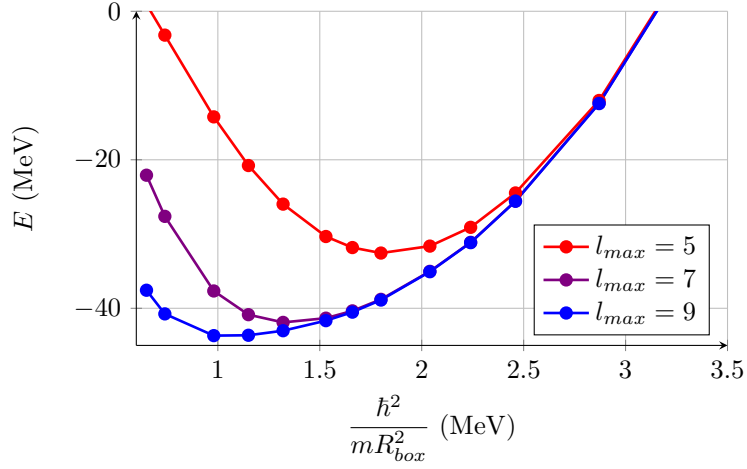


**Figure 5.5:** Convergence of the energies for  $^{16}\text{O}$  calculated with HF approximation and  $\text{N}^4\text{LO450}$  potential for different truncations of the single-particle Bessel DVR basis

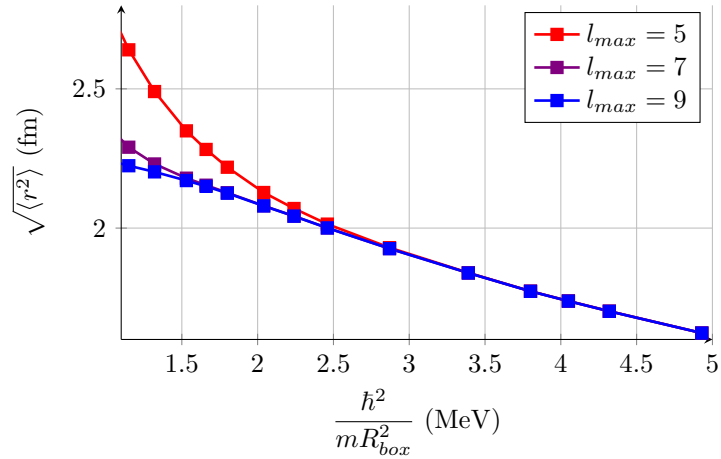


**Figure 5.6:** Convergence of the r.m.s. radii for  $^{16}\text{O}$  calculated with HF approximation and  $\text{N}^4\text{LO450}$  potential for different truncations of the single-particle Bessel DVR basis

This is quite satisfactory since it shows that the Bessel DVR basis is capable to reach the same HF energy as in the HO case with a reduced number of orbitals included in the model space. Even the radii (**Figure 5.6**) show a different behavior compared with the HO basis. The  $l_{max} = 7$  and  $l_{max} = 9$  curves almost completely overlap for values of the box up to 6 fm, showing a good UV convergence. However, they still depend on  $R_{box}$ , proving that IR convergence is still not reached.

**Figures 5.7** and **5.8** demonstrate the convergence of Bessel DVR for HF

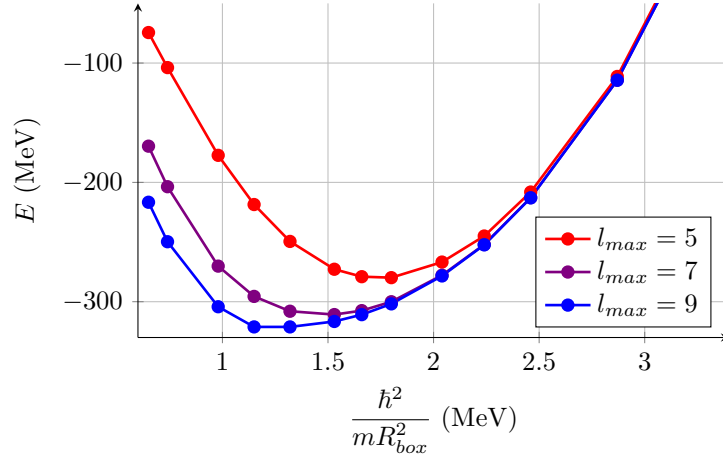


**Figure 5.7:** Convergence of the energies for  $^{48}\text{Ca}$  calculated with HF approximation and  $\text{N}^4\text{LO450}$  potential for different truncations of the single-particle Bessel DVR basis

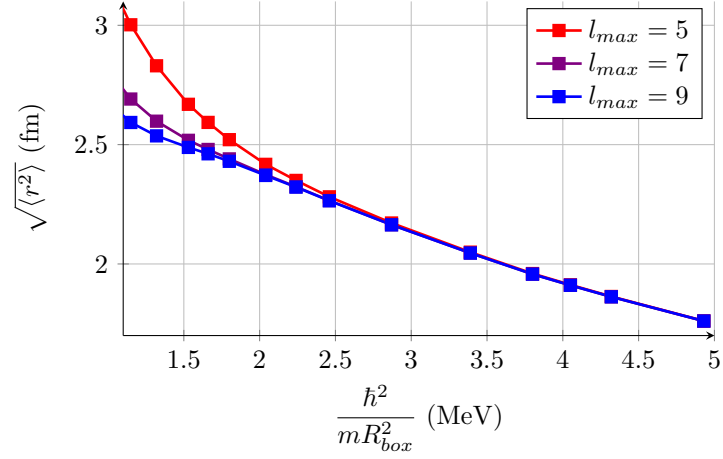


**Figure 5.8:** Convergence of the r.m.s. radii for  $^{48}\text{Ca}$  calculated with HF approximation and  $\text{N}^4\text{LO450}$  potential for different truncations of the single-particle Bessel DVR basis

computations of  $^{48}\text{Ca}$ . We find the same qualitative behavior as for  $^{16}\text{O}$ , indicating a convergence between the  $l_{max} = 7$  and  $l_{max} = 9$  model spaces for values of the box up to 5 fm. Differently from the HO case, the curves vs  $R_{box}$  don't flatten as the model space dimensions increase, but they seem to remain concave.

### 5.1.1 Center-of-mass correction for HF radii

As previously discussed, HF calculations show a dependence of the results in the Bessel DVR basis on the radius of the box even after convergence in terms of the basis dimension. To check if the center-of-mass contribution is responsible of this behavior, we subtracted it by using Eq. (1.1.4), to obtain the intrinsic r.m.s radii for both  $^{16}\text{O}$  and  $^{48}\text{Ca}$ .

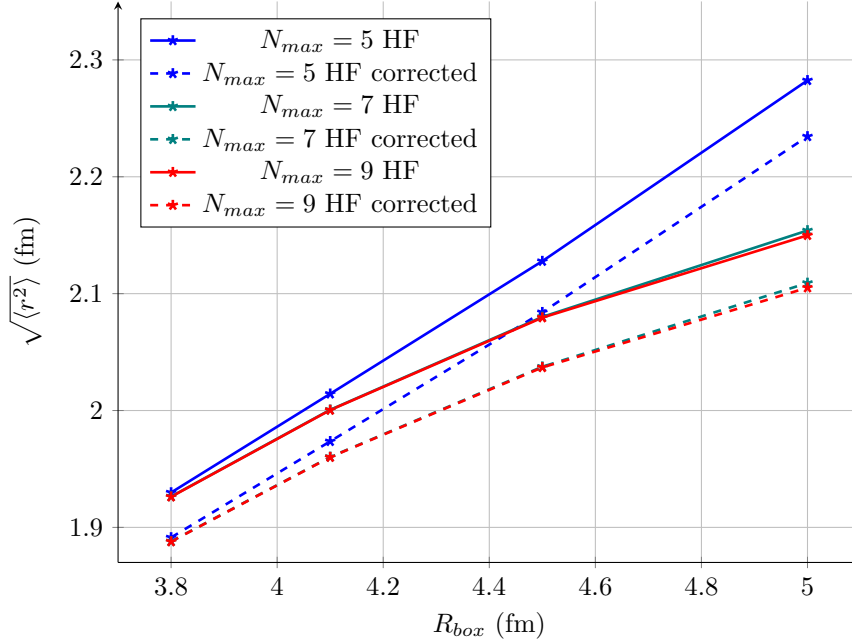


**Figure 5.9:** Comparison between the convergence of the r.m.s. radii calculated with HF approximation and the center-of-mass corrected ones. Results for  $N^4\text{LO450}$  potential and different truncations of the single-particle Bessel DVR basis are showed in the case of  $^{16}\text{O}$

**Figures 5.9** and **5.10** demonstrate a correction of about 0.05 fm for the root mean square radius relative to the HF propagator, causing only a relatively little change in the radius compared to the dependence of the choice of  $R_{box}$ . This is in line with the known impact of the COM corrections on the HF radii with the HO basis. Overall, the COM correction proved not to alter the convergence pattern.

Now we switch to a more sophisticated kind of calculations, which is the ADC2 approximation (see Section 1.2.3 for details).

The curves in **Figure 5.11** showed two main differences compared to the HF case. First of all, the convergence is reached approximately with  $N_{max} = 9$ , while for the HF calculations the parabolas are already close to a converged value for the model space  $N_{max} = 5$  (**Figure 5.1**). Second, the value to which the

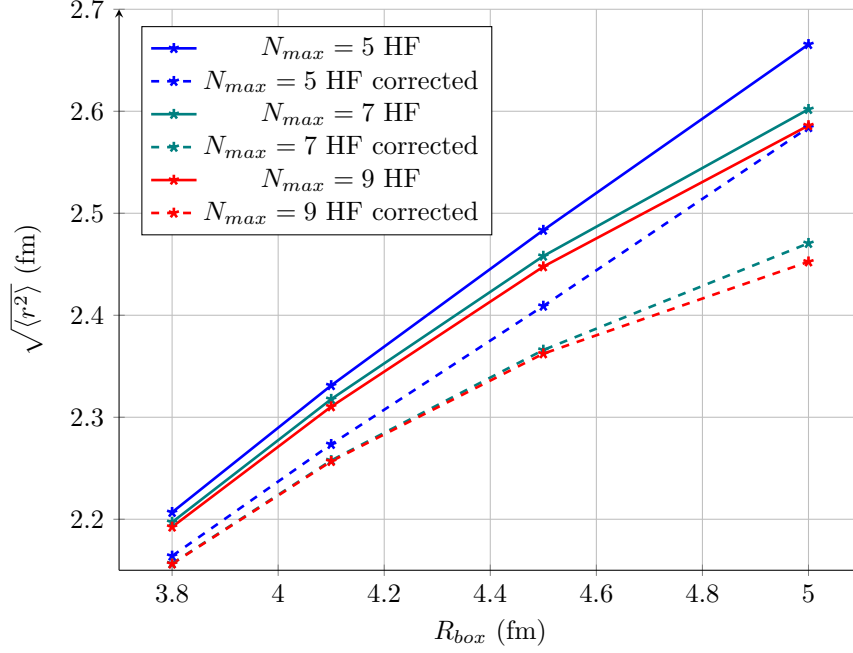


**Figure 5.10:** Comparison between the convergence of the r.m.s. radii calculated with HF approximation and the center-of-mass corrected ones. Results for  $N^4\text{LO450}$  potential and different truncations of the single-particle Bessel DVR basis are showed in the case of  $^{48}\text{Ca}$

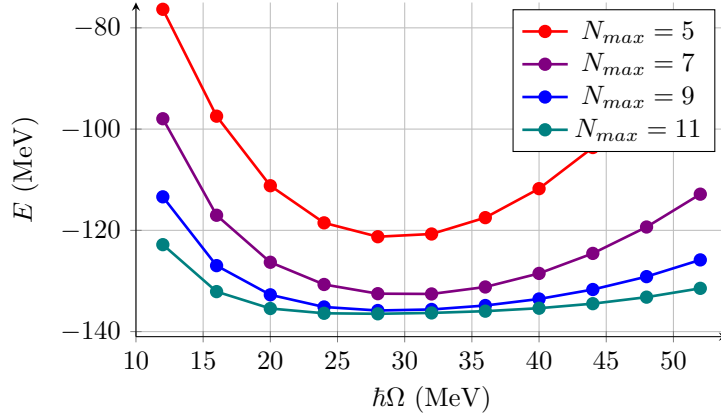


**Figure 5.11:** Convergence of the ground-state energy for  $^{16}\text{O}$  calculated with ADC2 approximation and  $N^4\text{LO450}$  potential for different truncations of the single-particle HO basis

ground-state energy converges is  $\hbar\Omega \approx 28 - 32$  MeV, which is higher compared to the energy  $\hbar\Omega = 16$  MeV in the HF case, showing the large effect of correlations. The radii as well show a convergence at higher values of  $\hbar\Omega$ , as the intersection

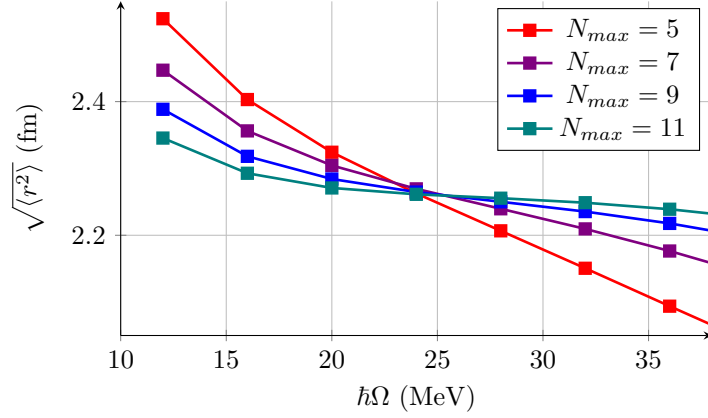


**Figure 5.12:** Convergence of the r.m.s. radii for  $^{16}\text{O}$  calculated with ADC2 approximation and  $\text{N}^4\text{LO450}$  potential for different truncations of the single-particle HO basis

point of the curves showed in **Figure 5.12** is found in correspondence of  $\hbar\Omega = 24$  MeV.

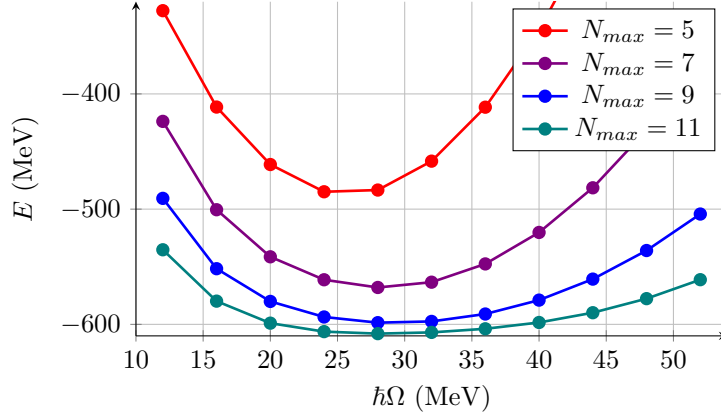


**Figure 5.13:** Convergence of the ground-state energy for  $^{48}\text{Ca}$  calculated with ADC2 approximation and  $\text{N}^4\text{LO450}$  potential for different truncations of the single-particle HO basis

In the case of  $^{48}\text{Ca}$ , the difficulty for the energies to converge seems to be amplified respect to the HF calculations. In **Figure 5.14** it seems important to include all the partial-wave contributes up to the model space  $N_{max} = 11$ . The estimated value of the ground-state energy is  $E \approx -608.06$  MeV, while the radii converge at  $\sqrt{\langle r^2 \rangle} \approx 2.5$  fm.

In **Figure 5.15** and **5.16** we performed the same ADC2 calculations for the Bessel DVR basis. In the case of  $^{16}\text{O}$ , the two ground-state energy found are  $E^{HO} \approx -136.48$  MeV and  $E^{DVR} \approx -124.91$  MeV. As in the HF case, **Figure**

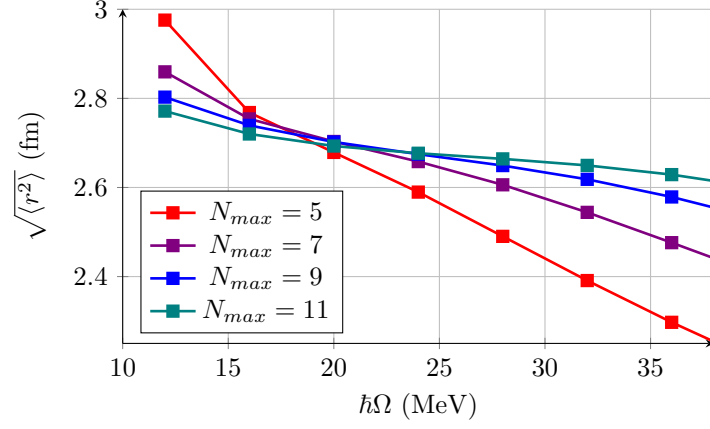


**Figure 5.14:** Convergence of the r.m.s. for  $^{48}\text{Ca}$  calculated with ADC2 approximation and  $\text{N}^4\text{LO450}$  potential for different truncations of the single-particle HO basis

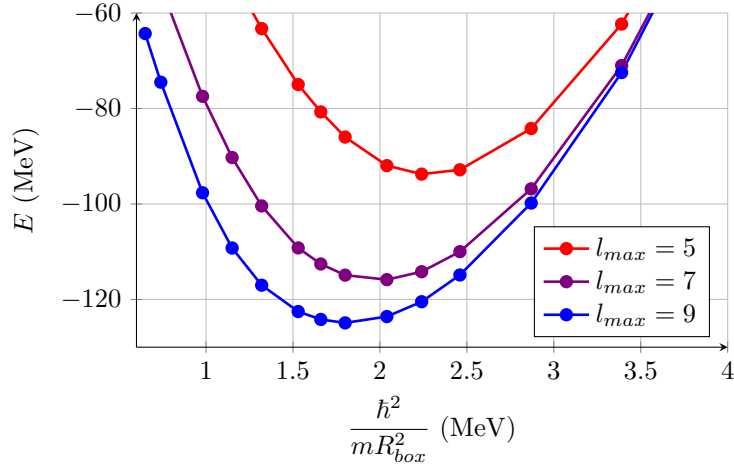


**Figure 5.15:** Convergence of the ground-state energy for  $^{16}\text{O}$  calculated with ADC2 approximation and  $\text{N}^4\text{LO450}$  potential for different truncations of the single-particle Bessel DVR basis

**5.16** shows that for  $l_{max} = 7$  and  $l_{max} = 9$  the curves are overlapped for almost all the values of the showed boxes  $R_{box}$ . The Bessel DVR basis seems then to have a good behavior in the description on the mean squared radii even for more complex calculations than HF.

Finally, we present the results obtained for the Bessel DVR and the  $^{48}\text{Ca}$  nucleus. The computed ground-state energy ( $E^{DVR} \approx -535.57$  MeV) is not so close to the value that we found in the case of the HO ( $E^{HO} \approx -608.06$  MeV), and this could imply the need to include bigger model spaces for heavier nu-

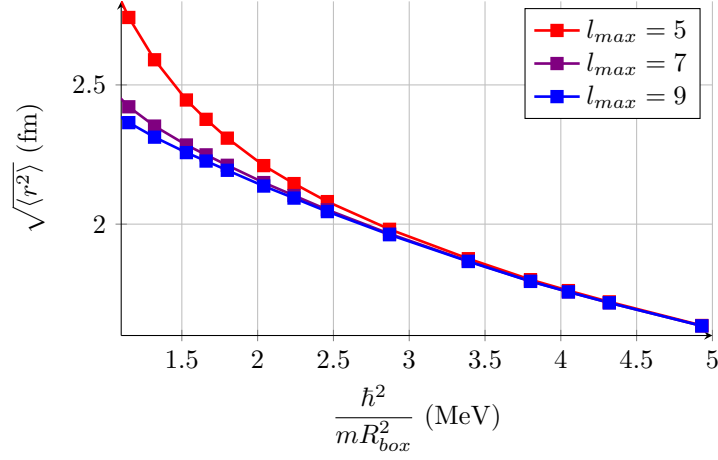


**Figure 5.16:** Convergence of the r.m.s. radii for  $^{16}\text{O}$  calculated with ADC2 approximation and  $\text{N}^4\text{LO450}$  potential for different truncations of the single-particle Bessel DVR basis

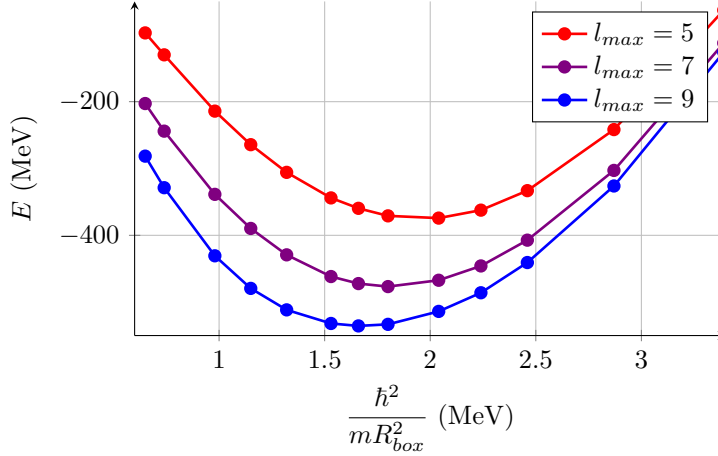


**Figure 5.17:** Convergence of the ground-state energy for  $^{48}\text{Ca}$  calculated with ADC2 approximation and  $\text{N}^4\text{LO450}$  potential for different truncations of the single-particle Bessel DVR basis

clei. Once again, the radii show a better convergence than the energies, having reached approximately fixed values at  $l_{max} = 7$ .

### 5.1.2 Extrapolations toward low- and high-momentum scales

In this section we study the IR and UV scales, which respectively represent the largest physical extent and the highest representable momenta of the selected wave functions.

First, we consider the IR convergence of the energies and radii for the  $^{16}\text{O}$

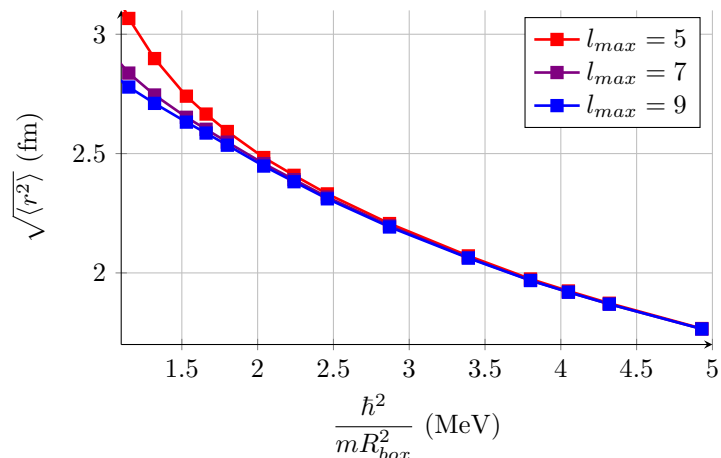


**Figure 5.18:** Convergence of the ground-state energy for  $^{48}\text{Ca}$  calculated with ADC2 approximation and  $\text{N}^4\text{LO450}$  potential for different truncations of the single-particle Bessel DVR basis

and  $^{48}\text{Ca}$ . Calculations of the nuclear observables that result from a nuclear structure calculation should be ideally independent from the dimensions  $N_{max}$  and  $l_{max}$  of the models spaces chosen for the computation. In practice, this independence is never reached, so different attempts to do extrapolations have been done in the past years to correct the approximate values of the observables that follows from the truncation of the model space.

For the Bessel DVR functions, which are defined in a box, studying the IR convergence of energies and radii is equivalent to take the limit  $R_{box} \rightarrow \infty$ . In the harmonic oscillator case, it has been shown [36, 35] that for a given value of  $\hbar\Omega$  a suitable quantity is provided by

$$L_2 = \sqrt{2(N_{max} + 3/2 + 2)}b. \quad (5.1.1)$$

We can then use  $L_2$  as the reference value for the effective box in which the HO is constrained, to be compared with the  $R_{box}$  of the Bessel DVR's. As we are interested in the IR convergence, we need to extrapolate the values of the energies and the radii in the limit  $R_{box} \rightarrow +\infty$ .

First we show the results relative to energies and radii in the ADC2 approximation, plotting the HO curves as a function of the variable  $L_2$  from Eq. (5.1.1) and the Bessel DVR ones as a function of the box  $R_{box}$ .

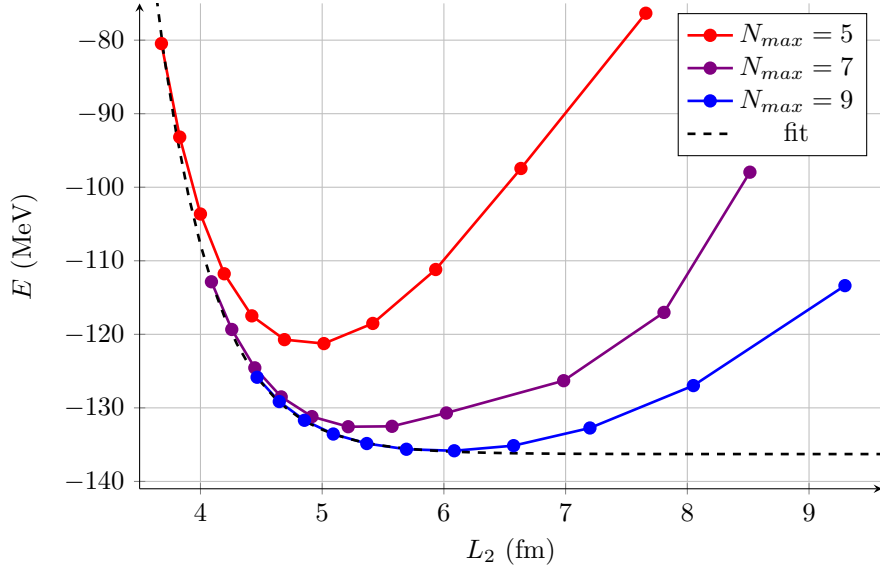


**Figure 5.19:** Convergence of the ground-state energy for  $^{16}\text{O}$  calculated with ADC2 approximation and  $\text{N}^4\text{LO450}$  potential for different truncations of the single-particle HO basis. The abscissa represents the effective HO box (Eq. (5.1.1)). The dashed line is the result of the fitting procedure (Eq. (5.1.2))

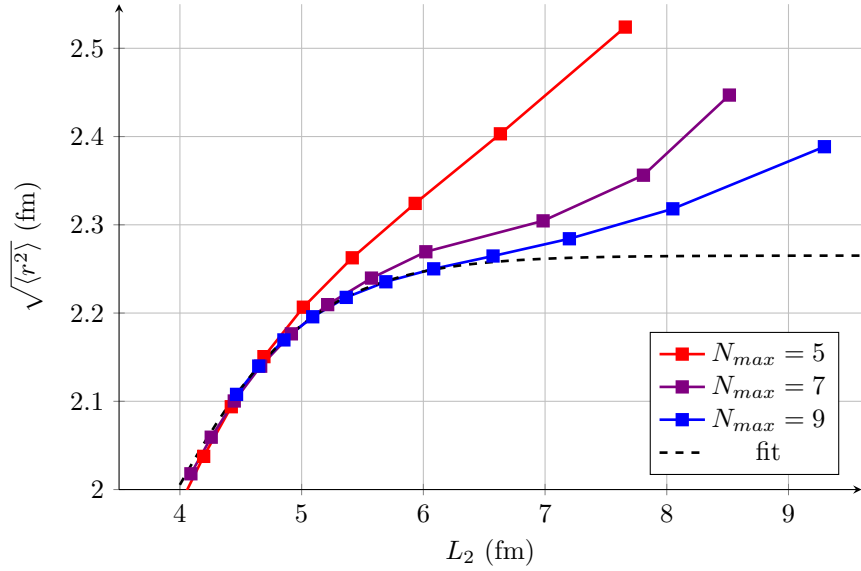


**Figure 5.20:** Convergence of the r.m.s. radii for  $^{16}\text{O}$  calculated with ADC2 approximation and  $\text{N}^4\text{LO450}$  potential for different truncations of the single-particle HO basis. The abscissa represents the effective HO box (Eq. (5.1.1)). The dashed line is the result of the fitting procedure (Eq. (5.1.3))

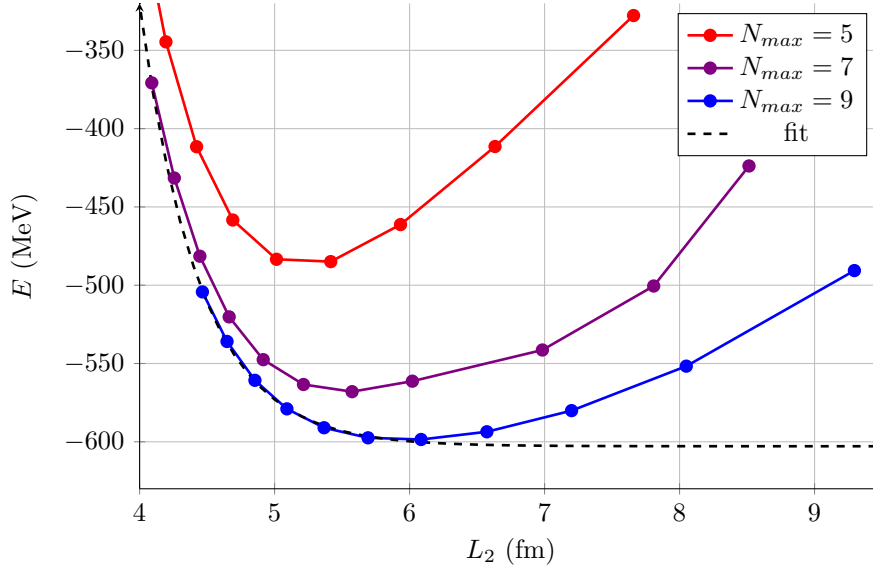


**Figure 5.21:** Convergence of the ground-state energy for  $^{48}\text{Ca}$  calculated with ADC2 approximation and  $N^4\text{LO450}$  potential for different truncations of the single-particle HO basis. The abscissa represents the effective HO box (Eq. (5.1.1)). The dashed line is the result of the fitting procedure (Eq. (5.1.2))

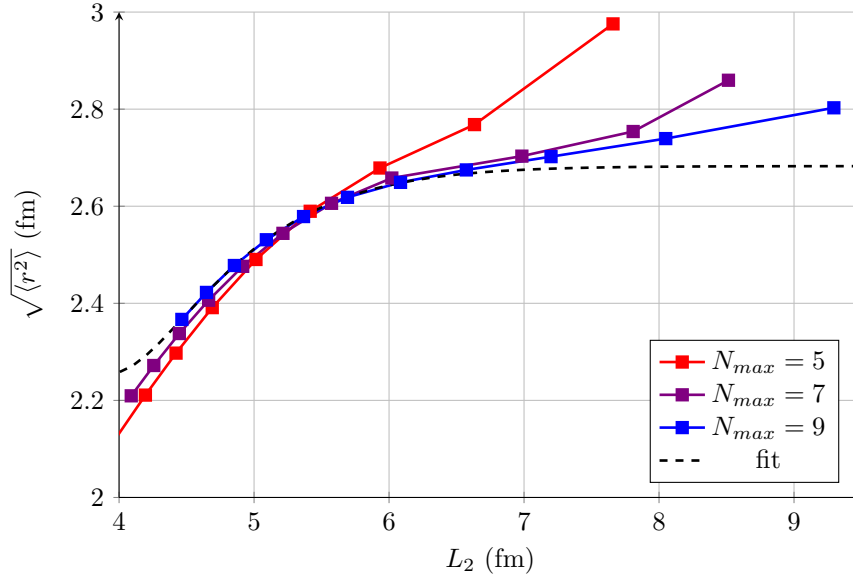


**Figure 5.22:** Convergence of the ground-state energy for  $^{48}\text{Ca}$  calculated with ADC2 approximation and  $N^4\text{LO450}$  potential for different truncations of the single-particle HO basis. The abscissa represents the effective HO box (Eq. (5.1.1)). The dashed line is the result of the fitting procedure (Eq. (5.1.3))

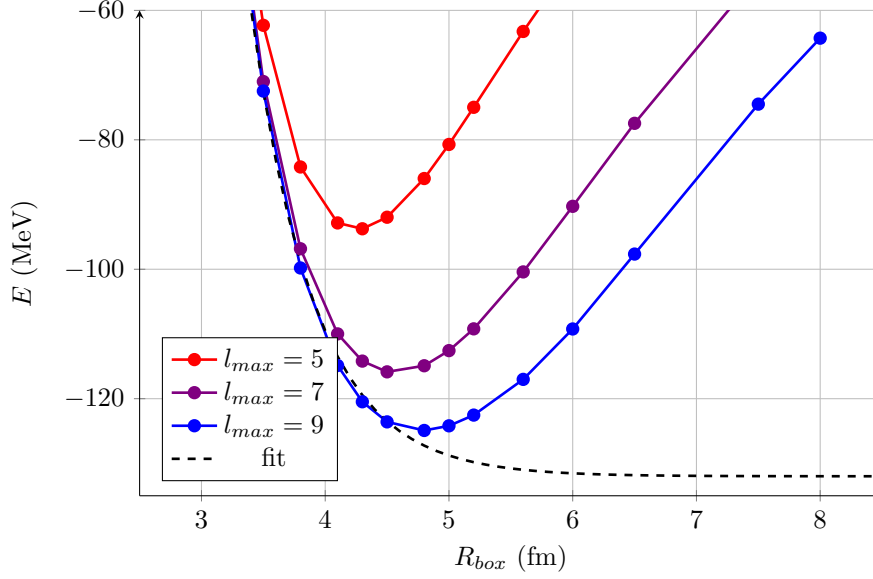


**Figure 5.23:** Convergence of the ground-state energy for  $^{16}\text{O}$  calculated with ADC2 approximation and  $\text{N}^4\text{LO450}$  potential for different truncations of the single-particle Bessel DVR basis. The dashed line is the result of the fitting procedure (Eq. (5.1.2))

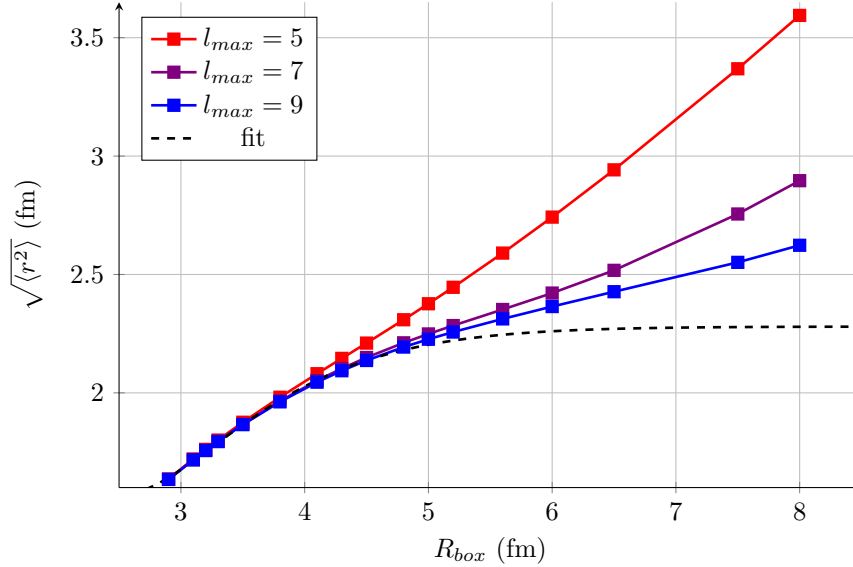


**Figure 5.24:** Convergence of the r.m.s. radii for  $^{16}\text{O}$  calculated with ADC2 approximation and  $\text{N}^4\text{LO450}$  potential for different truncations of the single-particle Bessel DVR basis. The dashed line is the result of the fitting procedure (Eq. (5.1.3))

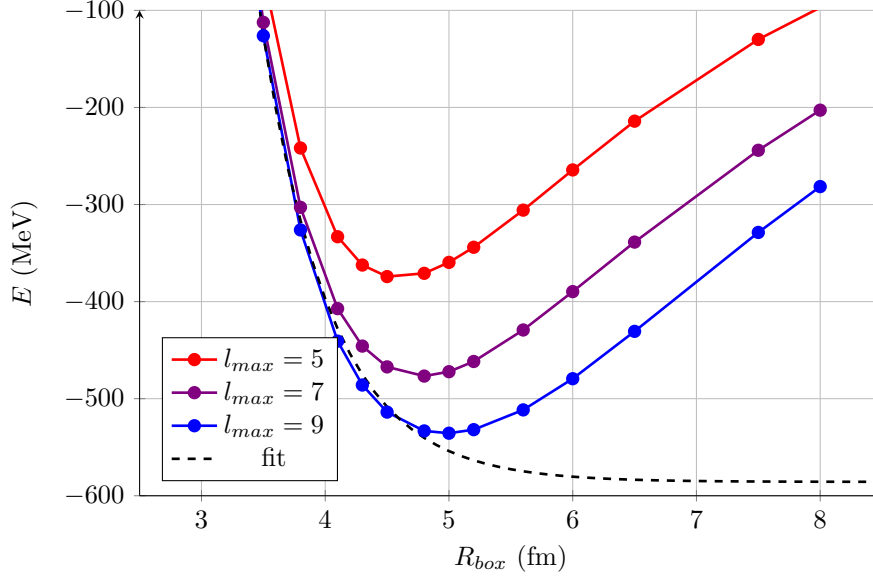


**Figure 5.25:** Convergence of the ground-state energy for  $^{48}\text{Ca}$  calculated with ADC2 approximation and  $\text{N}^4\text{LO450}$  potential for different truncations of the single-particle Bessel DVR basis. The dashed line is the result of the fitting procedure (Eq. (5.1.2))

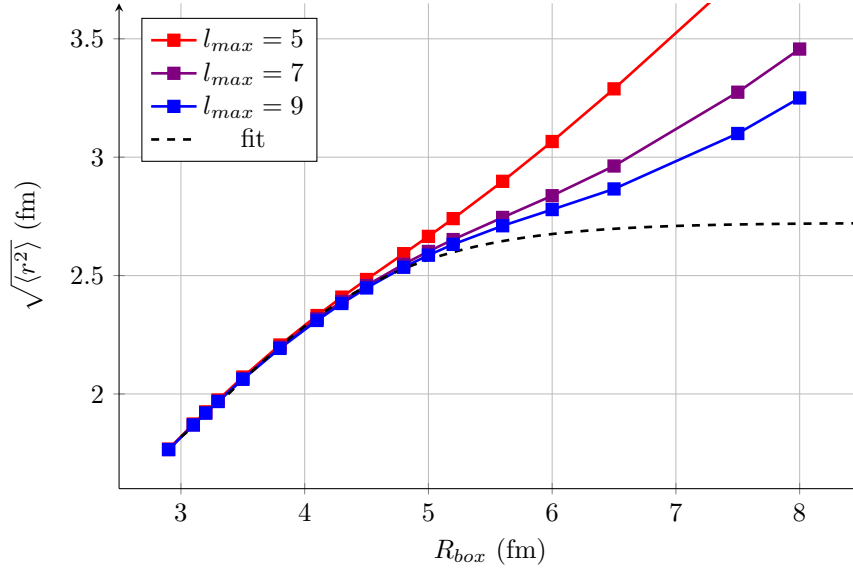


**Figure 5.26:** Convergence of the r.m.s. radii for  $^{48}\text{Ca}$  calculated with ADC2 approximation and  $\text{N}^4\text{LO450}$  potential for different truncations of the single-particle Bessel DVR basis. The dashed line is the result of the fitting procedure (Eq. (5.1.3))

The IR limit can be studied once the ultraviolet convergence is reached (once high momenta are included in the model space). We use the main results from [35], who have theoretically proven that in the case of a HO it can be described as a wave function in a hard-wall radius  $L$ . The relation between the energy and the box radius can be estimated using the following relation:

$$E_L = E_\infty + a_0 e^{-2k_\infty L}, \quad (5.1.2)$$

with  $a_0$ ,  $E_0$  and  $k_\infty$  parameters. On the other hand, the dependence of the radii from the box is written as

$$\langle r^2 \rangle_L \approx \langle r^2 \rangle_\infty [1 - (c_0 \beta^3 + c_1 \beta) e^{-\beta}], \quad (5.1.3)$$

with  $\langle r^2 \rangle_\infty$ ,  $c_0$ ,  $c_1$  parameters and  $k_\infty$  determined from the fit on the energy. In the case of the Bessel DVR basis, the parameter which regulates the IR convergence is represented by  $R_{box}$ . We used the short notation  $\beta = 2k_\infty L$ .

We used equations (5.1.2) and (5.1.3) to fit the values of the ground state energies and the mean square radii that we found from ADC2 computations. The results of the fits are summarized in Tables 5.27 and 5.28, where the uncertainties are given by the asymptotic standard error resulting from the fitting procedure. The fitting curves are showed in Figures 5.23, 5.24, 5.25 and 5.26.

	$E_0$	$a_0$	$k_\infty$
$^{16}\text{O}(\text{HO})$	$-\mathbf{136.28} \pm 0.10$	$152954 \pm 4454$	$1.07 \pm 0.03$
$^{16}\text{O}(\text{DVR})$	$-\mathbf{131.99} \pm 1.01$	$53846 \pm 5499$	$0.97 \pm 0.02$
$^{48}\text{Ca}(\text{HO})$	$-\mathbf{602.84} \pm 1.38$	$2230330 \pm 987100$	$1.12 \pm 0.05$
$^{48}\text{Ca}(\text{DVR})$	$-\mathbf{585.70} \pm 8.77$	$235842 \pm 2854$	$0.89 \pm 0.02$

**Figure 5.27:** Energy fit values for  $N_{max} = 9$  (HO) and  $l_{max} = 9$  (DVR)

	$\sqrt{\langle r^2 \rangle_\infty}$	$c_0$	$c_1$
$^{16}\text{O}(\text{HO})$	$\mathbf{2.2651} \pm 0.0008$	$1.86 \pm 0.07$	$-66 \pm 6$
$^{16}\text{O}(\text{DVR})$	$\mathbf{2.280} \pm 0.009$	$0.70 \pm 0.04$	$-8 \pm 1$
$^{48}\text{Ca}(\text{HO})$	$\mathbf{2.6826} \pm 0.0011$	$6.25 \pm 0.12$	$-364 \pm 11$
$^{48}\text{Ca}(\text{DVR})$	$\mathbf{2.722} \pm 0.013$	$0.68 \pm 0.03$	$-6 \pm 1$

**Figure 5.28:** Radii fit values for  $N_{max} = 9$  (HO) and  $l_{max} = 9$  (DVR)

Tables 5.27 and 5.28 show an improved compatibility of the results between

the two basis, especially in the case of the radii, while the energies still struggle to find a good agreement within the fitting uncertainties. The values found for the radii could be considered to be compatible if we consider that the center-of-mass correction found for the HF propagator in the Bessel DVR basis is of the order of 0.5 fm.

Now we consider the opposite problem compared to what we have just seen, analyzing the case of the UV limit, which is associated to functions defined on small boxes, in contrast to the IR limit which is associated to large boxes. The UV convergence that we are studying is related to the highest momenta that are reached by the considered basis. In the case of the HO, [37] proved that in order to investigate the UV limit we can proceed in analogy with what we have seen in the case of the IR limit, as UV effects are equally described imposing a sharp momentum cutoff at momentum  $\Lambda_2$  complementary to  $L_2$  (Eq. (5.1.1))

$$\Lambda_2 = \sqrt{2(N_{max} + 3/2 + 2)}\hbar c/b, \quad (5.1.4)$$

which differs from the definition used in [35]

$$\Lambda_0 = \sqrt{2(N_{max} + 3/2)}\hbar c/b \quad (5.1.5)$$

by a correction  $\Delta = 2$  in the square root. This correction is derived for both the IR and UV limits in [38]. In the case of the Bessel DVR basis, the momentum cutoff that we considered is given by the highest value among all the momenta associated to the partial waves in our model space

$$\Lambda_2^{DVR} = \max_{(n,l) \in \text{MS}} [k_{nl}] \hbar c = \max_{(n,l) \in \text{MS}} \left[ \frac{z_{nl}}{R_{box}} \right] \hbar c, \quad (5.1.6)$$

where  $z_{nl}$  as usual represents the  $(n+1)$ -zero of the spherical Bessel function of order  $l$  and MS represents all the partial waves included in the Bessel model space (discussed in detail in Section 4.2.3).  $k_{nl} = z_{nl}/R_{box}$  represents the momentum associated to the partial wave with quantum numbers  $nl$ .

It is interesting to notice the following: in the case of the HO

$$L_2 \Lambda_2 = 2(N_{max} + 3/2 + 2), \quad (5.1.7)$$

so the product between the cutoffs in the coordinate and momentum spaces that we used to represent the finite HO depends only on the number of degree of freedom of our basis. Similarly, in the case of the Bessel function the product of the two cutoffs reads

$$k_{nl}^{max} R_{box} = \frac{z_{nl}^{max}}{R_{box}} R_{box} = z_{nl}^{max}, \quad (5.1.8)$$

which again depends only on the number of degree of freedom covered by the model space.

To show the UV convergence of the two bases, we produced images analogous to **Figure 2** from [37]. On the  $y$ -axis the value  $|\Delta E/E_{gs}|$  is represented, with  $\Delta E = E_{gs} - E$ .  $E$  is the energy that we obtained from our computations for each  $N_{max}(/l_{max})$  and  $\hbar\Omega(/R_{box})$ , while  $E_{gs}$  is a reference energy that we chose to be the minimum energy found for the HO in  $N_{max} = 11$ :  $E(\text{O16}) = -136.48 \text{ MeV}$  and  $E(\text{Ca48}) = -606.978 \text{ MeV}$ . On the abscissa we represented the values of the momentum cutoff in the two bases,  $\Lambda_2$  and  $\Lambda_2^{DVR}$ . The lines represented are associated to fixed values of the IR cutoff ( $L_2$  for HO and  $R_{box}$  for Bessel DVR). In the case of the HO, as we computed values of the energy for different values of  $N_{max}$  and  $\hbar\Omega$ , we had to extrapolate the lines associated to fixed values of the box through an interpolation. The curves are displayed on a semilogarithmic axis in **Figures 5.29** and **5.30**. They show that in the limit of small boxes the energies seem to allineate to the same values. Interestingly, the calculations carried out for the DVR basis seem to correspond to systematically smaller values of  $\Lambda_2$  than for the HO basis.

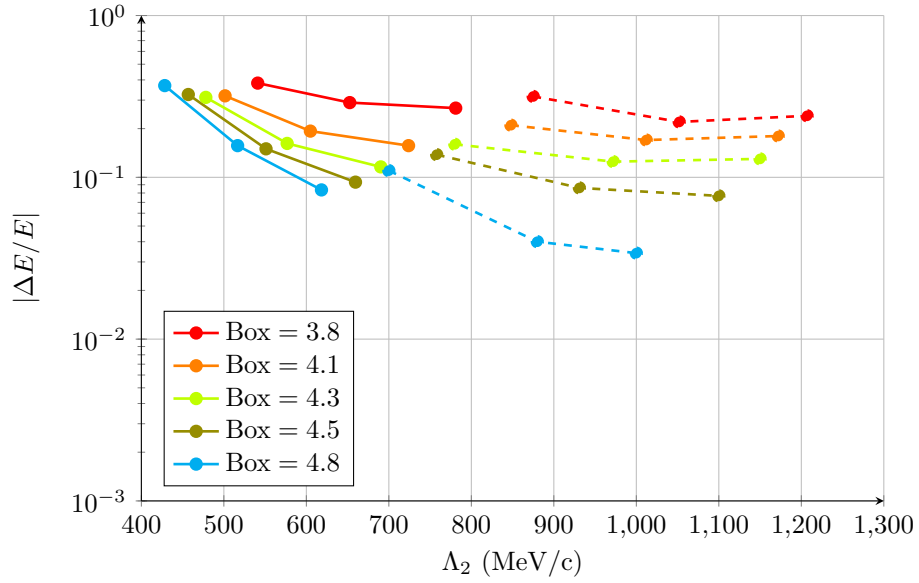


**Figure 5.29:** UV convergence for  $^{16}\text{O}$  and  $\text{N}^4\text{LO450}$  and potential. Solid lines: DVR. Dashed lines: HO. The box represents  $R_{\text{box}}$  for the DVR basis and  $L_2$  for the HO basis.

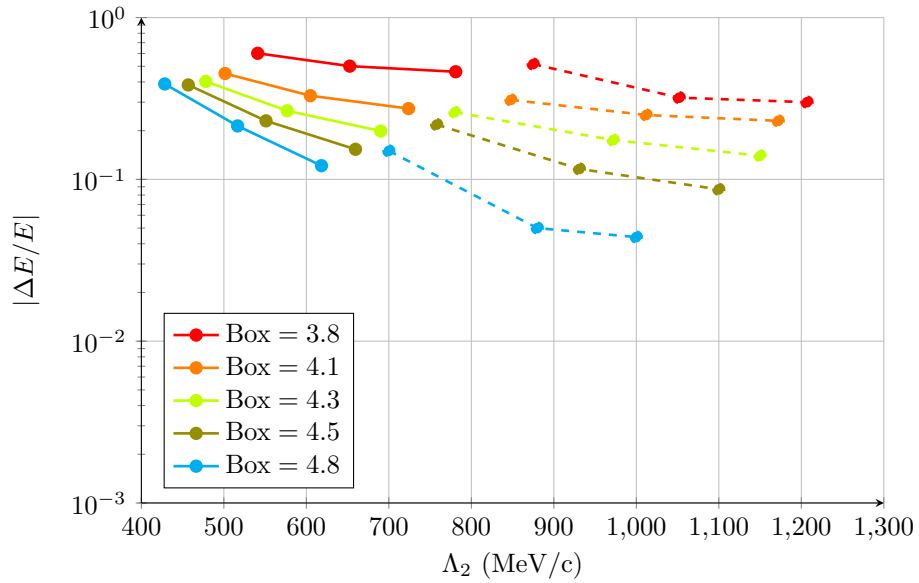


**Figure 5.30:** UV convergence for  $^{48}\text{Ca}$  and  $\text{N}^4\text{LO450}$  potential. Solid lines: DVR. Dashed lines: HO. The box represents  $R_{\text{box}}$  for the DVR basis and  $L_2$  for the HO basis.

## 5.2 Tests with different kinds of potentials

In this section, we are going to repeat the same kind of calculations seen in the case of the  $N^4\text{LO}450$  potential for other two potentials,  $N^4\text{LO}550$  and  $N^3\text{LO}(500)$ . A quick description and background of this interactions can be found in the beginning of this chapter. It is important to test the Bessel DVR basis on this variety of potentials to appreciate the different behavior in terms of convergence and quality of the results that the impact of different cutoffs brings.

### 5.2.1 $N^4\text{LO}550$ EMN potential

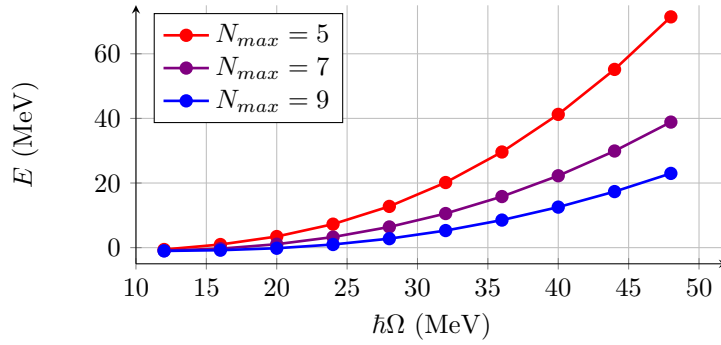


**Figure 5.31:** Convergence of ground-state energies for  $^{16}\text{O}$  calculated with HF approximation and  $N^4\text{LO}550$  potential for different truncations of the single-particle HO basis

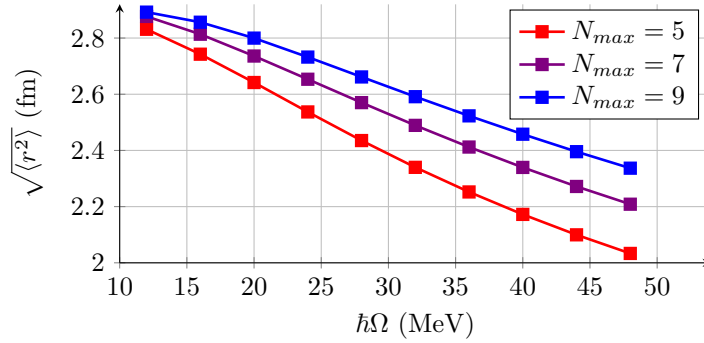


**Figure 5.32:** Convergence of the r.m.s. radii for  $^{16}\text{O}$  calculated with HF approximation and  $N^4\text{LO}550$  potential for different truncations of the single-particle HO basis

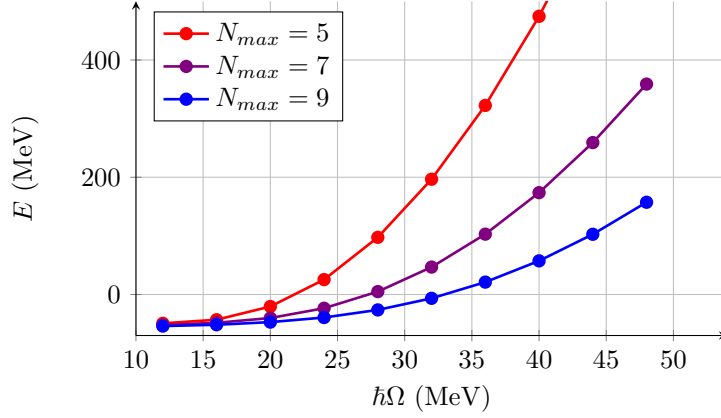


**Figure 5.33:** Convergence of the ground-state energies for  $^{48}\text{Ca}$  calculated with HF approximation and  $\text{N}^4\text{LO550}$  potential for different truncations of the single-particle HO basis

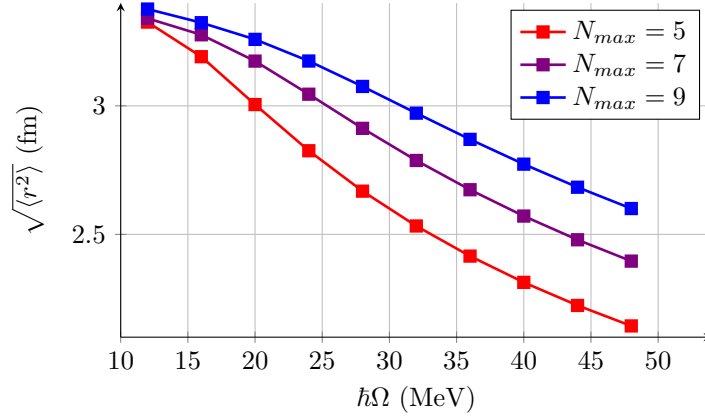


**Figure 5.34:** Convergence of the r.m.s. radii for  $^{48}\text{Ca}$  calculated with HF approximation and  $\text{N}^4\text{LO550}$  potential for different truncations of the single-particle HO basis

The first thing that we can notice from **Figures 5.31** and **5.33** is that the HF energy assumes positive values for most values of  $\hbar\Omega$ . This behavior is expected for hard interactions and is due to the highly repulsive core that characterizes them. The radii as well show a different behavior from the  $\text{N}^4\text{LO450}$  case, as the intersection point of the curves with different  $N_{max}$  seems to be reached for  $\hbar\Omega = 12$  MeV or even smaller values not represented in the graph.

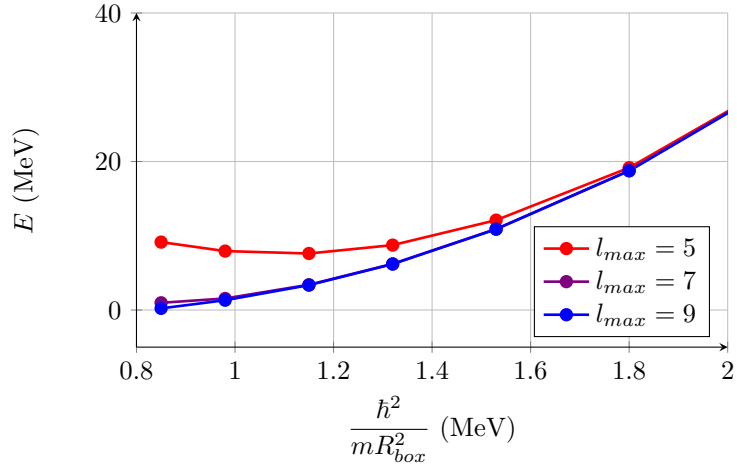


**Figure 5.35:** Convergence of the ground-state energies for  $^{48}\text{Ca}$  calculated with HF approximation and  $\text{N}^4\text{LO550}$  potential for different truncations of the single-particle Bessel DVR basis

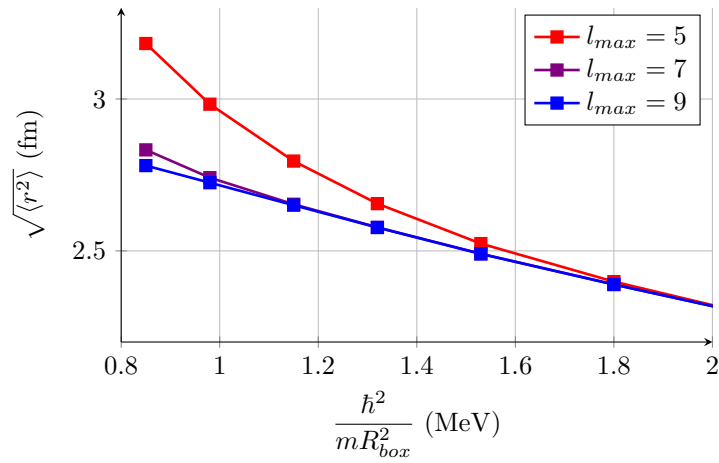


**Figure 5.36:** Convergence of the r.m.s. radii for  $^{48}\text{Ca}$  calculated with HF approximation and  $\text{N}^4\text{LO550}$  potential for different truncations of the single-particle Bessel DVR basis

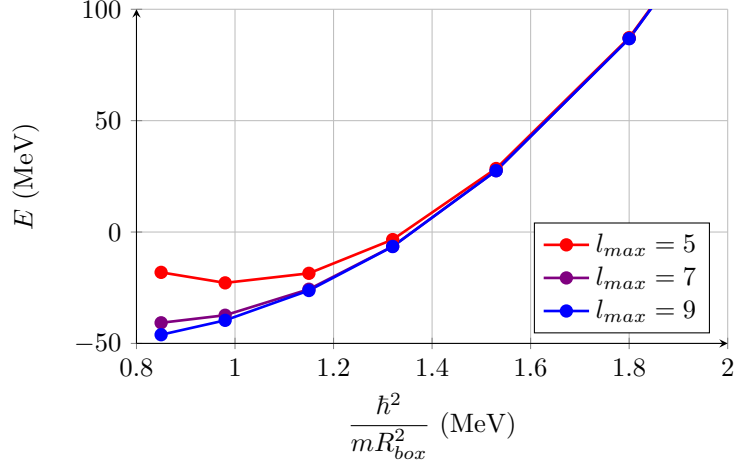


**Figure 5.37:** Convergence of the ground-state energies for  $^{48}\text{Ca}$  calculated with HF approximation and  $\text{N}^4\text{LO550}$  potential for different truncations of the single-particle Bessel DVR basis

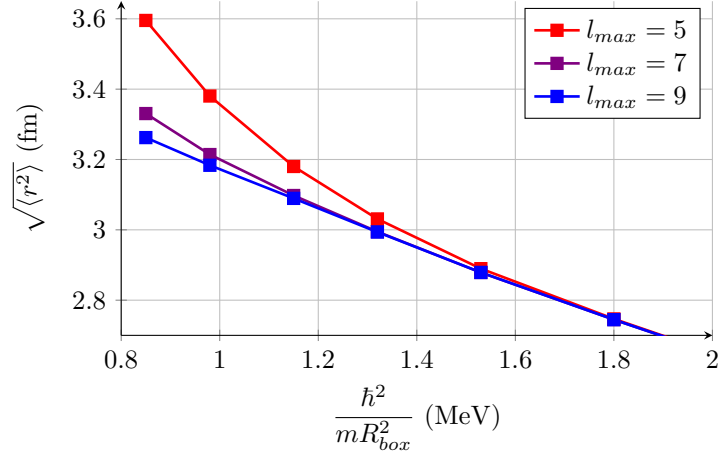


**Figure 5.38:** Convergence of the r.m.s. radii for  $^{48}\text{Ca}$  calculated with HF approximation and  $\text{N}^4\text{LO550}$  potential for different truncations of the single-particle Bessel DVR basis

Bessel DVR's seems to behave better than the HO basis in terms of convergence. In **Figures 5.35, 5.36, 5.37** and **5.38**, different curves with  $l_{max} = 7$  overlap almost completely with the corresponding  $l_{max} = 9$ , still the HF energy is compatible: in the case of  $^{16}\text{O}$  we found  $E^{HO} \approx -1.02 \text{ MeV}$  and  $E^{DVR} \approx -0.22 \text{ MeV}$ , while for  $^{48}\text{Ca}$  the HF energies are given by  $E^{HO} \approx -46.11 \text{ MeV}$  and  $E^{DVR} \approx -53.89 \text{ MeV}$ .

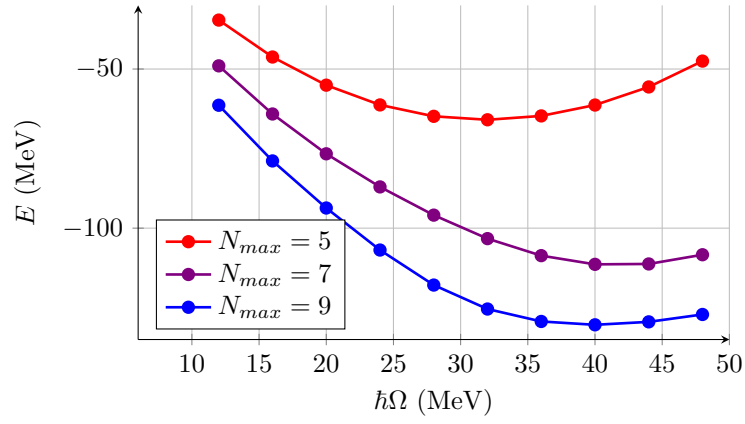


**Figure 5.39:** Convergence of the ground-state energies for  $^{16}\text{O}$  calculated with ADC2 approximation and  $\text{N}^4\text{LO550}$  potential for different truncations of the single-particle HO basis

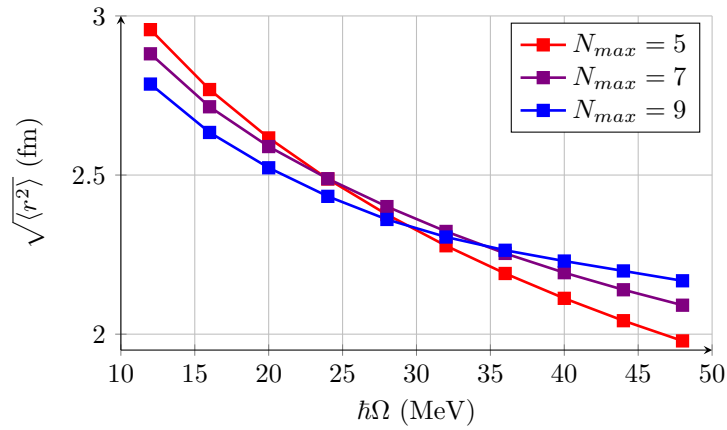


**Figure 5.40:** Convergence of the r.m.s. radii for  $^{16}\text{O}$  calculated with ADC2 approximation and  $\text{N}^4\text{LO550}$  potential for different truncations of the single-particle HO basis

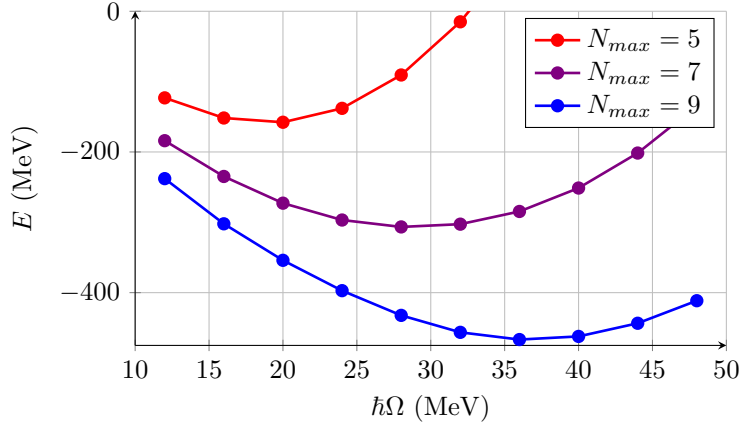


**Figure 5.41:** Convergence of the ground-state energy for  $^{48}\text{Ca}$  calculated with ADC2 approximation and  $\text{N}^4\text{LO550}$  potential for different truncations of the single-particle HO basis

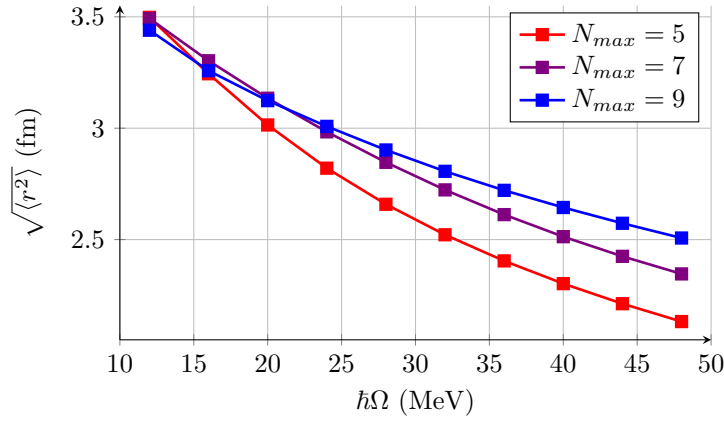


**Figure 5.42:** Convergence of the r.m.s. radii for  $^{48}\text{Ca}$  calculated with ADC2 approximation and  $\text{N}^4\text{LO550}$  potential for different truncations of the single-particle HO basis

ADC2 calculations performed with the HO basis show two main differences respect to the softer  $\text{N}^4\text{LO450}$  one. First, the convergence seems not to be reached with  $N_{max} = 9$ : the minimum reached with this model space differs from the value found for  $N_{max} = 7$  from about 10 MeV for  $^{16}\text{O}$  and 150 MeV for  $^{48}\text{Ca}$ . Second, the ground-state energy varies for different  $\hbar\Omega$ , shifting to higher values as  $N_{max}$  grows (in the case of  $\text{N}^4\text{LO450}$  the ground-state energy assumed approximately the same values of  $\hbar\Omega$  for different  $N_{max}$ ). The radii seem to converge at  $\sqrt{\langle r^2 \rangle} \approx 2.3$  fm for  $\hbar\Omega \approx 30$  MeV in the case of  $^{16}\text{O}$ . For  $^{48}\text{Ca}$ , the same convergence is reached at  $\sqrt{\langle r^2 \rangle} \approx 3.2$  fm for  $\hbar\Omega \approx 16$  MeV.

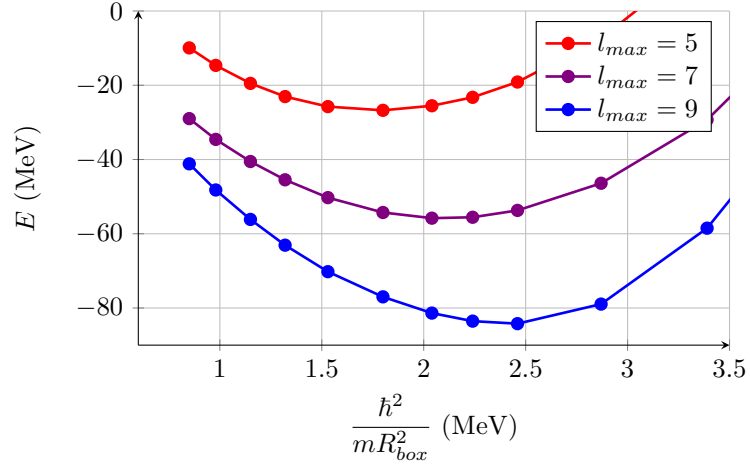


**Figure 5.43:** Convergence of the ground-state energy for  $^{16}\text{O}$  calculated with ADC2 approximation and  $\text{N}^4\text{LO550}$  potential for different truncations of the single-particle Bessel DVR basis

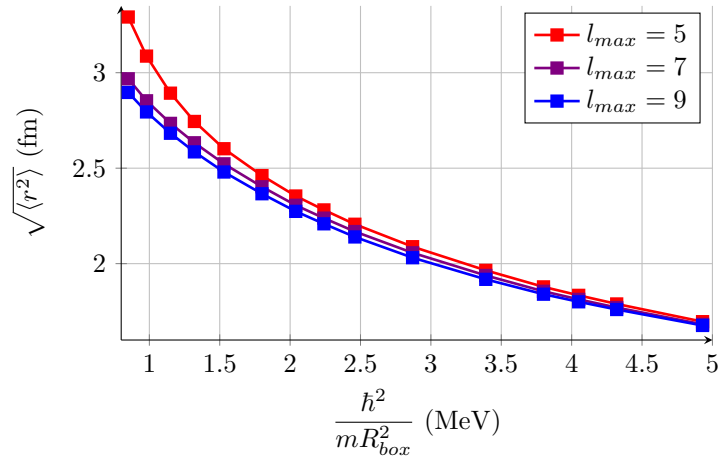


**Figure 5.44:** Convergence of the r.m.s. radii for  $^{16}\text{O}$  calculated with ADC2 approximation and  $\text{N}^4\text{LO550}$  potential for different truncations of the single-particle Bessel DVR basis

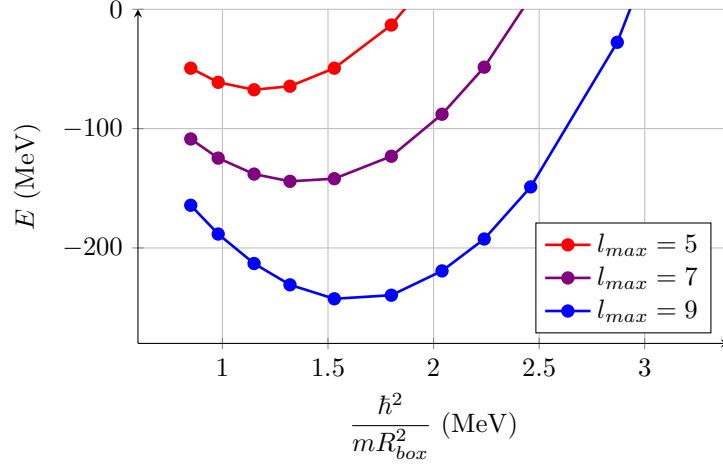


**Figure 5.45:** Convergence of the ground-state energy for  $^{48}\text{Ca}$  calculated with ADC2 approximation and  $\text{N}^4\text{LO550}$  potential for different truncations of the single-particle Bessel DVR basis

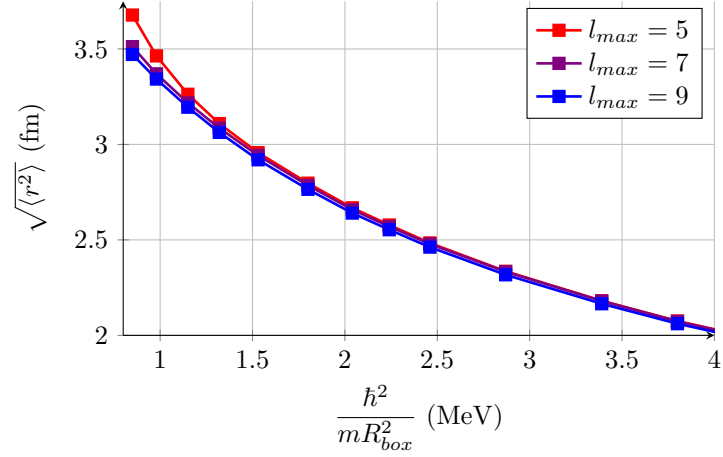


**Figure 5.46:** Convergence of the r.m.s. radii for  $^{48}\text{Ca}$  calculated with ADC2 approximation and  $\text{N}^4\text{LO550}$  potential for different truncations of the single-particle Bessel DVR basis

Moving to ADC2 calculations, the HO energies seem to have a worse convergence respect to the  $\text{N}^4\text{LO450}$  case, as one could expect for a harder potential.

### 5.2.2 N<sup>3</sup>LO EMN potential

Finally, we present some calculations performed with N<sup>3</sup>LO(500) potential, which is the hardest between the three potentials that we have seen. In this case we only show the results for the case of <sup>16</sup>O.

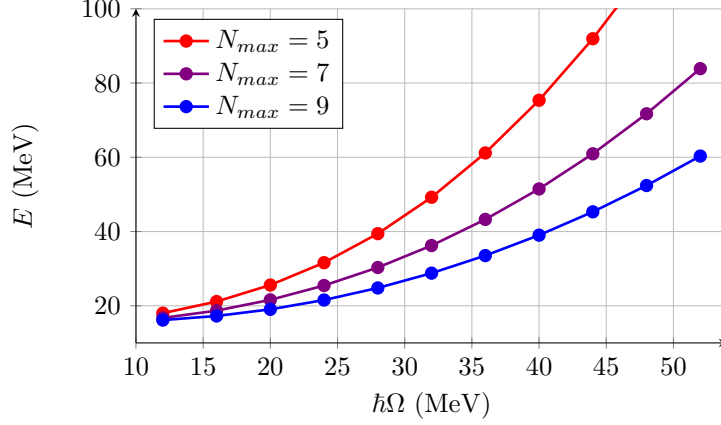


**Figure 5.47:** Convergence of the energies for <sup>16</sup>O calculated with HF approximation and N<sup>3</sup>LO(500) potential for different truncations of the single-particle HO basis

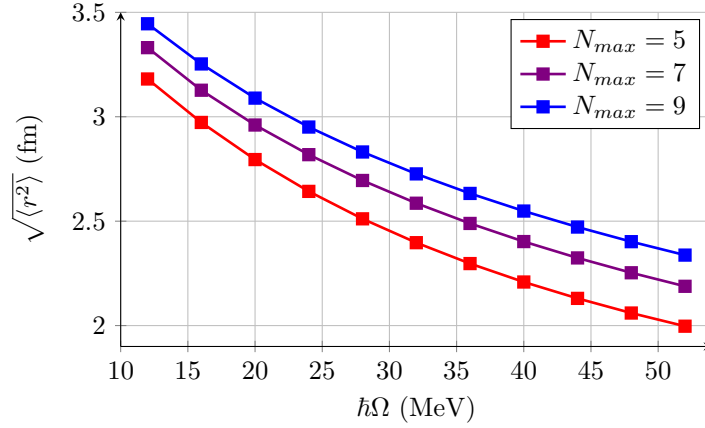


**Figure 5.48:** Convergence of the r.m.s. radii for <sup>16</sup>O calculated with HF approximation and N<sup>3</sup>LO(500) potential for different truncations of the single-particle HO basis

HF energies converge to a positive value of the energy which is higher than in the case of N<sup>4</sup>LO550 and the convergence seems to be not yet reached at  $\hbar\Omega \approx 12$  MeV, which is the minimum computed value of the oscillator energy.

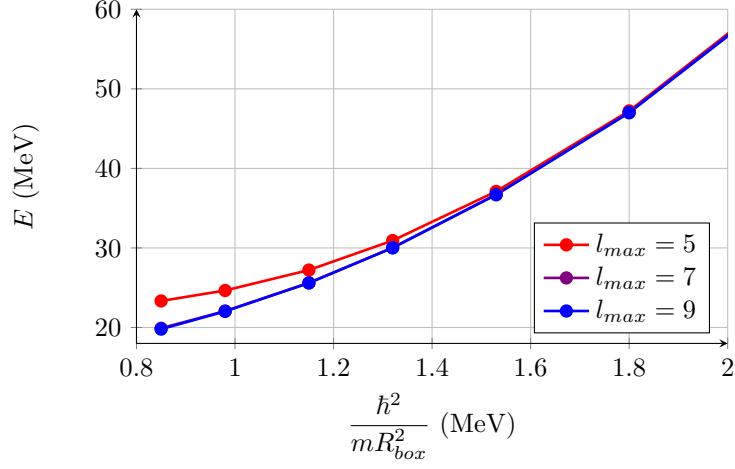


**Figure 5.49:** Convergence of the energies for  $^{16}\text{O}$  calculated with HF approximation and  $\text{N}^3\text{LO}(500)$  potential for different truncations of the single-particle Bessel DVR basis

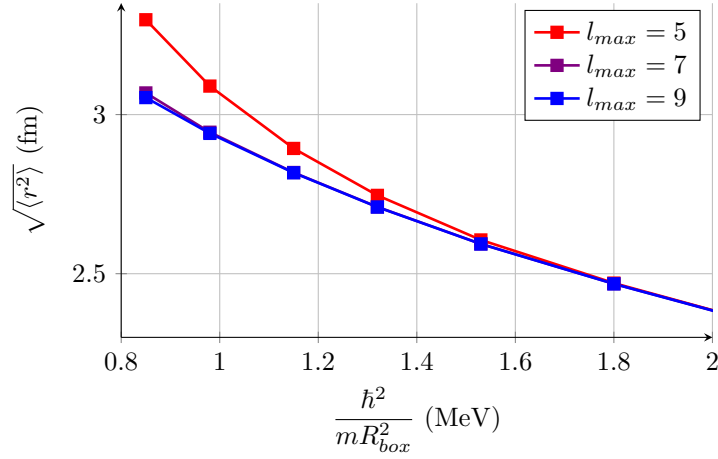


**Figure 5.50:** Convergence of the r.m.s. radii for  $^{16}\text{O}$  calculated with HF approximation and  $\text{N}^3\text{LO}(500)$  potential for different truncations of the single-particle Bessel DVR basis

As in the case of the other potentials, HF convergence is reached on all the considered domain of  $R_{box}$  for  $l_{max} = 7$ . Boxes dimensions larger than 8 fm seem to be necessary to reach the minimum for the parabolas in the energy graphs.

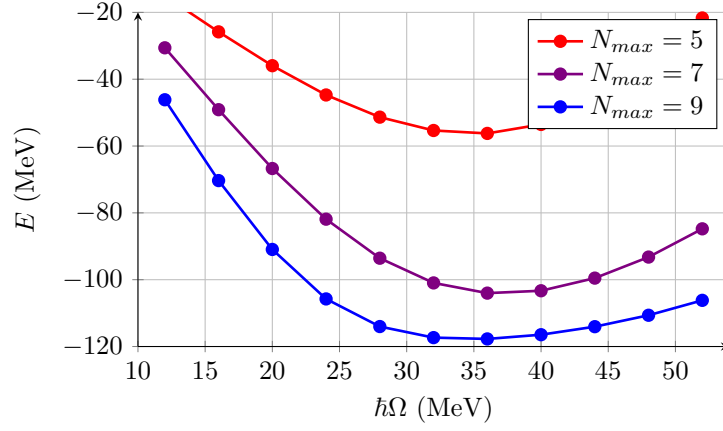


**Figure 5.51:** Convergence of the ground-state energies for  $^{16}\text{O}$  calculated with ADC2 approximation and  $\text{N}^3\text{LO}(500)$  potential for different truncations of the single-particle HO basis

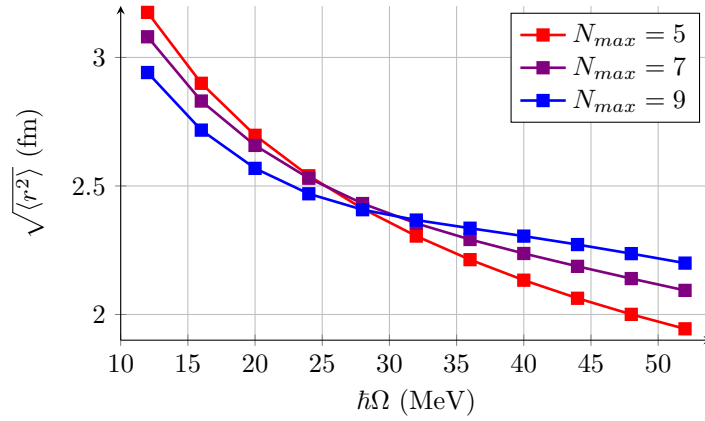


**Figure 5.52:** Convergence of the r.m.s. radii for  $^{16}\text{O}$  calculated with ADC2 approximation and  $\text{N}^3\text{LO}(500)$  potential for different truncations of the single-particle Bessel DVR basis

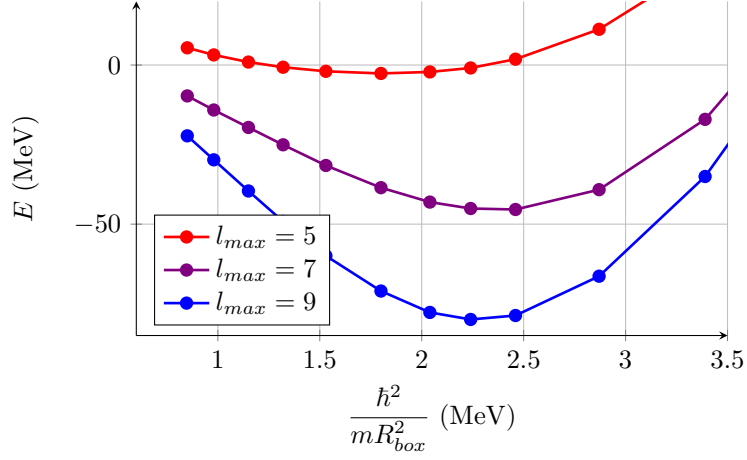


**Figure 5.53:** Convergence of the ground-state energy for  $^{16}\text{O}$  calculated with ADC2 approximation and  $\text{N}^3\text{LO}(500)$  potential for different truncations of the single-particle Bessel DVR basis

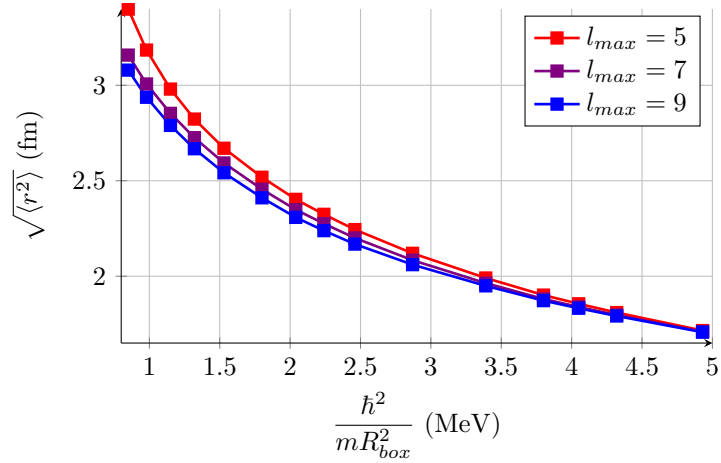


**Figure 5.54:** Convergence of the r.m.s. radii for  $^{16}\text{O}$  calculated with ADC2 approximation and  $\text{N}^3\text{LO}(500)$  potential for different truncations of the single-particle Bessel DVR basis

Finally, ADC2 calculations show difficulties in converging for both the two basis, especially for the Bessel DVR one. In this basis, radii show a better behavior than the energies, converging to same values at  $l_{max} = 7$ .

## CHAPTER 6

### SUMMARY AND CONCLUSIONS

This thesis focused on the analysis of the use of different spherical basis in *ab initio* nuclear structure calculations. First we gave an overview of the *ab initio* methods, introducing the many-body Hamiltonian and specializing the discussion to the case of the Self-consistent Green's functions, which was our method of choice for precise many-body computations. We decided to test our computation tool on chiral EFT interactions, since these provide the best inputs for state-of-the-art nuclear structure. We derived the analytical form of the interaction matrix elements in the case of HO basis, then we derived efficient working equations for generalized spherical bases with the help of the Wong-Clement brackets [20], which have been discussed in depth. After, we introduced the discrete variable representation (DVR) theory, with particular attention to the case of the functions that we aimed to investigate. Results of the computation made with the two different HO and Bessel DVR bases have then been compared.

Based on our results showed in Section 5.1, the following general conclusions can be drawn. The HO results behave as expected from know-how in *ab initio* computations, hence proving the efficiency and well functioning of the codes we developed. The optimal value of  $\hbar\Omega$  falls as the nucleon number increases and the radii tend to converge to a value at which curves with different model space  $N_{max}$  tend to intersect. In the case of the HF calculations, we introduced a COM correction for the radii and confirmed that this did not alter the convergence pattern, causing only a little shift of the results of about 0.05 fm. Then we performed a more advanced kind of calculation, the ADC2 approximation, which includes nuclear correlations, as opposed to HF case. In this approximation, the optimal  $\hbar\Omega$  assumes high values, in line with the soft character of the chiral

potentials employed. The rate of convergence of the results is strongly dependent on the chiral potential used for the computation. Calculations converge faster for the softer potential ( $N^4\text{LO}450$ ) and slower for the harder one ( $N^3\text{LO}(500)$ ). The results in the two different bases converge qualitatively to the same results for the energies and the radii in the case of  $N^4\text{LO}450$  potential, despite the Bessel DVR being defined on a model space with poor UV and IR cutoffs. For harder potentials, the Bessel DVR struggles to reproduce the energies obtained in the HO case, still showing a good convergence for the radii. The energies and the radii computed with the Bessel DVR basis have proved to depend on the box upon which they are defined and this behavior remained unchanged after the application of the center-of-mass correction that we performed for the HF radii. The infrared limit of the two bases has then been studied with an extrapolation of the energies and radii of the studied nuclei in the limit of infinite boxes. These results showed a good agreement for the charge radii, within the uncertainties deriving from the fitting procedure. The ground-state energies showed a better compatibility than the computed ADC2 ones.

DVR seem to be promising and further analyses of their application in nuclear structure calculations are worth to be performed. Future studies should focus on investigating a broader range of different spherical basis for similar computations as those done in this work. As the main limitation of the Bessel DVR basis seems to be the dependence of the results on the chosen box in the coordinate space, the following two variations of this basis are ready to be tested with the same previously discussed computations. A first possibility is to change the boundary conditions, using the von Neumann one. This allows the nucleus not to be confined in a box, still keeping the advantages of the DVR basis in the study of IR and UV limits. Equations for this functions have been derived in this work in Section 4.2.1. A second alternative consists in switching the definition of the box in which the nucleus is confined from the coordinate space to the momentum space. This basically implies a cutoff on the energies that could even simplify the construction of the Bessel model space. The analytical form of these functions has been derived in [32]. Finally, sinc functions and Airy functions are worth to be tested with the machinery that we developed, as the mathematical tools necessary to their applications has already been built [26, 29] in the DVR case.

Overall, the formalism developed in this work led the way to the use of a vast number of different basis functions in nuclear applications and the different advantages of each one could be exploited.

## BIBLIOGRAPHY

- [1] D. Baye and P. H. Heenen. ‘Generalised meshes for quantum mechanical problems’. In: *Journal of Physics A* 19, 2041 (1986).
- [2] A. Bulgac and M. M. Forbes. ‘Use of discrete variable representation basis in nuclear physics’. In: *Phys. Rev. C* 87, 051301 (2013).
- [3] T. Inoue. ‘Strange Nuclear Physics from QCD on Lattice’. In: *AIP Conference Proceedings* 2130, 020002 (2019).
- [4] H. Hergert and R. Roth. ‘Treatment of the intrinsic Hamiltonian in particle-number nonconserving theories’. In: *Phys. Lett. B* 682, 27 (2009).
- [5] S. C. Pieper and R. B. Wiringa. ‘Quantum Monte Carlo Calculations of Light Nuclei’. In: *Annual Review of Nuclear and Particle Science* 51, 2001 (2002).
- [6] B. R. Barrett, P. Navrátil, and J. P. Vary. ‘Ab initio no core shell model’. In: *Progress in Particle and Nuclear Physics* 131 (2013).
- [7] G. Hagen et al. ‘Coupled-cluster computations of atomic nuclei’. In: *Reports on Progress in Physics* 77, 096302 (2014).
- [8] A. Cipollone, C. Barbieri, and P. Navrátil. ‘Isotopic chains around Oxygen from evolved chiral two- and three-nucleon Interactions’. In: *Phys. Rev. Lett.* 111, 062501 (2013).
- [9] R. Roth, *Ab initio calculations of nuclear structure, Lectures at the school Frontiers in Nuclear and Hadronic Physic.* 2021. URL: <https://youtu.be/r1AwdDeilEo>.
- [10] H. Hergert et al. ‘Ab initio calculations of even Oxygen isotopes with chiral two-plus-three-nucleon interactions’. In: *Phys. Rev. Lett.* 110, 242501 (2013).

- 
- [11] M. P. Lombardo, M. Hjorth-Jensen and U. van Kolck. *An Advanced Course in Computational Nuclear Physics - Bridging the Scales from Quarks to Neutron Stars*. Springer, 2017.
- [12] C. Barbieri and M. Hjorth-Jensen. ‘Quasiparticle and quasihole states of nuclei around  $^{56}\text{Ni}$ ’. In: *Phys. Rev. C* 79, 064313 (2009).
- [13] S. Brolli. *Correlazioni nucleari in catene isotoniche con  $N=20$  e  $N=28$* . 2020.
- [14] A. Carbone et al. ‘Self-consistent Green’s functions formalism with three-body interactions’. In: *Phys. Rev. C* 88, 054326 (2013).
- [15] F. Raimondi and C. Barbieri. ‘Algebraic diagrammatic construction formalism with three-body interactions’. In: *Phys. Rev. C* 97, 054308 (2018).
- [16] F. Raimondi and C. Barbieri. ‘Nuclear electromagnetic dipole response with the self-consistent Green’s function formalism’. In: *Phys. Rev. C* 99, 054327 (2019).
- [17] R. Machleidt and D. R. Entem. ‘Chiral effective field theory and nuclear forces’. In: *Phys. Rep.* 503, 1 (2011).
- [18] D. R. Entem, R. Machleidt, and Y. Nosyk. ‘High-quality two-nucleon potentials up to fifth order of the chiral expansion’. In: *Phys. Rev. C* 96, 024004 (2017).
- [19] V. Bernard, N. Kaiser, and Ulf-G. Meißner. ‘Aspects of chiral pion-nucleon physics’. In: *Nucl. Phys. A* 615, 483 (1997).
- [20] C. W. Wong and D. M. Clement. ‘Vector bracket and transformed wave function of a few-body state’. In: *Nucl. Phys. A* 183, 210 (1971).
- [21] R. Balian and E. Brézin. ‘Angular-momentum reduction of the Faddeev equations’. In: *Il Nuovo Cimento B* 61, 403 (1969).
- [22] C. L. Kung, T. T. S. Huo, and K. F. Ratcliff. ‘Converged values of second-order core-polarization diagrams with orthogonalized-plane-wave intermediate states’. In: *Phys. Rev. C* 19, 1063 (1979).
- [23] N. Austern et al. ‘Theory of finite-range distorted-waves calculations’. In: *Phys. Rev.* 133, B3 (1964).
- [24] B. F. Bayman and A. Kallio. ‘Relative-angular-momentum-zero part of two-nucleon wave functions’. In: *Phys. Rev.* 156, 1121 (1966).
- [25] R. G. Littlejohn et al. ‘A general framework for discrete variable representation basis sets’. In: *J. Chem. Phys.* 116, 8961 (2001).
- [26] R. G. Littlejohn and M. Cargo. ‘Multidimensional discrete variable representation bases: Sinc functions and group theory’. In: *J. Chem. Phys.* 116, 7350 (2002).

- 
- [27] J. C. Light and T. Carrington. *Discrete Variable Representation and their Utilization*. 2003.
- [28] D. Lemoine. ‘A note on orthogonal discrete Bessel representations’. In: *J. Chem. Phys.* 118, 6697 (2003).
- [29] R. G. Littlejohn and M. Cargo. ‘An Airy discrete variable representation basis’. In: *J. Chem. Phys.* 117, 37 (2002).
- [30] J. C. Light, I. P. Hamilton, and J. V. Lill. ‘Generalized discrete variable approximation in quantum mechanics’. In: *J. Chem. Phys.* 82, 1400 (1984).
- [31] *Discrete Variable Representation, R. Martinazzo*. URL: <https://users.unimi.it/cdtg/download/notes/DVR.pdf>.
- [32] R. G. Littlejohn and M. Cargo. ‘Bessel discrete variable representation bases’. In: *J. Chem. Phys.* 117, 27 (2002).
- [33] D. Lemoine. ‘The discrete Bessel transform algorithm’. In: *J. Chem. Phys.* 101, 3936 (1994).
- [34] D. R. Entem and R. Machleidt. ‘Accurate charge-dependent nucleon-nucleon potential at fourth order of chiral perturbation theory’. In: *Phys. Rev. C* 68, 041001 (2003).
- [35] R. J. Furnstahl, G. Hagen, and T. Papenbrock. ‘Corrections to nuclear energies and radii in finite oscillator spaces’. In: *Phys. Rev. C* 86, 031301 (2012).
- [36] S. N. More et al. ‘Universal properties of infrared oscillator basis extrapolations’. In: *Phys. Rev. C* 87, 044326 (2013).
- [37] S. A. Coon et al. ‘Convergence properties of ab initio calculations of light nuclei in a harmonic oscillator basis’. In: *Phys. Rev. C* 86, 054002 (2012).
- [38] S. König et al. ‘Ultraviolet extrapolations in finite oscillator bases’. In: *Phys. Rev. C* 90, 064007 (2014).
- [39] N. Bygaard et al. ‘Vortex line in a neutral finite-temperature superfluid Fermi gas’. In: *Phys. Rev. A* 69, 053622 (2004).
- [40] V. Somà, C. Barbieri, and T. Duguet. ‘Ab initio self-consistent Gorkov-Green’s function calculations of semi-magic nuclei: Numerical implementation at second order with a two-nucleon interaction’. In: *Phys. Rev. C* 89, 024323 (2009).